ABSTRACT

Title of Dissertation: CONTRIBUTIONS TO RESOLVING ISSUES IMPEDING THE OPERATION OF HIGH POWER MICROWAVE AND SUBMILLIMETER DEVICES

Dmytro Kashyn, Doctor of Philosophy, 2014

Dissertation directed by:
Professor Victor Granatstein
Department of Electrical and Computer Engineering, UMCP
Dr. Gregory Nusinovich, IREAP, Co-Advisor
Dr. John Rodgers, IREAP, Co-Advisor

This thesis reports an experimental study aimed at extending high power, high efficiency gyrotron operation to submillimeter wavelengths. A series of experiments carried out both at the University of Maryland and the Institute of Applied Physics of the Russian Academy of Science, succeeded in demonstrating output power at 670 GHz of 180 kilowatts with 20% efficiency (gyrotron voltage was 57 kV and beam current was 16 amperes). The maximum output power achieved in the experiments was 210kW at somewhat higher voltage and current (viz. 58kV and 22A). The achieved output power and efficiency are twice as large as achieved in previous experiments in this frequency range with pulse duration in the range of tens of

microseconds. These performance parameters are relevant to a previously proposed application of detecting concealed radioactive materials by air breakdown in a focused beam of sub-millimeter radiation. The 670 GHz gyrotron combined features of two lines of previous experiments: (a) to operate at the required frequency, pulsed solenoids producing 28T magnetic were employed and (b) to obtain high efficiency a very high order mode was used in the gyrotron cavity, as in the experiments with gyrotrons for plasma heating.

Evidence of multimode beating was observed in submillimeter output envelope. The excitation of spurious modes, especially during the rise of the gyrotron voltage pulse, was analyzed and the method of avoiding this was proposed which also allows to reduce collector loading in gyrotrons operating in modulated regimes.

The present study also includes theoretical analysis of the processes that deepens the understanding of microwave breakdown (arcing) in high power microwave devices. The effect of the dust particles microprotrusions on the device operation was analyzed. These microprotrusions were observed and their negative effects were remedied by careful polishing and machining of the resonator surface.

Finally, the generated 670 GHz radiation was focused and used to study breakdown both in argon and in the air. This breakdown volume was theoretically analyzed and the effects of the atmospheric turbulence on the air breakdown were included.

CONTRIBUTIONS TO RESOLVING ISSUES IMPEDING THE OPERATION OF HIGH POWER MICROWAVE DEVICES

By

Dmytro Kashyn

Dissertation submitted to the Faculty of the Graduate School of the
University of Maryland, College Park, in partial fulfillment
of the requirements for the degree of
Doctor of Philosophy
2014

Advisory Committee:

Professor Victor Granatstein, Chair
Professor Thomas Antonsen
Professor Howard Milchberg
Professor Daniel Lathrop
Dr. Gregory Nusinovich
Dr. John Rodgers

Dedication

To My Family My Mentors And My Friends

Acknowledgements

I want to thank all wonderful people at IREAP who contributed to the completion of this dissertation. First of all I want to thank Dr. Gregory Nusinovich who was the key person in my decision to start this work, and whose wise guidance helped me immensely during my years in graduate school. Secondly, I want to thank Dr. Thomas Antonsen Jr., whose patience and calmness helped me in the most critical moments of my graduate life. Thirdly, I want to thank Dr. John Rodgers for his passion and drive for experimental science and his guidance and support for my work. The last, but not the least person to whom I want to thank for my academic achievements is my advisor, Dr. Victor Granatstein, who provided guidance and overall management of my work. The construction of experiments described in this thesis would have been not possible without help of IREAP staff. Jay Pyle, Don Martin, Nolan Ballew, Nancy Booone, Bryan Quinn, Edward Condon, Dorothea Brosius and Roxanne Defendini provided help at various stages of my work. I would like to thank all my friends, Aydin Kesar, Long Nguyen, Sergey Novikov, Dr. Sergey Pershoguba, Ruifeng Pu, Dr. Olexandr Sinitsyn and Alexey Vedernikov who were with me during these years.

I want to thank my father, my mother, my wonderful sister and my entire family, whose support is hard to quantify, but is impossible to forget. Lastly, I want to thank my girlfriend, Nastia, who aided me in more ways that I can count.

Table of Contents

List of Figures

Chapter 1: Experimental studies of sub-terahertz gyrotron for remote detection of concealed radiation

1.1 Introduction

There is a high interest in the detection schemes that can remotely sense concealed radioactive materials. These schemes should be primarily used to prevent radioactive materials from being brought into the country, since a so called "dirty bomb" can be used to devastating effect, even if the amounts of radioactive materials are relatively small. This threat, combined with the fact that less t1han two percent of the containers [1.1] entering the US by sea are thoroughly checked, drives interest in a remoter scheme that can reliably detect the presence of radioactive materials in maritime environments. Conventional tools for radiation detection, such as Geiger counters, lack the ability to remotely detect the radiation. They need to be in close proximity to the source to obtain reliable readings, and the performance deteriorates when even a modest amount of screening is present. The first chapter of my dissertation focusses on experimental activities with a novel 670 GHz gyrotron developed for a practical realization of a recently proposed scheme for detection of concealed radiation. The chapter gives a brief description of the scheme and provides an explanation of why the gyrotron is operating at the specific frequency and power needed for the experiments. Then the details of the design and analysis of the gyrotron and its various components are provided along with the results of the experiments performed with this device at the University of Maryland in collaboration with the Institute of Applied Physics of the Russian Academy of

Science. Some of the results presented in this chapter were published in Applied Physics Letters [1.2], and presented at a workshop held at University of Maryland.

1.2 Motivation

Recently Nusinovich and Granatstein [1.3] proposed a novel scheme for remote detection of concealed radiation. This scheme involves the initiation of the breakdown of air in a certain volume with a high power source, and measurements of the volume under study to determine the presence of the radioactive materials in the vicinity of that volume. Microwave breakdown was studied at least since 1970s [1.8]. Typically, when air breakdown is discussed, this means that the breakdown involves radiation from high power lasers [1.4] with short pulses. This process involves avalanche ionization of the gas in the presence of seed electrons. In this breakdown scenario a multiphoton ionization process is involved, and this breakdown mechanism requires the density of the electromagnetic power of the order or higher than 10^{14} W/m^2. There is, however, another breakdown mechanism that happens when the pulse duration are longer than tens of nanoseconds. In this breakdown mechanism an avalanche discharge occurs, providing that seed electrons were present in the volume under the consideration. This process, called an avalanche breakdown. In the absence of radioactive material the density of seed electrons $n_{e,amb}$ is 1-2 electrons per cubic centimeter, and the breakdown rate is low. When, the radioactive material is present, the density of seed electrons is greatly enhanced, $n_e \gg n_{e,amb}$ and the breakdown rate is high. Thus it is important to focus the radiation into the volume of the order of one cubic centimeter. The electromagnetic power densities required for this process to occur are much smaller than for the laser breakdown; however, there are certain restriction that applies to this process: for instance, the breakdown will only happen if the air in the volume is significantly pressurized above the ambient level [1.5]. The numerical simulations performed with Monte Carlo codes [1.6] for 1kgCi of radioactive cobalt show that electron production rate outside a container that encloses a radioactive material exceeds the naturally occurring electron production rate by a several orders of magnitude. This result implies that enough gamma radiation will penetrate the walls of the container to ionize the air in its vicinity, thus making the scheme feasible.

Based on these considerations the following detection scheme was proposed. The “suitable” (the requirements for the source will be given later) electromagnetic source produces electromagnetic radiation that is focused in a volume in the vicinity of the possible location of the radioactive source. The field of electromagnetic wave exceeds the breakdown limit in a volume into which this field is focused. By observing the occurrence of the breakdown from that volume the presence of radioactive materials in its vicinity can be deduced. The theoretical basis of the method was given in the series of articles by Nusinovich, Granatstein and their colleagues [1.6] [1.7] these articles deal with various aspects of the proposed method, such as range and resolution of the system as well as the imposed power requirements. In this section, I will reproduce the results that are relevant to my theoretical and experimental work that was done in the course of this project; namely, the restrictions and requirements that the electromagnetic source should meet in order to be used in the detection scheme, and the calculations that determine range and resolution of the system.

1.3 Description of the scheme

Air breakdown is well documented in the literature [1.8]. According to the theory, avalanche breakdown at atmospheric pressure will occur when the electric field in a certain volume exceeds a certain threshold value, providing that this volume contain some free ellectrons. The value of this threshold field is given by:

$$E_{th} = 3.2\times 10^{6}\left(1+\left(\frac{\omega}{\nu_k}\right)^{2}\right)^{1/2} \quad \frac{V}{m} \tag{1.1}$$

In this formula $\omega = 2\pi f$ is the angular wave frequency and $\nu_k = 2\pi\times 685\times 10^{9}\ s^{-1}$ is the effective electron-molecule collision frequency. The threshold power density corresponding to this electric field is:

$$S_{th} = 0.5\frac{E_{th}^{2}}{Z_0} = 1.36\times 10^{10}\left[1+\left(\frac{\omega}{\nu_k}\right)^{2}\right] \frac{W}{m^{2}}, \tag{1.2}$$

here, $Z_0 = 377\ \Omega$ is the wave impedance of free space.

The threshold power is calculated under the assumption that the radiation can be focused into a spot with linear size of the order of one wavelength, according to the following formula:

$$P_{th} = S_{th}\pi\lambda^{2} = 4.3\times 10^{10}\left[1+\left(\frac{\omega}{\nu_k}\right)^{2}\right]\left(\frac{2\pi c}{\omega}\right)^{2} W \tag{1.3}$$

The figure 1.1 shows this dependence plotted in the frequency range 10GHz < f < 100THz. This frequency range corresponds to the following range of the wavelength of electromagnetic radiation from $3\,\mu m$ to 3cm.

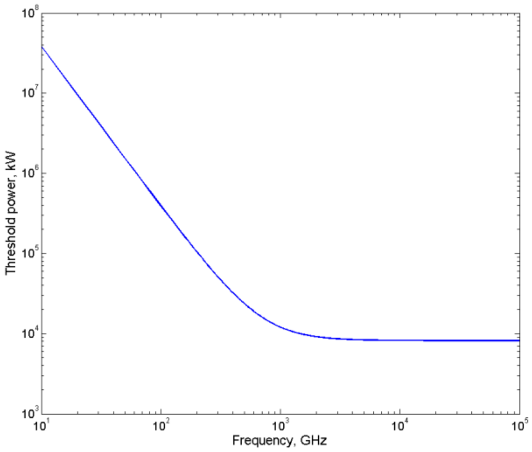

Figure 1.1 The dependence of the threshold power on the frequency.

It can be seen from the figure 1.1 that as the operating frequency increases the threshold power approaches a limiting value which is independent of the frequency. It can also be seen from this plot that it is beneficial to operate the system at frequencies of the order of one terahertz to reduce the power requirements.

Apart from the choice of the suitable operating frequency the three following requirements should be met in order for the system to operate effectively:

(1) Electromagnetic energy from the chosen pulsed source should propagate through the atmospheric air and be focused in the volume V, and for the duration of the pulse the power density should exceed the threshold power density:

$$S > S_{th} \tag{1.4a}$$

(2) The pulse duration should be sufficient to allow the avalanche breakdown to occur, i.e:

$$\tau_{pulse} > \tau_{\mu}\,, \tag{1.4b}$$

where τ_μ is the time required for the avalanche breakdown to build up, which is dependent on the operational frequency and effective ionization rate. This time is of the order of 100 ns for frequency in the range from 0.01 to 28.3 THz, and in order to enhance the resolution of the system the following condition should hold $\tau_{pulse} \gg \tau_\mu$.

(3) Volume, into which the radiation is focused should be small enough that the appearance of a free electron during the time τ_μ is a rare occurrence at the ambient level of background electron density $n_{eo} \sim 10^6 m^{-3}$, i.e.:

$$V < n_{eo}^{-1} \sim 1000\, mm^3 . \qquad (1.4c)$$

The estimates for the range, assuming a Gaussian profile of the beam, can be done using well-established theory [1.9]. The cross-sectional area of the beam along the axial coordinate is given as:

$$A_\perp = A_{\perp 0}\left(1 + \frac{(\lambda z)^2}{\left(2\pi w_0^2\right)^2}\right), \qquad (1.5)$$

where $A_{\perp 0} = \pi w_0^2$ is the area of the beam at the focal waist, $z = 0$, and w_0 is the beam radius. At the antenna, i.e. at $z = -R$, the beam cross section is given as $A_\perp = \pi a^2$, where a is the beam radius at the lens. The assumption that the lens radius is given by $r_{lens} = \sqrt{2}\, a$, which ensures that more than 98% of the beam power is focused by the lens. Then equation (1.5) gives the following estimate for the range of the system:

$$\frac{R}{r_{lens}} = \frac{\left(\sqrt{2}\pi w_0\right)}{\lambda} \qquad (1.6)$$

The radius of the beam at the lens depends on the power produced by the source according to the equation (1.3) is given by $\frac{P_{th}}{S_{th}} = \pi\lambda^2$, and also at the beam waist for a Gaussian beam $\frac{P}{S_0} = \frac{\pi}{2} w_0^2$, where S_0 is the power density on axis. According to these formulas the radius of the beam at the focal plane may be expressed as:

$$w_0 = \lambda \left[2 \left(\frac{S_{th}}{S_0} \right) \left(\frac{P}{P_{th}} \right) \right]^{\frac{1}{2}} \tag{1.7}$$

the ratio $\frac{S_0}{S_{th}}$ is chosen as 1.5 (or 3 for the sources with shorter pulse durations). The ratio $\frac{P}{P_{th}}$ is the power ratio delivered to the source (including the effect of the atmospheric absorption). The last parameter in the figure 1.2 that depicts the focusing geometry is L_{dif}. If the breakdown volume is assumed to be prolate spheroid with minor semiaxis r_0 and major semiaxis $L_{dif} / 2$ then the volume is equal to:

$$V = \left(\frac{2}{3} \right) \pi r_0^2 L_{dif} \tag{1.8}$$

and the expression for the diffraction length is as following:

$$L_{dif} = 4\pi \left(\frac{w_0^2}{\lambda} \right) \left(\frac{S_0}{S_{th}} - 1 \right)^{\frac{1}{2}} \tag{1.9}$$

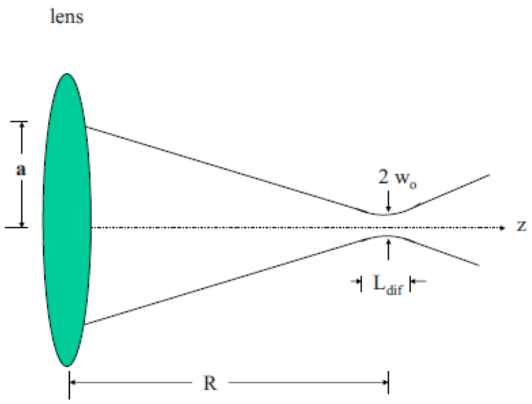

Figure 1.2 The focusing geometry of the system that is used for the estimates.

The original paper [1.3] proposed several potential candidates for the sources used in the scheme. They included: a 0.67 THz gyrotron oscillator with power in excess of 200kW and a pulse duration of at least $10\,\mu s$, a 91.4 GHz second harmonic gyroklystron amplifier with peak power of 1.5 MW and a pulse duration of $1\,\mu s$ [1.10], and a couple of similar transversely Excited Atmospheric-Pressure (TEA) CO_2 lasers [1.11] with a wavelength of $10.6\,\mu m$ with peak powers and wavelength of 100MW / 30 *ns* and 30MW / 100 *ns* respectively. The source of a choice was the 0.67THz gyrotron. This source has a reasonable power density ratio equal to 1.5, low threshold power, equal to 17kW and a reasonable ration of the pulse duration to the time required to build up the breakdown, i.e. $\tau/\tau_\mu = 90$. At this frequency the wavelength of the electromagnetic radiation is equal to 0.44*mm* and according to Eq. (1.8) the volume in which breakdown occurs is estimated to be 88mm^3. The other advantage of using this source in the scheme is that for the atmospheric pressure this frequency is close to the bottom of the Paschen's curve and there is an atmospheric window with a relatively small attenuation of 0.05 dB/m, which means that the range of the system can effectively be a few hundreds of meters.

1.4 Description of gyrotron

After giving the description of the source used in the scheme it is important to explain what is a gyrotron and how it operates. The Gyrotron is a well-studied device that celebrates its half century “anniversary” this year [1.12]. It is a well-studied, well understood tool. The theory describing various aspects of the device operation is developed and various experiments were performed in the course of the half century This type of devices has a wide range of application, which includes plasma heating [1.13], radar applications [1.14], material processing [1.15] and NMR spectroscopy [??]. Recently, a new set of potential applications for high power terahertz sources were proposed, for which gyrotrons may be promising candidates, see for instance [1.16], and the references therein. These applications also include previously discussed scheme for detection of concealed radiation. However increasing the operating frequency of a gyrotron into the subterahertz range leads to several technological problems that should be addressed in order to create a device with efficiency high enough to achieve the desired power output.

In order to address these issues some information about the components of the gyrotron tubes and its principles of their operation should be provided before the further discussion can be given. Gyrotrons are members of the class of devices collectively known as electron cyclotron masers (ECM) or cyclotron resonance masers (CRM)[1.17]. The principle of the device operation is based on the cyclotron maser instability [1.18]. This instability occurs due to the fact that there is a relativistic dependence of the electron cyclotron frequency on the electron energy. The gyrotron is defined [1.19] as a cyclotron resonance maser in which the interaction of a helical electron beam with electromagnetic waves happens in nearly uniform open waveguides near a cutoff frequency. Figure 1.1, reproduced from [1.20], is the simplest gyrotron configuration.

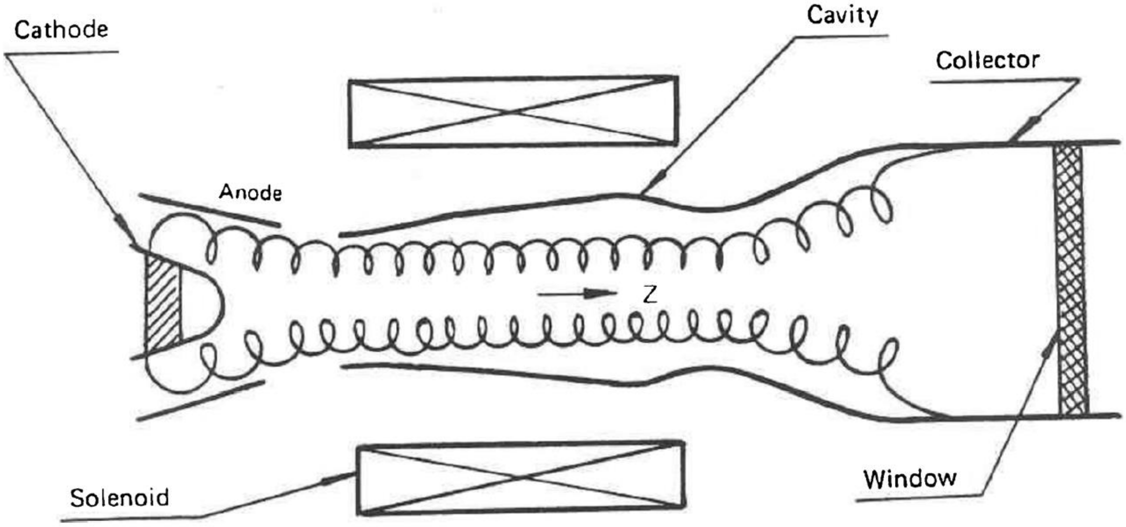

Figure 1.3 The arrangement of the simplest gyrotron oscillator, known as gyromonotron, reproduced from [1.20].

An electron beam is generated by an emitter, this emitter has a certain shape to produce an annular beam. The beam is propagated in the cathode – anode gap, accelerated by the electric field due to potential difference between the anode and the cathode. This electric field has both perpendicular and parallel components with respect to the magnetic field generated by a solenoid. This means that the electrons emitted from the cathode increase the components of their orbital and axial velocities. The electrons move towards the cavity in an increasing magnetic field, in which the electron flow is adiabatically compressed, thus increasing the electron orbital momentum. In the resonator, where the magnetic field is uniform, beam-wave interaction happens and part of the electron kinetic energy is transformed into the microwave energy. The spent beam exits the cavity, decompresses in the decreasing magnetic field and is deposited on the collector. The collector also serves a role of an oversized output waveguide, directing the output radiation towards the output window. After the electromagnetic energy is extracted, the spent beam is dumped onto the collector and the produced radiation is extracted from the output window of the tube.

In the gyromonotron an electron beam is formed by the magnetron injection gun (MIG)[1.21]. This is a specific arrangement of an electron gun which forms the hollow electron beam in the DC electric field caused by the voltage applied between the cathode and anode. The beam is further confined towards resonator, where the interaction occurs,. The electrons experience the adiabatic compression which increases their orbital momentum in accordance with the conservation law $p_{\perp}^2 / B = const$. Under the resonance condition:

$$\omega - k_z v_z \approx s\Omega \tag{1.10}$$

the electrons with cyclotron frequency $\Omega = eB / m_0 \gamma$ interact in the cavity with an electromagnetic field producing the electromagnetic radiation. In the equation (1.10) ω and k_z are the wave angular frequency and axial wavenumber respectively, v_z is the electron axial velocity and s is the cyclotron resonance harmonic number.

From equation (1.10) it follows that changes in the electron energy in the process of the interaction with electromagnetic wave may cause axial bunching and due to changes in the electron axial velocity and orbital bunching due to the dependence of the electron cyclotron frequency on the energy. It also follows from the equation (1.10) that in the course of interaction with traveling waves the spread in axial velocities can result in significant inhomogeneous Doppler broadening of the cyclotron resonance band, which typically lead to efficiency deterioration. To compensate for this effect and operate in the regime where broadening is weak, the gyrotrons typically operate near a cutoff frequency, i.e. with waves that have small k_z. The dispersion diagram is shown in figure 1.4 [1.20].

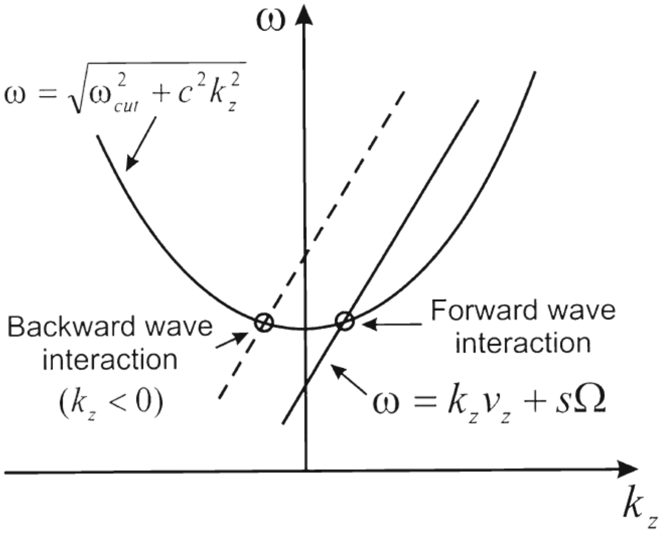

Figure 1.4 Dispersion diagram of the gyromonotron that operates near cutoff. The parabola shows the dispersion curve of a smooth-wall waveguide with cutoff frequency ω_{cut}. Straight lines correspond to the wave beam line of forward-wave (positive k_z) and backward-wave (negative k_z) interaction, reproduced from [1.20].

The interaction, when part of the electron kinetic energy is transformed into microwave energy, is happening in the resonator. This process of interaction of electrons with electromagnetic wave can be divided into three stages:

a) Energy modulation;

b) Orbital bunching;

c) Deceleration of the bunch.

When the electrons are emitted from the cathode they have uniform angular distribution. During the first stage of the interaction the electron ring is displaced towards the region of the accelerating field where $v_{\perp} E < 0$, the energy of some electrons increases while the energy of the electrons with different gyrophases decreases. During this stage, the energy of the electron ring on average increases, i.e. the electrons absorb energy from electromagnetic wave. During the second stage of the process, the modulation of electron energies, due to relativistic effect of the dependence of the electron mass on the energy, causes the small changes in the electron cyclotron frequency, which results in the formation of the electron bunch. If the frequency of the electromagnetic wave slightly exceeds the cyclotron frequency of the electrons or its resonance harmonic ($\omega > s\Omega_0$) an electron bunch is formed in the decelerating phase of the electromagnetic field. During the last stage of the process the electron bunch is decelerated and the electrons transfer energy of the gyration to the electromagnetic field. This process is illustrated in figure 1.5 [1.20].

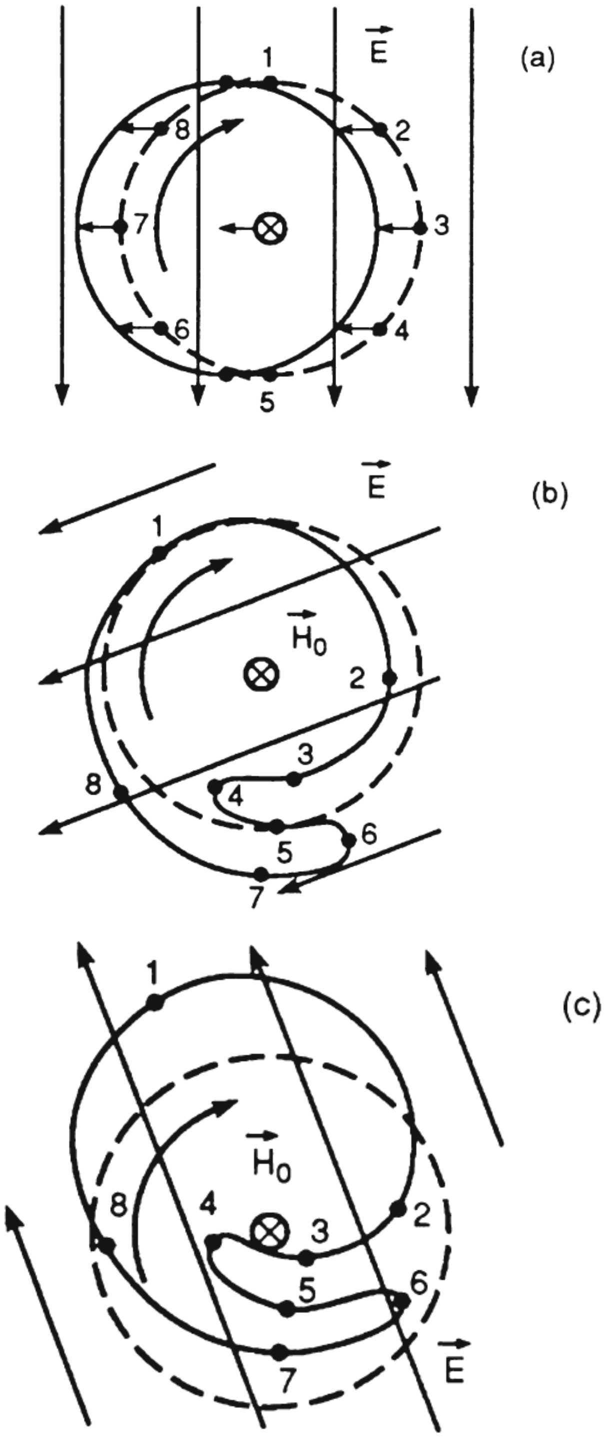

Figure 1.5 The pictorial illustration of the process of the interaction of electrons with an electromagnetic wave. a) Energy modulation, b) orbital bunching and c) deceleration of the bunch, reproduced from [1.20].

The field of gyrotron research is well developed. The number of published papers describing various aspects of theory describing the device, numerical and experimental studies of its operation and its different components exceeds several thousand with more than a thousand contributors. For more than fifty years of research the device characteristics significantly improved. At the dawn of the gyrotron development the output power of the first device in the continuous operating regime did not exceed 200W at 25GHz[1.12]; as at now, the modern gyrotrons designated for electron cyclotron resonance plasma heating operate at 140 -170 GHz with output about a megawatt in continuous mode [1.22]. To achieve this operational milestone a number of scientific and technological challenges had to be overcome. These challenges included, but were not limited to the following aspects:

- development of number of theories to properly describe various aspects of the device operation [1.12];
- development of numerical codes that allow one to simulate and optimize the geometry of the device under the study and make accurate prediction about operation parameters;
- overcoming a significant number of engineering problems in the design of various gyrotron components.

For instance, to achieve output powers on the order of one megawatt the following technological challenges had to be resolved:

- realization of the stable operation at high order working modes;
- effective energy output;
- development of novel magnetron injection guns;
- development and utilization of novel superconducting mangetic systems;
- analysis of depressed collectors;

- invention and utilization of chemical vapor deposition (CVD) diamond windows.

These aspects put gyrotron research on the front edge of modern science and technology. Recently, another item was added to the list of the possible gyrotrons applications. This class of the devices, due to their unique physics, is among few sources that are capable of delivering high power microwave raidiation in the terahertz region. The expansion of the gyrotrons into this field imposes additional requirements on the device geometry thus presenting additional techonological challenges during manufacturing, assembly and operations. These topics had to be addressed and resolved during the theoretical and experimental studies of the 670GHz device operating at fundamental harmonic, which needs magnetic field close to 27T.

The development of the scheme was started as one of the tasks under the umbrella of the AppEL program, which is a long term collaboration between the University of Maryland and Office of Naval Research. The tube development was performed in collaboration with the Institute of Applied Physics of the Russian Academy of Science (IAP RAN). This institute is one of the pioneers[1.21] in the gyrotron development and retains a leading role in the research of various microwave devices[1.12]. Due to the IAP team expertise and experience in tube development and availability of modern manufacturing facilities the task was divided in the following way. The University of Maryland team concentrated on the developing of the interaction circuit and various diagnostics, while IAP team concentrated on the design and manufacturing of the electron gun, anode, magnet and the magnet power supply.

The novelty of this tube, i.e. the fact that the tube was operated at a frequency that is much higher that is typical for gyrotrons, led to a number of additional requirements imposed on the device. Typically, for any tube the following issues should be addressed:

- Creation of the electron beams that have high orbital energy and optimal orbital-to-axial electron velocity ratio.
- Optimization of the interaction circuit to achieve maximum efficiency
- Heat management of the system and spent beams
- Converting the output radiation and extracting it from the device in a way that maximizes the efficiency of the tube.

The outlined problems are addressed in any gyrotron design, but reduced size of the interaction circuit at higher frequencies makes the successful development of the tube extremely challenging. The additional challenges include:

- Stable generation of the operation mode in oversized resonator;
- Generation of strong magnetic field in the required region of space;
- Proper handling of Ohmic losses in the electrodynamical system;
- Addressing the issue of magnetic field penetration through the metallic walls of the system.

It should be stressed that for this operating frequency it was not possible to use a conventional or superconducting magnet to generate required magnetic field; thus, a pulsed magnet was utilized for the tube operation. The novelty of this gyrotron as well as most of the challenges that had to be overcome in the course of its operation stemmed from the necessity to use this pulsed solenoid [1.16]. Those issues are elaborated in much details later in this chapter.

The Figure 1.5 shows a photograph of the assembled tube and its crossection. The device has vertical arrangement. The electron gun, high voltage feeds and the feeds for the heater are located at the bottom of the assembly. The Dewar that encloses the solenoid also serves as the mounting post for the system, i.e. three support rods that are attached to it, allows the tube to be located and aligned on the experimental table. Located close to the gun are pumping port and the input for water that cools the system. The body of the anode with the magnet wound on it and the magnet outputs connections are shown on the top of the structure. Finally, the output window of the gyrotron with the flange assembly is at the top of the tube assembly.

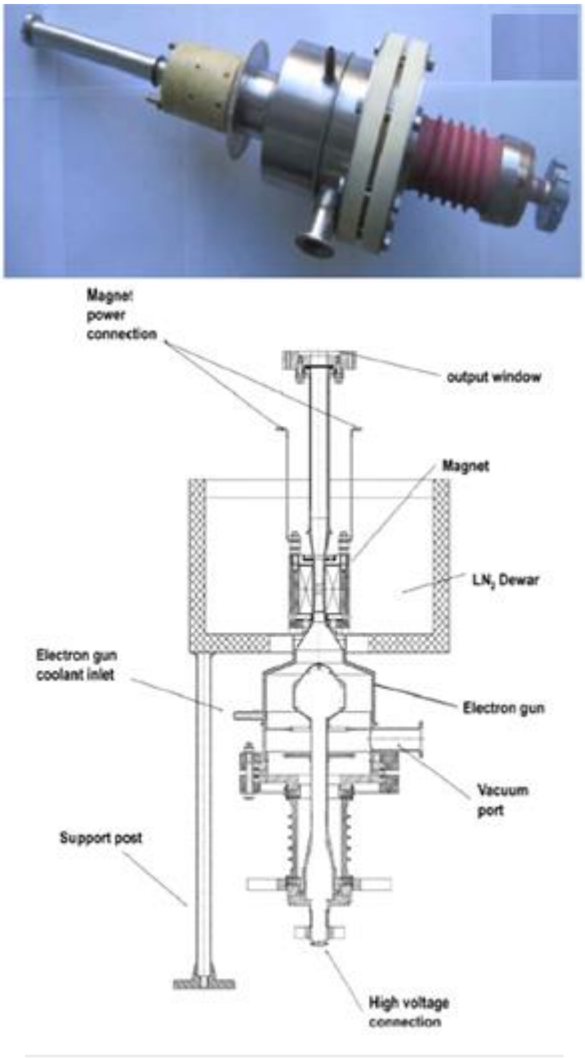

Figure 1.6 A photograph of the assembled tube without a Dewar and the tube's section view.

Having described the basic tube component I will now give further details describing the tube components and the experimental activities that were required to achieve the calculated parameters. Since several tube components needed to be modified and adjusted in order to ensure the optimal operation of the device.

1.5 Gyrotron components design

1.5.1 Operating frequency

Interest in using the tube for remote sensing of radiation put certain restrictions on the operating frequency and other parameters of the device. Earlier in this chapter the reasons for choosing the operating frequency were given. They were governed by the necessity of utilizing the tube for remote detection, i.e. the atmosphere should be relatively transparent at frequency. The other consideration that was taken into account is that there were, in fact, some source development activity at this frequency sponsored by DARPA [1.25], which could potentially lead to additional collaboration and cross benefit the performed research.

1.5.2 Operating mode and Efficiency Calculations

The choice of the operating mode is closely related to the task of calculating the efficiency of the tube. Gyrotrons typically operate in high order transverse electric TE modes. The excitation of these high order modes near cutoff allows the electron axial momentum to remain almost constant during the process of electron beam interaction. It is also preferable to operate the tube operates at very high order modes, when the operating frequency of the device is high, such is the case for the device under the consideration, i.e. 670 GHz. The operation of the device in these high order modes allow one to reduce the losses of the power in the cavity walls and greatly increase the efficiency. In order to achieve power levels sufficient for the scheme to operate the close attention to the device efficiency is appropriate.

In order to calculate the efficiency of the tube the following approach was used. First, the linear theory [1.20] was used to obtain a preliminary estimates of the tube efficiency, then the numerical analysis employing available numerical codes [1.26] was used to optimize the geometry to maximize output efficiency.

The electrons in the beam radiate the power which is distributed between the power of outgoing radiation and the ohmic loses. If W denotes the energy stored in the resonator these powers are equal to $P_{out} = \left(\frac{\omega}{Q_D}\right)W$ and $P_\Omega = \left(\frac{\omega}{Q_\Omega}\right)W$, i.e. they are inversely proportional to the diffractive and ohmic quality factors, Q_D and Q_Ω. For preliminary estimates the following formulas can be used:

$$Q_D = 30\left(\frac{L}{\lambda}\right)^2, \tag{1.11}$$

where L is the length of the resonator, and λ is the operating wavelength, and

$$Q_\Omega = \left(R_w / \delta\right)\left(1 - m^2 / \nu_{m,p}^2\right)^2, \tag{1.12}$$

where R_w is the resonator wall radius, $\delta = \left(1/2\pi\right)\sqrt{\lambda c / \sigma}$ is the skin depth (σ is the conductivity of the wall and c is the speed of light) and $\nu_{m,p} \approx 2\pi R_w / \lambda$ is the eigennumber of the $TE_{m,p}$ mode. Assuming that surface roughness reduces the conductivity of copper to make it two times smaller than the tabulated value, the number equal to 1.1 μm gives a good estimate for the skin depth at 670 GHz.

The output efficiency is then given as:

$$\eta_{out} = \left(\frac{Q_\Omega}{Q_D + Q_\Omega}\right)\eta_{\text{int}}, \tag{1.13}$$

where η_{int} is the interaction efficiency, which is defined as:

$$\eta_{\text{int}} = \left(\frac{\beta_{\perp 0}^2}{2\left(1 - \gamma_0^{-1}\right)}\right)\eta_\perp. \tag{1.14}$$

In the last equation $\beta_{\perp 0} = v_{\perp 0} / c$ is the initial orbital velocity normalized to the speed of light, $\gamma_0 = 1 + eV_b / mc^2$ is the Lorentz factor determined by the operating beam voltage V_b and $\eta_\perp$ is the orbital efficiency that characterizes the fraction of electron gyration energy that is transformed into electromagnetic radiation. The orbital efficiency depends on three normalized parameters:

normalized length $\mu = \pi\left(\beta_{\perp 0}^2 / \beta_{z0}\right)\left(L / \lambda\right)$;

normalized cyclotron mismatch $\Delta = \dfrac{2}{\beta_{\perp 0}^2} \dfrac{\omega - s\Omega_0}{\omega}$;

normalized beam current parameter $I_0 = 0.238 I_b(A) Q 10^{-3} G \dfrac{\lambda}{L} \left(\dfrac{s^s}{2^s s!} \right) \dfrac{\beta_{\perp 0}^{2(s-3)}}{\gamma_0}$.

The numerical coefficients in I_0 is given for the Gaussian beam profile.

In this definitions the parameters have the following meaning β_{z0} is the normalized axial velocity, ω is the operating frequency, Ω_0 is the initial electron cyclotron frequency, I_b is the operating current in amperes, Q is quality factor of the resonator, G is the coupling factor to the operating TE mode and s is the cyclotron harmonic.

The operational mode was chosen to be $TE_{31,8}$. The stable operation of the specified mode in (MW)-class gyrotrons was shown in the recent experiments [1.27]. The initial estimates of the efficiency were carried out with the help of formulae (1.11-1.14). The operating voltage and beam current of the gyrotron are equal to 60-70kV and 15-20A respectively. This beam power, which is in the excess of 1MW is necessary to obtain 200-300kW of the radiated power.

The radius of the beam should be chosen in such a way that the electrons provide maximum coupling to the operation mode in the resonator. This coupling is determined by the factor:

$$G_{m,p} = \frac{J_{m\mp 1}^{2}\left(\nu_{m,p} R_b / R_w\right)}{\left(\nu_{m,p}^{2} - m^{2}\right) J_m^{2}\left(\nu_{m,p}\right)} . \tag{1.15}$$

The dependence of $G_{m,p}$ on R_b / R_w is shown in figure 1.6.

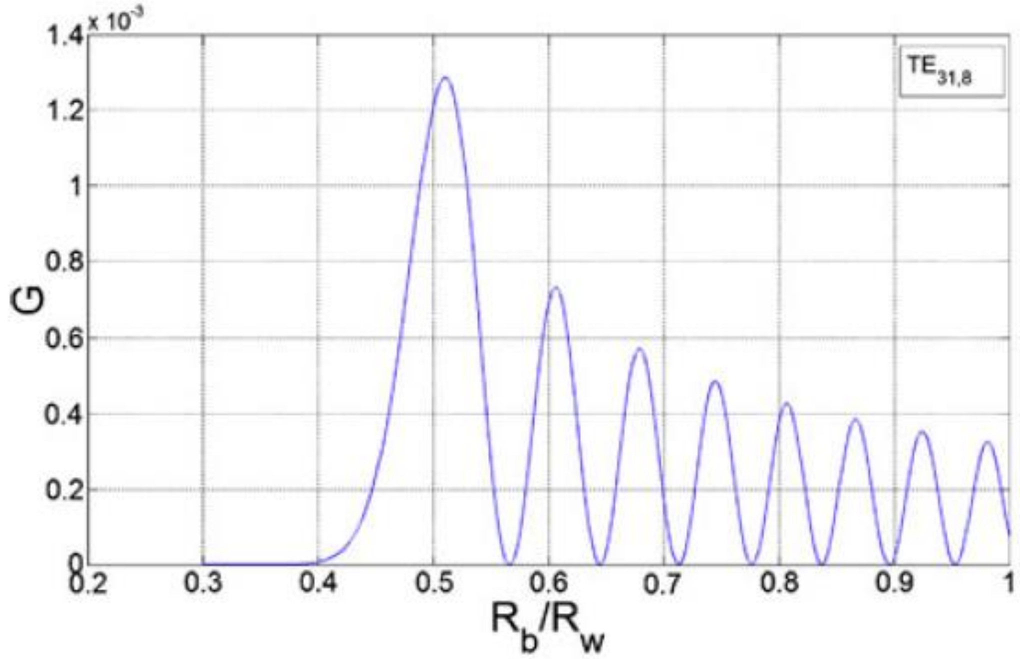

Figure 1.7 Coupling factor $G_{m,p}$ for the mode $TE_{31,8}$.

The ratio of the orbital-to-axial velocity which is defined as the ratio: $\beta_{\perp 0} / \beta_{z0}$ is equal to 1.3-1.35. This ratio is typical for gyrotron guns. The analysis of the gun was performed at University of Maryland[1.28] and IAP and the resulting gun geometry and parameters were obtained. The magnetic compression ratio, which is defined as $\alpha_B = {}^{B_0}\!/\!_{B_{cath}}$, i.e. the ratio of the magnetic field inside the resonator to the field at the cathode; for the required beam voltage of 60-70kV and under the assumption that the field on the cathode has typical value of 4kV/mm [1.24] the compression ratio is close to 88, which is quite large for a gyrotron gun. The cathode radius of the designed gun is equal to 2.15 cm. To achieve the beam current of 20A and assuming moderate cathode loading of 4 A/cm^2 the width of emitter was calculated to be 3.7mm. Typically, in order to avoid efficiency degradation, the spread in the guiding centers should not exceed 1/6 – 1/4 of a wavelength; for the chosen operation frequency this corresponds to the range 0.07mm to 0.11mm. The radial spread of electron guiding centers in the resonator is calculated to be 0.14mm, which corresponds to 0.3λ. It will be shown later in this chapter that even this spread will not significantly degrade the performance of the device.

1.5.3 The tests for uniformity of the emitter

The initial tests performed with the tube revealed that in order to adjust the orbital to axial ratio of the electron velocity the cathode should be moved further away from the anode. The demountable design of the tube allowed to perform this task by disassembling the vacuum seal and inserting a spacer ring. The original design supplied the device with three spacer rings with different thickness, having the following values: 5mm, 5.5mm and 6mm. Two additional spacers were machined with required tolerance from a recycled 12inch vacuum flanges; 316L stainless steel ensures that these manufactured spacers provide good vacuum in the system without leaking or outgassing. In subsequent tests generation of the electromagnetic radiation improved. However, it was necessary to recondition the emitter, since in the course of these tests the tube was brought up to atmospheric pressure ten times, which led to contamination of the emitter ring.

It is know that LaB_6 emitters can be reconditioned to restore the emission properties of the cathode. In particular, the way the emitter ring is designed for this tube allows the migration of fresh crystals of the LaB_6 to the surface of the emitter, effectively restoring the emission properties of the gun. In order to perform testing, the cathode was removed from the gyrotron and was mounted into the gun stand. The gun stand was available from previous experiments on a 17GHz gyroklystron [1.29]. This is a state of the art device that includes a multiport vacuum chamber that can host the original gyroklystron gun, and provided the pumps and the circuitry to feed and control power in a required and safe manner, i.e. having circuitry to protect the gun in the case of power failure and so on.

In order to perform the experiments on the 670GHz gyrotron gun a number of changes were made to the test stand assembly. First, the circuitry that controls the stand was modified to be able to operate the gun in the required regime, which included the installation of relays and switches and a transformer capable of supplying 250Watt of DC power to the heater of the gun from the stand power supply. In order to mount the gun onto the stand, an adapter was again manufactured from the blank vacuum flange. The adapter had bolt mounts and the special groove, so it was possible to utilize the original gun assembly along with the original gaskets, thus allowing one to keep the vacuum inside the chamber at the level of $5 \cdot 10^{-7}$ Torr, as was measured by an ion gauge. The vacuum level in the stand was much better than the vacuum measured in the experiments, thus improving the efficiency of the procedure of gun reactivation.

After the gun was put in the stand and power in excess of 250Watt was applied to it, it was conditioned for several days. The necessity of reconditioning the gun allowed an additional test of the gun be performed. The uniformity of the emitter ring was tested using of the two color pyrometer Mikron 77. The temperature of the gun was measured through one of the chamber ports. The emitter ring was divided into 16 parts and the temperature of each segment was recorded. A special stand to mount and adjust lateral and vertical position of the pyrometer was manufactured. This holder allowed precise control of both lateral and vertical position. The emitter has shown good performance with temperature deviation from the mean was less than one percent.

The results of the experiments measuring the performance of the emitter are shown in the Figure 1.8.

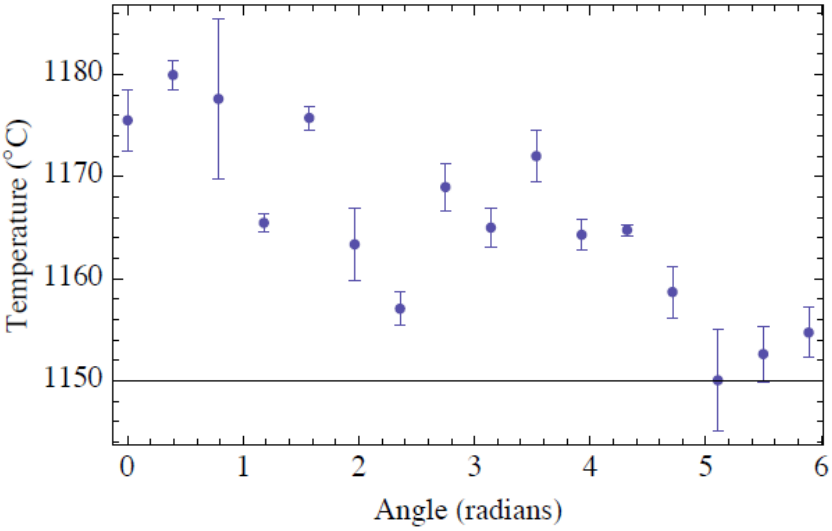

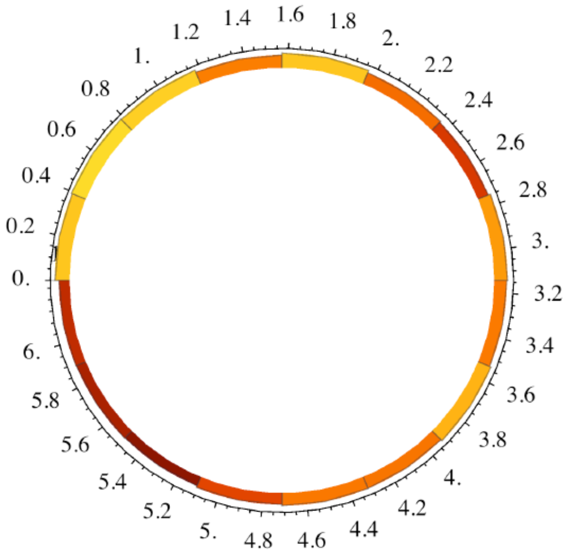

Figure 1.8 a) The temperature distribution of the emitter as a function of the angular coordinate. b) The azimuthal distribution of temperature at the cathode ring, the color varies from 1150 to 1180C.

1.5.4 Pulsed Solenoid

Simple estimates show that in order for the device to operate at the fundamental harmonic at the chosen frequency the magnetic field should be close to 28T. Commercially available superconducting magnets [1.30] can readily provide the fields of the order of 15-20T, however, as the values of magnetic fields are increased further than these values, the cryo-systems become prohibitively expensive. One solution to achieve such high magnetic field in gyrotrons is to utilize pulsed solenoids. The first results of the experiments with sub-terahertz gyrotrons were performed almost thirty years ago [1.31], however the limitations of solenoid manufacturing technology delayed a practical realization of these tubes for about twenty years. Only recently researchers in Russia [1.32] and Japan [1.33] developed the gyrotrons that were capable of operating at terahertz frequencies and produce significant amount of electromagnetic power output. The tube studied in the recent experiments in IAP RAS demonstrated that it is possible to operate the tube at 1THz frequency utilizing a solenoid with inner diameter of 6mm capable of producing up to 40T magnetic field [1.34]. The design of this gyrotron and the specifications of the solenoid were taken as a basis for the 670GHz gyrotron.

These terahertz tubes were taken as a starting point of the design of a new magnet with inner and outer diameters of 17.5mm and 41mm respectively for the gyrotron. The solenoid is directly wound onto the body of the tube (the section of the anode where the magnet is located is a stainless steel pipe of 0.5mm wall thickness and 16 mm in diameter). This arrangement of the system helps with the alignment of the solenoid with respect of the axis of the tube and significantly increases the mechanical stability of the system. The solenoid winding is made of the material that is typically used in the manufacturing of the cryomagnets. This is the wire made of a 40% Nb-60% Ti alloy with copper outer shell, that supports and reinforces the windings. The particular geometry of the wire is as follows: it has rectangular shape with dimensions 3x1 mm^2. This geometry allows one to achieve almost 80% filling factor for the solenoid. Each layer of the wiring is covered by an epoxy layer for electric insulation and the entire assembly is enclosed in a 15 mm textolite glass bandage to further reinforce the structure. The other feature of this solenoid design is that in order to further stabilize the reproducibility of the output signal and reduce the energy requirements for the charging unit, the solenoid during operation is immersed in the liquid nitrogen. The magnet is enclosed in a Dewar. The Dewar is made from the textolite sheet with a copper layer on it to solder directly to the gyrotron body. When the system is filled with liquid nitrogen, the resistance of the coil is reduced from 0.07Ω, measured at the room temperature to 0.01Ω. The solenoid coil has the following parameters:

- the inductance of the solenoid is equal to 0.335 mH;
- solenoid constant is equal to 34Oe/A;
- at the nominal voltage of 3.1-3.15kV, the current in the solenoid is equal to 8kA
- this voltage allows one to achieve magnetic fields exciding 28T.

The picture of the test solenoid and the one mounted on the anode of the gyroton are shown on the figure 1.9.

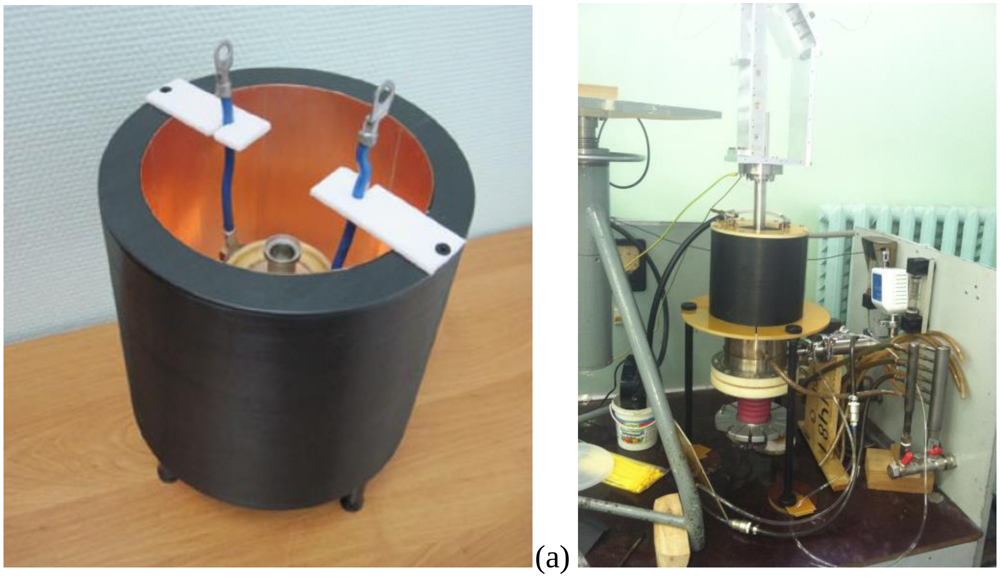
(a)

Figure 1.9 The test solenoid (a) and the solenoid mounted on the device (b)

1.5.5 Pulsed solenoid power supply

In order to achieve stable operation of the gyrotron the solenoid current from pulse to pulse should not differ by more than 0.1%. In order to achieve such a high degree of reproducibility a careful design of the pulse solenoid power supply should be performed. The schematic of the power supply used in the experiment is shown in figure 1.3. The charging block consists of three 6 kV capacitors (K75-100) with 1,100 μF capacitance each. These capacitors are connected in parallel (this connection is denoted as C in figure 3). The discharge of the energy accumulated in the capacitors is controlled by a thyristor switch (denoted VS on the schematic). The charging block (CCPS4000), consisting of a high-frequency transistor converter, with dozing capacitors; the transformer output allows the capacitors to be charged to nominal voltage in the range from 0.5kV to 3.8kV with the target pulse to pulse variability of the current less than 0.1%.

In the course of operation, in order to obtain the required value of the voltage the capacitors should be charged to the voltage $V_{ch} = \mathrm{I}_{max} \sqrt{L_s / C} \exp\left(-\pi / 2Q\right)$ where $Q = \sqrt{L_S / C} / \left(R_0 + R_S\right)$ is the circuit quality factor. In this formula, R_0 is an equivalent resistance of the circuit taking into account the losses in the contacts, capacitors and the thyristor. The experimental testing of the power supply showed that the value of the circuit quality factor is close to 3. The ohmic heating of the coil causes severe problems for the solenoid operation. To overcome those, a crowbar circuit that consists of a diode and a resistor R_{cr}, such that $R_{cr} \gg R_s$ is added in parallel with the capacitor. The nominal value of the resistor is 0.1 *Ohm*, and the corresponding energy dissipated in each pulse being on the order of $W_{cr} \approx L_s I_{\max}^2 / 2\left(1 + R_s / R_{cr}\right)$, the dissipated energy at the maximum nominal voltage can reach 15kJ. Thus, the resistor was made from a stainless steel tube with 10 mm outer diameter and was cooled by forced air. The total weight of the power supply is about 195 kg and the dimensions are $0.55 \times 0.78 \times 1.18 m^3$. The testing and experiments performed with the power supply showed that the device performance satisfies the required specifications.

Figure 1.10 shows the time dependence of the solenoid current. In order to cut the current at the quarter of the period a crowbar circuit is added in parallel with the capacitor bank. The next figure (1.11) shows an example of the trace of the solenoid current, as measured by a voltage monitor and a picture of the power supply.

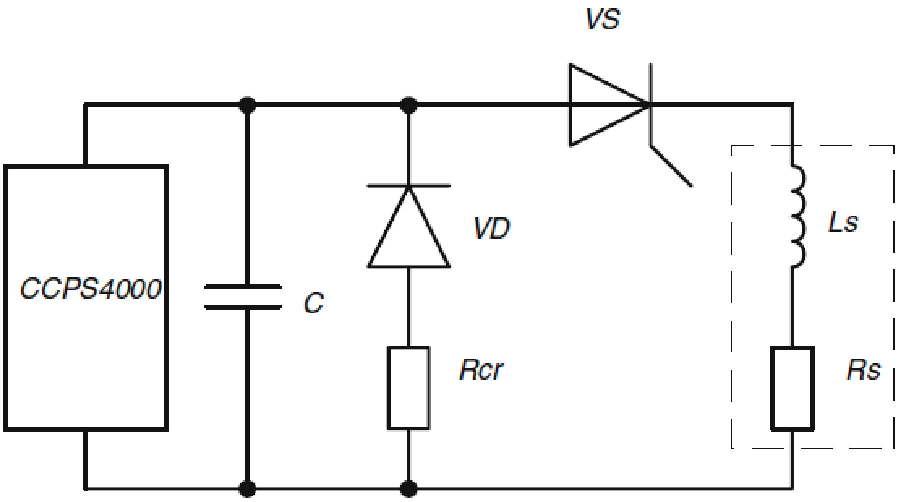

Figure 1.10 The schematic of the pulsed magnet power supply

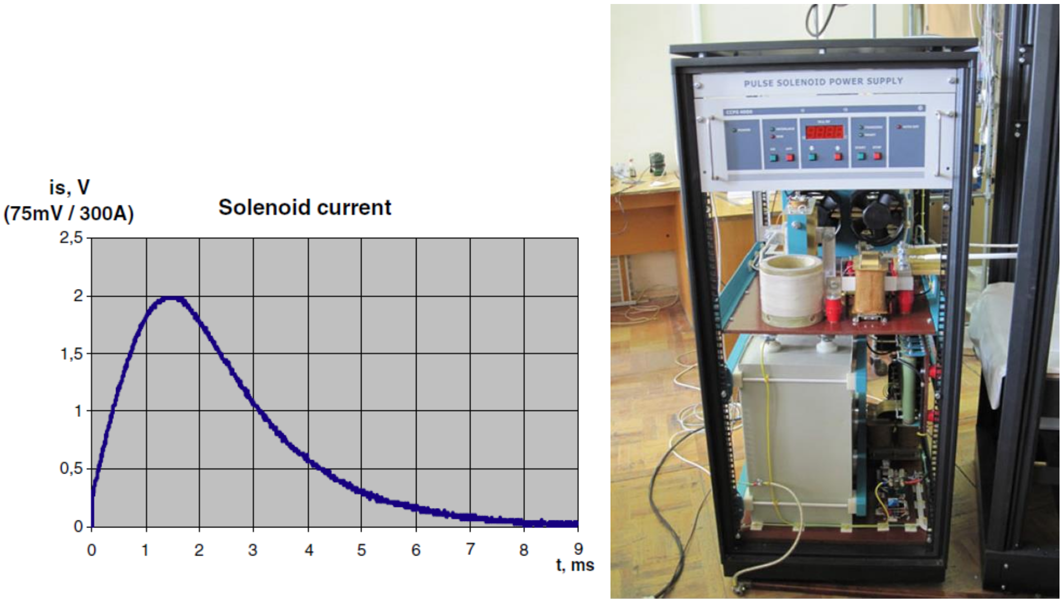

Figure 1.11 (a) Time dependence of the pulsed solenoid current, (b) Pulse solenoid power supply

1.5.6 Calorimeter

The measurements of the frequency of a gyrotron operating in the pulsed regime is a challenging task that is complicated by a number of factors, such as frequency shift and/or instability of the magnetic power supply.

The most reasonable way to proceed is to calibrate the gyrotron solenoid at the lower magnetic fields; i.e. at the lower currents and then measure the output frequency of the radiation based on this calibration.

A Hall effect sensor was used to measure the magnetic field inside the coil. A modification of the Mitutoyo Height Gage was used to mount the Hall sensor allowing for precise control of the position of the sensor inside the interaction circuit. A vector network analyzer connected through the audio amplifier allowed for measuring the parameter $S_{2,1}$ which corresponds to measuring the magnetic field by a Gauss meter. These results, along with the calibration of the solenoid power supply show, that in order to obtain a magnetic field of 28T the power supply should be charged to 3.5kV.

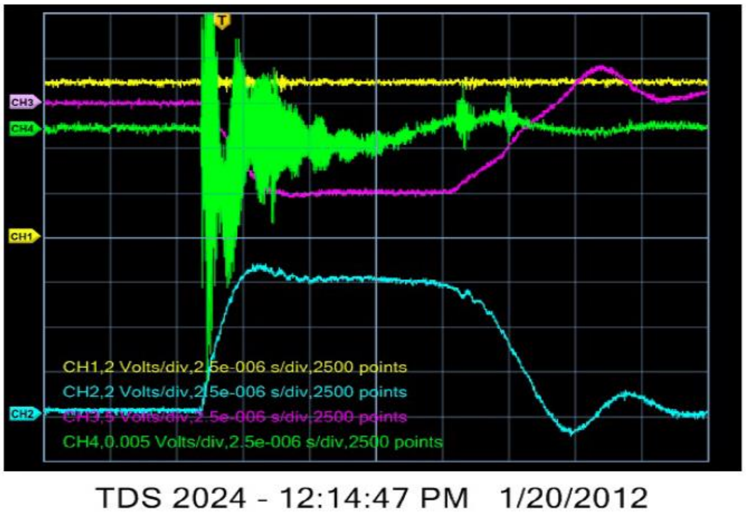

Figure 1.12 The trace of voltage (purple), current (cyan) RF trace (green) and the signal from magnet power supply (yellow).

The radiated power was converted into a Gaussian-like wave beam with the use of the standard Vlasov quasi-optical converter and focused with a parabolic mirror. The radiation was focused by a parabolic mirror and reflected in such a way that it propagates in a direction perpendicular to the axis of the gyrotron.

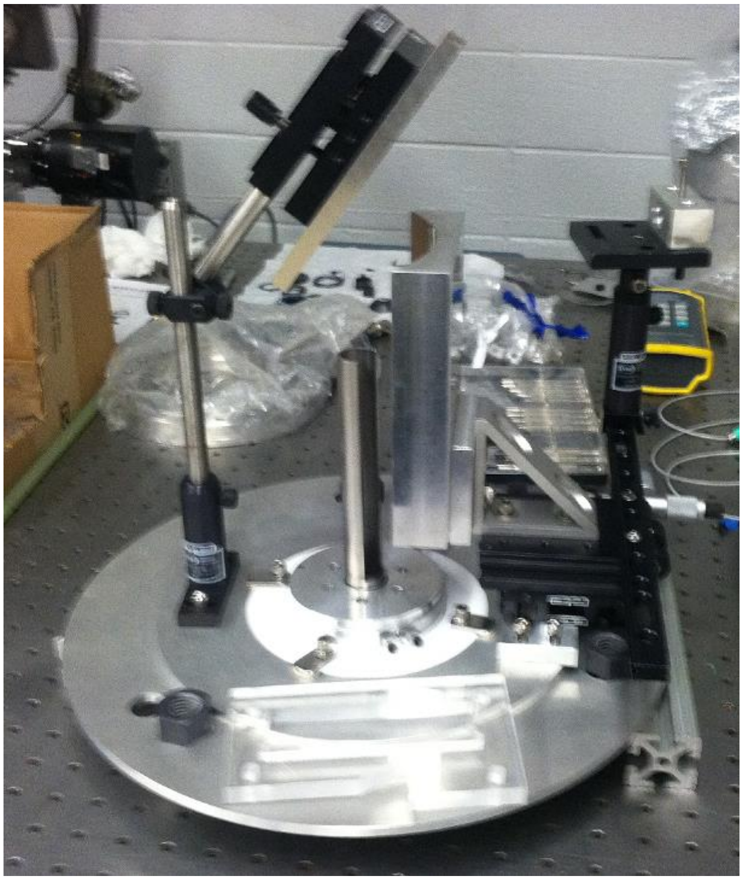

Figure 1.13 The quasioptical converter and parabolic mirrors that were used in the experiment.

A solid state radiation detector was used in the experiments to detect the presence of the terahertz radiation from the source. However, the available detectors were not designed to quantify the frequency and power of the gyrotron under the consideration. However, the detector was used when it was needed to detect the radiation and quantifying the shape of the output radiation envelop.

The task of measuring the radiation at this frequency requires specialized diagnostic. The standard method is to use a solid state calorimeter [1.34], which uses thermocouple to measure the deposited pulse. This approach requires, however, that thermal equilibrium is established in the calorimeter. This approach, is more attainable in gyrotrons that operate in the continuous mode.

Since this gyrotron operates at the pulsed regime another method of detecting the energy of the radiation pulse was used, first developed and used by A.G. Shkvarunets [1.35]. The principle of operation of this device is to measure the thermal expansion of a certain liquid that absorbs the energy of sub-THz radiation. This method has a major advantage, since this calorimeter is a broadband device, i.e. it absorbs all the energy of the pulse over a wide range of frequency. The body of the calorimeter is made from delrin plastic that providees rigidity. The radiation entered the device through a thin Teflon film that has good transparency for the radiation at the given frequency. The calorimeter was filled with liquid that has good absorption of the terahertz electromagnetic radiation. As the working media hexane and ethanol was used and it was found that the performance of the calorimeter is similar for both working liquids; thus it was decided to use ethanol in further experiments. The calorimeter was calibrated by supplying a pulse with energy of one Joule through the wire installed inside the calorimeter. The calorimeter has a thin tube attached to it, this tube is connected to the main reservoir containing the working liquid. As the energy of the pulse is absorbed the thermal expansion of the liquid causes the meniscus to rise, and the displacement of the meniscus is readily registered by a high resolution camera and recorded by a video digitizer to be stored in a local computer.

A view of the calorimeter and a result of the generic measurement are shown in the figure 1.14. In the figure the level of the liquid is shown to slowly drift with time and after the pulse is recorded a sharp rise is observed, the height of the step corresponds to amount of energy in the pulse.

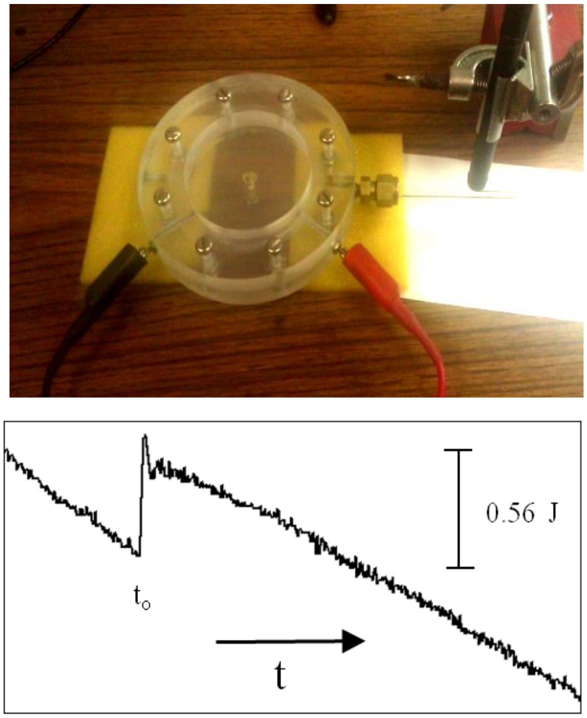

Figure 1.14 The view of the calorimeter. And the result of the measurement of the radiation where power in excess of 130kW was measured in 0.56J pulse.

The energy distribution of the beam was measured by an infrared scanner to quantify the beam structure. The experiments have shown that the radiation can be effectively transported to the distances of up to 10 meters, at which point the diameter of the beam spot at the focal plane is 4mm. It should be noted, that this value is rather small, due to several reasons. Firstly, the efficiency of the mode converter was estimated to be 50%, due to the transformation of the operating modes into other types of oscillations in the process of propagation from the resonator to the output window. This can be addressed by performing a careful analysis of the modal composition of the output radiation and a better design of the converter. Secondly, the power of the outgoing radiation measured in these experiments was only 100kW, by increasing the power of the outgoing radiation this problem can also be addressed.

The next section of this chapter is concerned with numerical analysis of the gyrotron resonator. The initial numerical analysis of the device efficiency was done long before the arrival of the device to UMD [1.36]. This analysis have shown that a properly designed resonator can achieve an overall efficiency in excess of 35%. But once the initial testing of the tube after its arrival at UMD was done, the need to design a resonator with even higher efficiency was apparent.

1.5.7 Optimizing the resonator geometry

The original design studies explored extensively the role of the angles of the tapered sections of the resonator. The initial experimental results of the tests performed in the Institute of Applied Physics showed that the elongation of the straight section of the resonator led to increase of efficiency. However, extensive elongation of the interaction section may lead to the deterioration of the output efficiency. The goal of the studies was to find the optimal efficiency, develop the tools and procedure to manufacture the resonator and test the performance of the resonator in the available tube at IAP RAS.

The original design of the resonator has length of the straight section equal to 3.85 mm. It was chosen as the basis for the further investigations. The preliminary estimates were performed in the framework of the linear theory as shown by formulas (1.12 – 1.14). Based on these formulas, rough estimates of the resonator efficiency can be made. Assuming that the surface roughness in the cavity reduces the conductivity by a factor of two, the skin depth at this frequency is equal to $1.1\,\mu m$. The ohmic quality factor of the cavity Q_{ohm} is according to (1.12) is equal to 30000. Taking the ratio of the resonator length to the wavelength to be ten, i.e. $L/\lambda = 10$ we get the diffractive quality factor is equal to 3000. For the mode $TE_{31,8}$ and the beam current of about 15-20A and the value of the normalized beam parameter close to optimal, the orbital efficiency is close to 66%. Then, the overall efficiency of the device is close to 35%.

The task of performing numerical simulations of fast wave devices requires special numerical tools. For instance, the usage of PIC codes is not justified, since it takes enormous amount of computational time and resources. To effectively simulate fast waves devices a number of computer codes were designed. Our group uses one of these codes, MAGY[1.26] which allows full time dependent description of the electromagnetic field and self-consistent analysis of the electron motion. The calculations of the electromagnetic fields and the corresponding quantities are based on the waveguide modal representation of the fields, which leads to significant reduction of the computational time, since instead of full system of Maxwell equations a relatively small number of coupled one-dimensional partial differential equations is solved.

The original study of the resonator has extensively dealt with the analysis of the taper angles and the size of the up-taper and down-taper sections. First, the analysis show that spurious modes can deteriorate the performance of the operating $TE_{31,8}$ mode. This is done in a series of so called “cold simulations” in MAGY. In these simulations a point source of $TE_{31,8}$ with Gaussian distribution in the middle of the cavity is assumed. The inclusion of the modes that the operating $TE_{31,8}$ mode can transform into (i.e. modes $TE_{31,7}$ and $TE_{31,9}$) allows one to estimate how much of the energy is converted into these modes due to the wall tapering. The results of the simulations show that for the basic design, the amplitude ratio for the spurious modes under consideration are less than 10^{-2} and 10^{-3} for $TE_{31,7}$ and $TE_{31,9}$ respectively.

It is well known, that the maximum of gyrotron efficiency occurs when the excitation takes place in the hard self-excitation region. Hard self-excitation occurs when there is a large slippage in the gyrophase with respect to the RF field, requiring large wave amplitude to trap the electron bunch. In order to practically realize this scenario in MAGY simulation a Gaussian source is placed inside the cavity which supplies the initial "kick" required for the self-excitation, this source is turned off after some time ($\sim 10ns$) to ensure that the self-excitation has occurred.

In the hot cavity simulation beam voltage was set to 70kV, beam current was set to 15A and the orbital-to-axial velocity alpha was set to 1.3. The magnetic field was chosen to be constant to reduce the computational time. The calculations were first performed to find the profile that yields the maximum efficiency and can be practically realized.

The dependence of the efficiency of the resonator as a function of the length of the straight section is shown in figure 1.15.

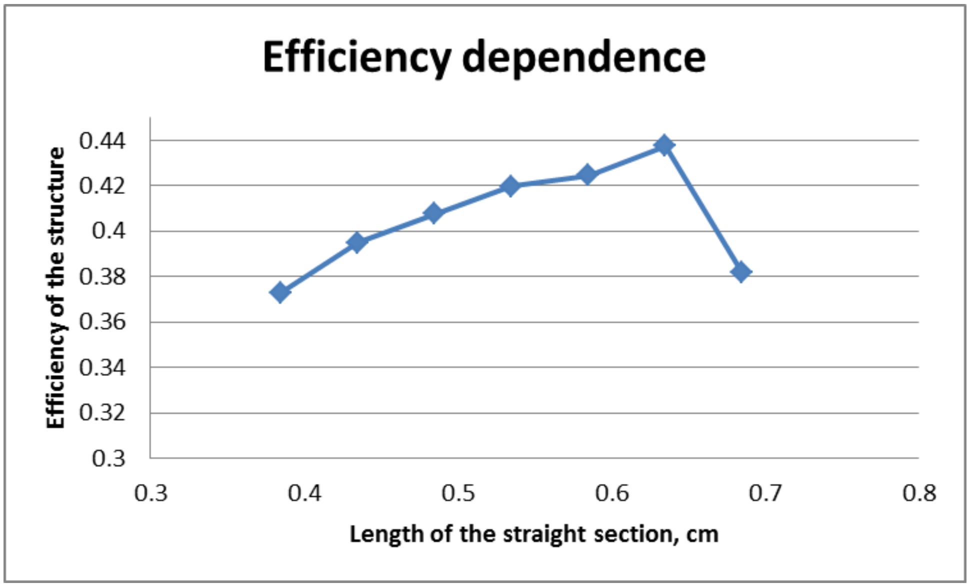

Figure 1.15 The dependence of the output efficiency as a function of the length of the straight section.

The figure shows that the overall efficiency of the resonator can be increased up to 44%. But there is another consideration that should be taken into account before any further analysis is of the profiles is performed.

The manufactured gyrotron tube design allows to quickly remove and replace the resonators. The resonator is combined with down-taper, cutoff section and up-taper section into single piece that is machined with high precision numerically controlled lathe.

The length of the entire section is 60 mm while the inner diameter of the piece varies, having the minimum value of 9.5 mm. Since it is known that the surface quality [] of the resonator plays one of the most important roles in the production of the output RF radiation it is imperative to achieve the highest surface quality. This requirement from a machining stand point of view means that appropriate tools should be used. The resonator is machined with a boring bar, which is a stiff tool that shapes the inner profile of the cavity. It is a challenging problem from a machining point of view since it requires some special tools.

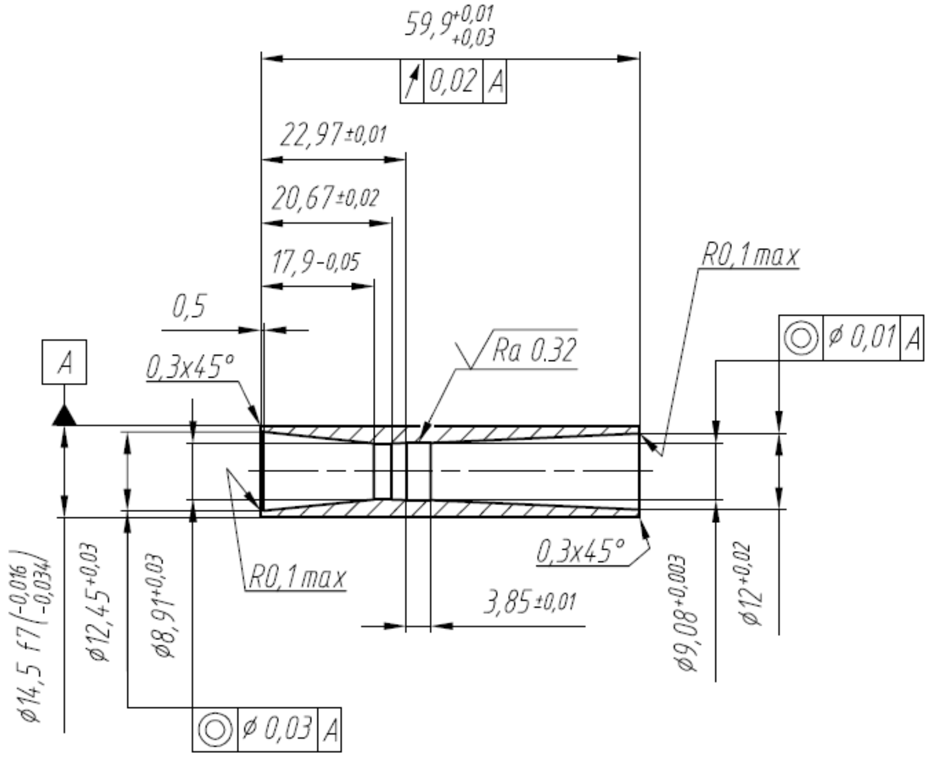

Figure 1.16 The mechanical drawing of the resonator.

This imposes certain restrictions on the equipment. Firstly, high precision tooling should be used, which includes CNC lathe with high precision chuck to keep the concentricity of the outer and inner profile of the resonator to the required tolerance. Also, as discussed earlier in this chapter, the optimal geometry of the resonator should meet two opposite requirements:

- the length of the resonator should be increased, to improve the output efficiency;
- the overall length of the uptaper and the straight section should not exceed the limit of the tool stiffness.

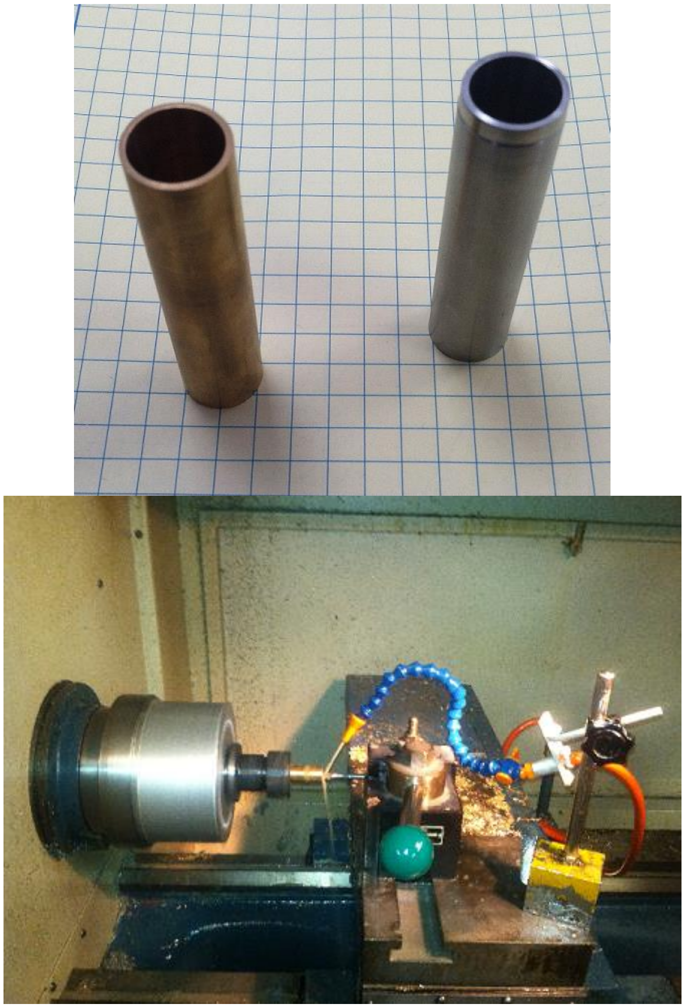

Figure 1.17 The manufactured resonators and the machining setup used in the manufacturing process.

To meet these requirements the length of the straight section of the resonator was chosen to be 5.75 mm. This geometry presents reasonable compromise between the output efficiency and the machining capabilities and the extensive analysis of this design was performed. The analysis of the efficiency of the resonator was performed in the presence of the spurious $TE_{31,7}$ and $TE_{31,9}$ were included into the simulations.

1.5.8 The comparison of the original design with advance simulation

As was described earlier, the maximum efficiency happens in the hard excitation regime. In the original studies by [1.36] it was shown that the effect of the after-cavity interactions leads to increase of the overall efficiency of the structure. In this analysis, instead of constant magnetic field along the entire structure, a more realistic profile of the magnetic field was chosen. The magnetic field is approximated by a parabola given by the following equation: $B(z)/B_{\max} = 1 - a\left(z - z_0\right)^2$. The numerical constants have the following values: $a = 1090.3\,\mathrm{m}^{-1}$, , and z_0 = 0.00475m.

This selected field profile is chosen in such a way that it corresponds to magnetic field profile inside the solenoid, obtained in the series of calibration experiments described earlier in this chapter.

1.5.9 The effect of the velocity spreads

For the profile under study calculations were carried out which included the effects of velocity spread (no guiding center spread was assumed). Simulations were performed to study the effect of velocity spread on structure efficiency. The simulations were set up to include root mean square (rms) velocity spread corresponding to 2.5%, 5% and 10%. Figure 1.18 shows the effect of the velocity spread on the overall efficiency of the structure. Velocity spreads reduce the peak efficiency from 42% to 41.5% in the case of 5% velocity spread and to 40% in the case of the 10% spread. Overall, the effect of the velocity spread does not play significant role in the efficiency deterioration, since even with 10% velocity spread, a total efficiency in excess of 40% can be achieved.

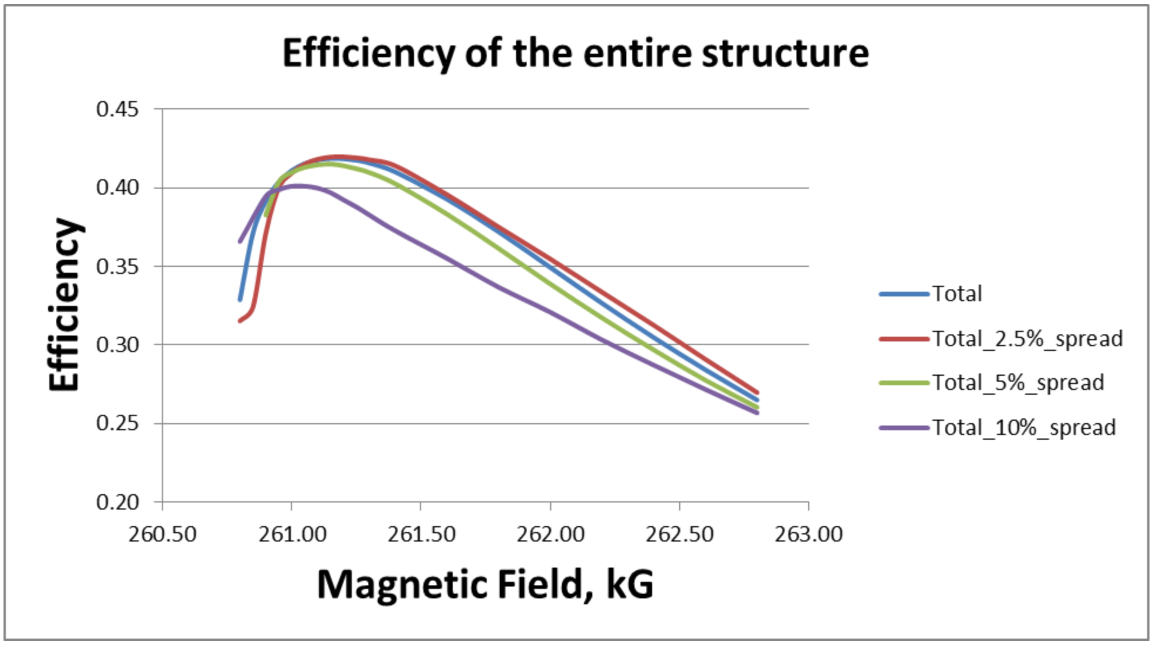

Figure 1.18 The effect of the velocity spread on the efficiency of the resonator.

1.5.10 The effect of the after cavity interactions

The inclusion of the after cavity region in the simulations has an effect on the total interaction efficiency. The wall radius in the after cavity region increases, along with the axial wave number k_z. When a constant magnetic field is assumed in the simulations, in this region the cyclotron resonance ($\omega = s\Omega + k_z v_z$) condition for a operating mode is no longer satisfied. When, on the other hand, the magnetic field is tapered, this condition may yet be satisfied for some values of parameters and additional interaction may take place, changing the overall efficiency of the device. Figure 1.19 shows the results of the simulations when the after cavity region is not included. This figure shows, that the effect of the after cavity interaction can improve the overall efficiency of the structure by several percent (comparing the figures (1.19) with the figure (1.18)).

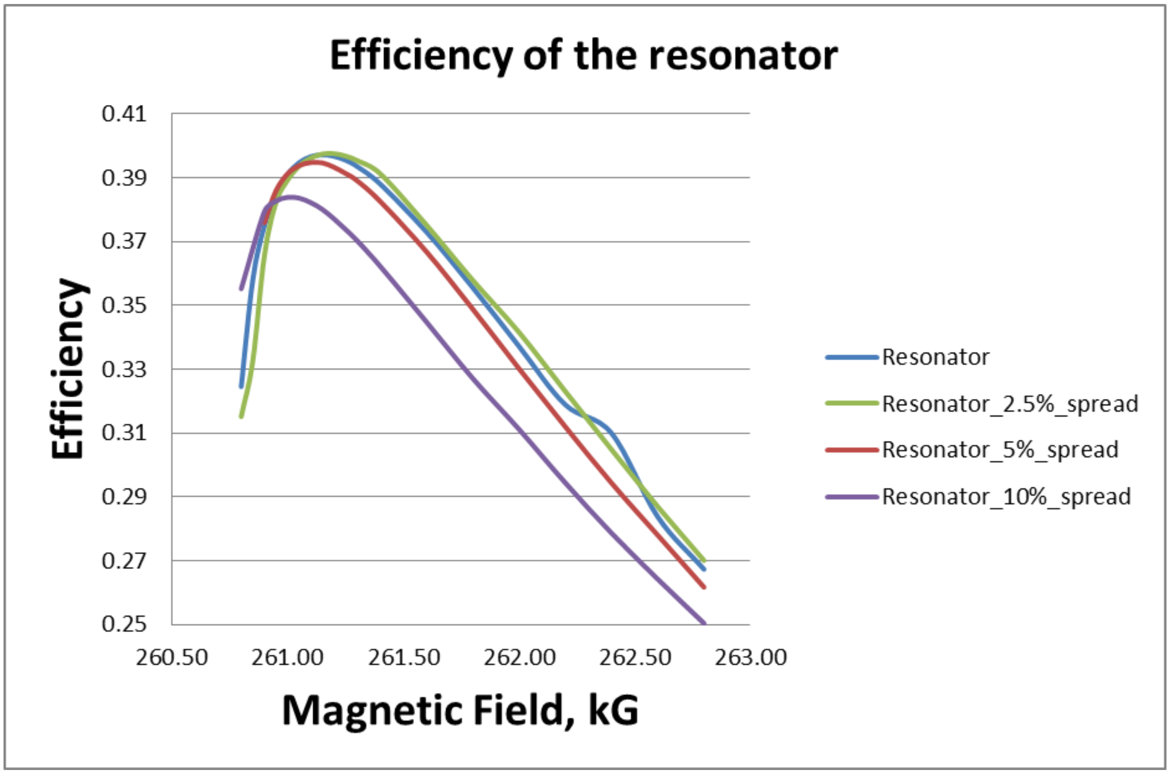

Figure 1.19 The efficiency of the structure without the up-taper section.

Since the gyrotron uses a pulsed solenoid there is another important issue that should be addressed in the simulations. Typically, in the gyrotron experiments, the length of the beam pulse is long enough, such that ionization occurs to compensate for the DC space charge field that is caused by the beam current. But in this design the requirement of using a pulsed solenoid puts a restriction on the beam pulse length. Namely, the length of a beam pulse should be significantly smaller than the length of a pulse that forms magnetic field in the solenoid. The calculations presented before did not take into account this effect. The results of the simulations with the inclusion of the voltage depression are shown in the Figure 1.20. The inclusion of this effect leads to a shift in the value of the optimum magnetic field and a slight improvement of the efficiency since the axial velocity is slightly decreased, due to voltage depression. This effect, however, only increases the efficiency by 0.5 percent.

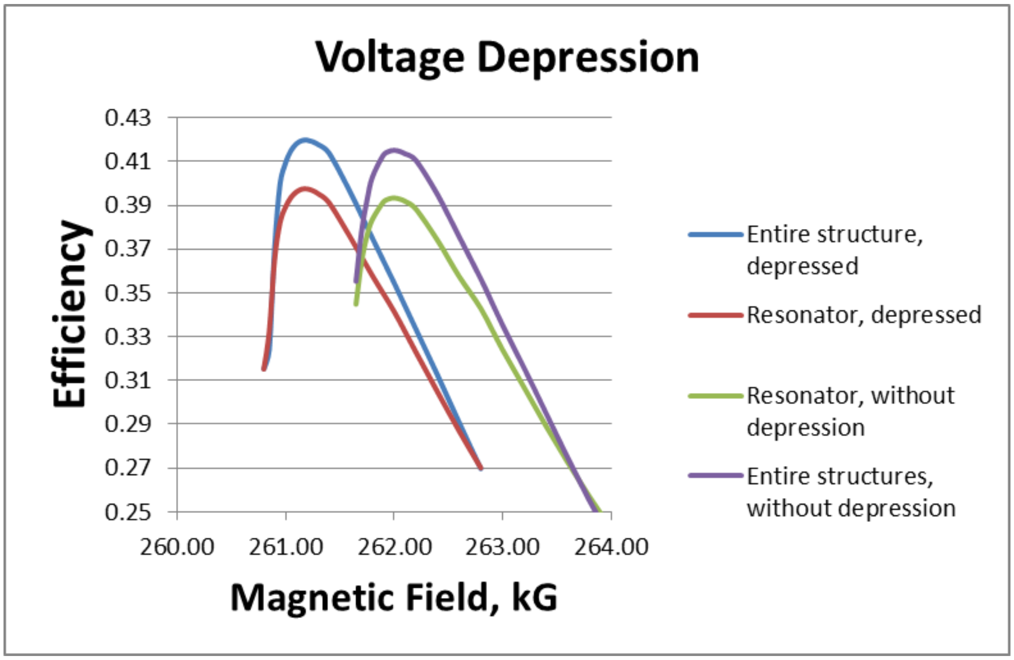

Figure 1.20 The efficiency with the inclusion of the voltage depression effect. The efficiency of the resonator and the total structure, in comparison.

Overall, the results of the experiment show that the elongation of the straight section of the resonator leads to a slight improvement in the resonator efficiency.

Two resonators were machined for the tests; one was made from stainless steel and the other from beryllium copper alloy, containing 2% beryllium. Since the solenoid is operated in the pulsed regime there can be a time lag between the maximum magnetic field in the solenoid and the maximum of the magnetic field in the structure, depending on the material of the resonator. This analysis was performed using a finite element code ELCUT, which is capable of providing the solutions of non-stationary electromagnetic problems. A 2D model of the gyrotron was simulated; an impulse of electric current was supplied to the solenoid windings, such that a sinusoidal field with maximum amplitude of 27 T and half period of $2.5\,\mu s$ (which corresponds to the field obtained in the experiment) was produced. The results of the simulations show that when the beryllium copper alloy resonator is used, the charging voltage on the magnetic field power supply should be increased about 20% and the time delay between the discharge of the capacitor bank and the beginning of the gyrotron pulse should be increased by 0.7miliseconds.

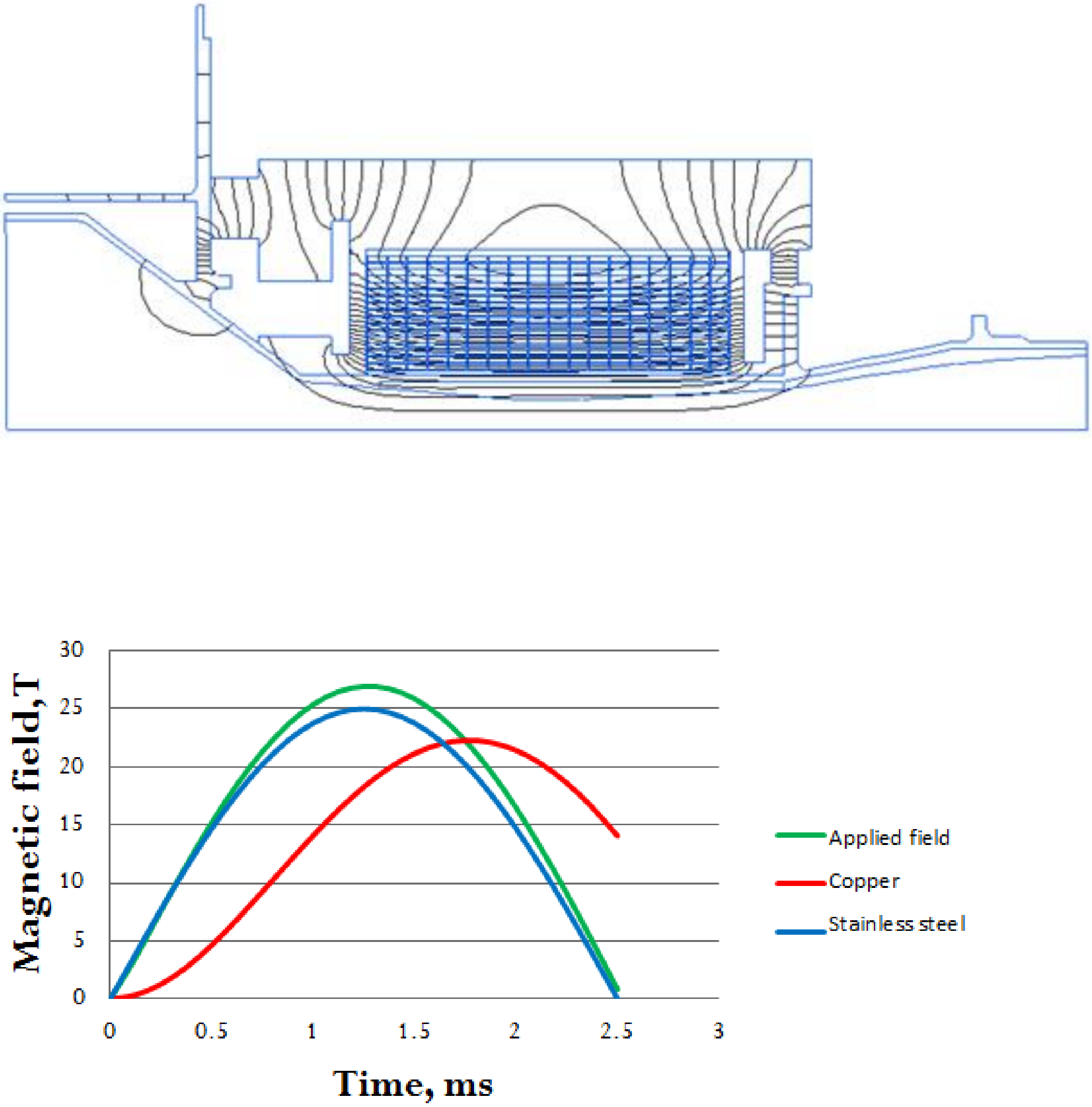

Figure 1.21 The simulated field distribution of the magnetic field inside the resonator. b) The results of the simulations showing the results of penetration of the magnetic field inside the resonator. Green – applied field to the coils, blue – stainless steel resonator, red – copper resonator.

1.5.11 The experiments on air breakdown

In the course of the experiments, by varying the amplitude of the magnetic field, two points of stable operation were found. One of this operating points corresponds to the designed characteristics of the gun, close to the point 70kV of beam voltage and 15A of beam current. The output power in this regime was in the range between 90kW and 150kW, which corresponded to 9 -15% wall plug efficiency. The other operation point was found at a slightly lower voltages, i.e. at 58kV and 22A. At this operating point the power of the radiation was in excess of 200kW, approximately 210kW. This corresponds to 16.5% efficiency. The maximum efficiency of the device was realized at 57kV and 16A of the current reaching almost 20%. If the loses in the thick Teflon window and ohmic losses are taken into account (15-20% and 10% respectively), the interaction efficiency obtained in the experiment was close to 30%, which is in very good agreement with the calculated value.

The focused THz radiation was used to perform initial tests on the air breakdown. It was shown, that it is possible to create a breakdown event on metallic plane with initiators (sharp metallic needles) located at some distance a few meters from the quasi optical converter. The breakdown was also observed in a chamber filled with argon. Further investigation of the breakdown events, such as structural and temporal evolution is recommended.

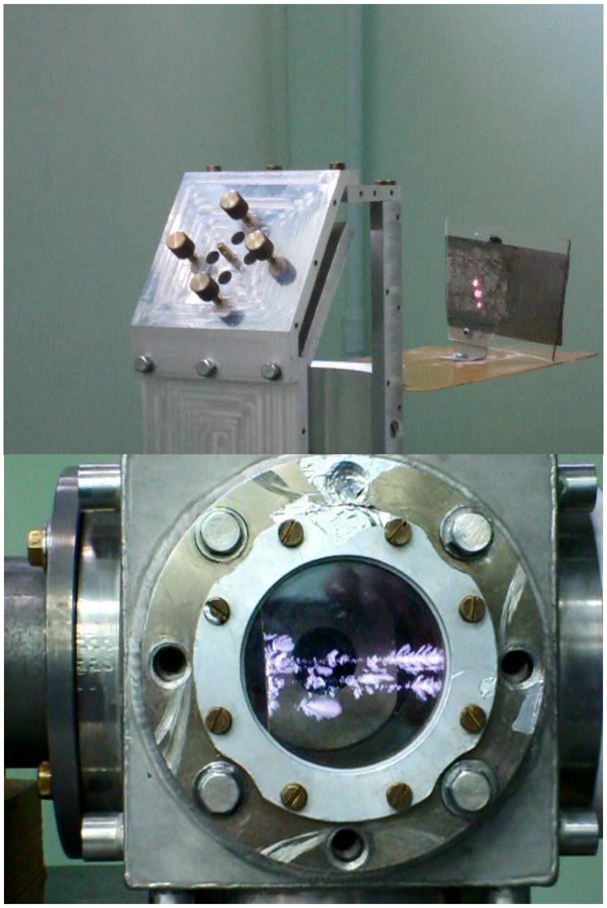

Figure 1.22 The terahertz breakdown observed in the air and in the argon filled chamber.

The amount of the experimental data that was obtained in the course of the experiments was rather limited, since the tube suffered a catastrophic failure, when the output window was pierced during the operation of the device. This lead to the annihilation of the gun and serious damage to the anode of the gyrotron.

The design and manufacturing of the gyrotron windows is a complicated process that is crucial for obtaining high power RF radiation output. The state of the art windows for megawatt class devices [1.37] use a number of materials that have suitable dielectric (loss factor and permittivity) and mechanical properties. Sapphire, water free fused silica, silicon nitride and CVD (chemical vapor deposition) diamond are among the most used. The window is designed in such a way, that the power reflection from it is minimized, i.e. the thickness of the window is an integer number of wavelength. The fact that the exact modal composition of the sub-millimeter gyrotron output radiation is not known, have facilitated the need for a broadband window for this device. The designed window, a Teflon disk of 1.5 mm thickness had acceptable dielectric properties, but the mechanical properties have proven to be unsatisfactory. For the subsequent versions of this modular gyrotron it is crucial to have a window capable of withstanding mechanical stresses due to rep rate regime of operation, by either manufacturing a CVD diamond or sapphire window and in addition, designing the output section of the tube in such a way, that it reduces the amount of pressure that is applied on the edges of the window by the stainless steel spacers that locks the window in its position.

Overall, the studies have revealed several flaws in the gyrotron gun design that should be addressed in the subsequent experiments:

- a more robust and transparent for the terahertz radiation output window;
- additional pumping ports to improve the vacuum conditions inside the tube
- a more robust design of the gun cathode, in particular addressing the issue of the stability of the emitter ring mounts.

The most important factor that had an effect on the tube performance is connected with a novel design of the tube. The fact that the gyrotron has a demountable resonator and collector has a number of advantages at the testing stage, when frequent access to the gun, emitter and other inner parts of the system are needed, for instance to service the emitter ring, adjust orbital to axial velocity ratio of the electron beam or modify the interaction circuit. However, we suspect that this design leads to significant deterioration of the device efficiency since it was observed that the sharp joints between the anode body and the resonator as well as the joints between the resonator and the collector are sources of ions that deteriorate the surface quality of the resonator and are the sources of ions that can halt the generation of the terahertz radiation and can poison the emitter by back traveling to the emitter surface in the magnetic field. The last chapter of my dissertation addresses the issue of how such sharp “protrusions” can deteriorate the performance of high power microwave structures.

Despite the described issues, this tube has shown good performance producing high power teharhertz radiation (up to 210kW) with high efficiency (in excess of 20%) sufficient to initiate the breakdown of air, thus proving the capability of this tube to be used as the core of the concealed radioactive materials detection scheme.

The next chapter of my dissertation describes several effects that deals with the propagation of the electromagnetic radiation from the gyrotron and the ways to improve the range of the detection scheme.

Chapter 2: Analysis of breakdown prone volume and effects of the atmosphere on operation of THz remote system

2.1 Introduction

The developed 670GHz gyrotron produces power which can be well focused and yields power density exceeding the breakdown threshold, an accurate evaluation of the breakdown-prone volume is important for determining the range of the system designed for the detection of the concealed radioactive material. This evaluation for the case of a single wave beam was done in Ref. 2.1. As known (see, e.g., [2.2] and references therein), for a number of reasons it is more advantageous to realize a freely localized breakdown in air by using crossing wave beams. The breakdown-prone volume for the case of crossing wave beams was analyzed in Ref. 2.3. For careful determination of the conditions under which the breakdown occurs, the calculation of such volume should be described in more detail. The results of this analysis were published in the Journal of Applied Physics [2.3].

In this chapter the characterization of the breakdown-prone volume in possible configurations of focused wave beams is presented. The chapter is organized as follows: firstly, a single wave beam is considered, in the next sections the analysis for the case of crossing wave beams is presented. Two possible polarizations illustrated by Fig. 2.1 are distinguished: the wave electric field oriented perpendicular to the plane of crossing (so-called s-polarization) shown in Fig. 2.1a and in the plane of crossing (p-polarization) shown in Fig. 2.1b. First, the case of crossing wave beams in the limit that the region of short wave-beam intersection is analyzed (its length is much shorter than the Rayleigh length) and therefore the effect of diffraction spreading can be neglected. Later, the effect of the diffraction spreading is taken into account and this effect on the breakdown-prone volume is evaluated. After that, the range of the detection scheme is estimated based on the 670GHz gyrotron with power output in excess of 200kW and with pulses length from 10 to 30 microseconds. In the last section analysis of the role of atmospheric effects in widening of wave beams is performed.

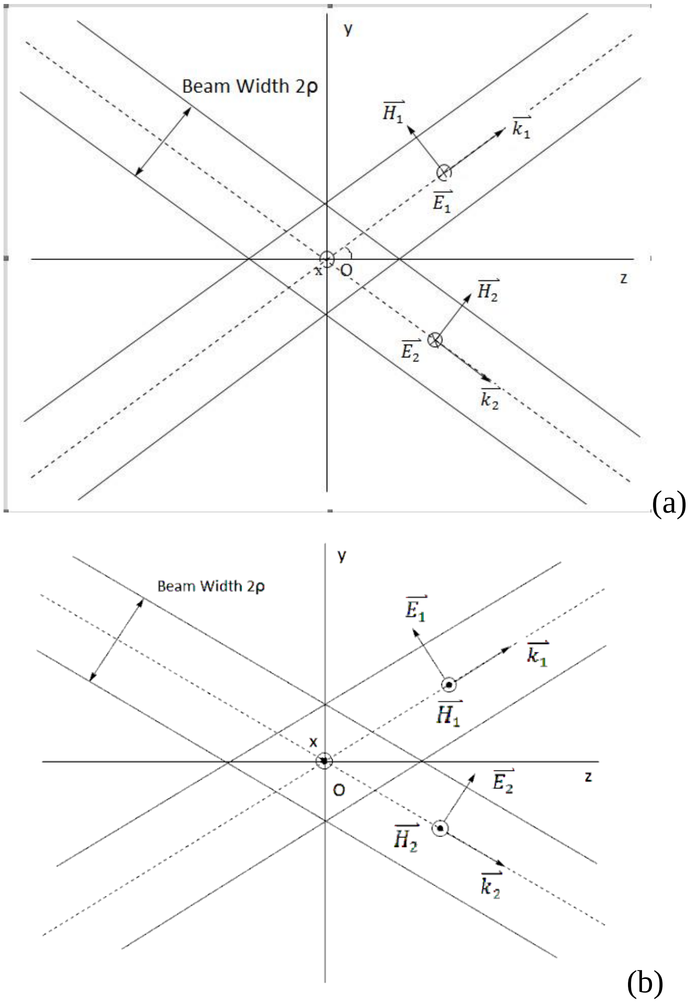

Figure 2.1 Two types of polarization of the crossing wave beams: (a) s-polarization (wave electric field is perpendicular to the plane of crossing, (b) p-polarization (wave electric field is in the plane of crossing)

2.2 Breakdown-prone volume in a single wave beam

In order to characterize a breakdown-prone volume in a single wave beam diffraction should be taken into account under the assumption that this wave beam was focused by a focusing mirror. Then, the intensity of a focused wave beam in the vicinity of its focal plane can be given as [2.4]:

$$\left|E\left(r,z\right)\right|^2 = E_0^2\left[\frac{\rho_0}{\rho\left(z\right)}\right]^2 \exp\left\{-2\frac{r^2}{\rho(z)^2}\right\}. \tag{2.1}$$

In (2.1), $\rho\left(z\right)$ is the axially dependent width of a wave beam defined by:

$$\rho^2\left(z\right) = \rho_0^2\left[1+\left(\frac{\lambda z}{\pi\rho_0^2}\right)^2\right] = \rho_0^2\left(1+\frac{z^2}{z_0^2}\right) \tag{2.2}$$

where ρ_0 is the width of a wave beam in a focal plane, $z=0$, and $z_0 = \pi\rho_0^2/\lambda$ is the Rayleigh length. The region where $E \geq E_{th}$ exists in the vicinity of the axis of the wave beam, at $0 \leq r \leq r_{th}$. Here the limiting value of the radius $r = r_{th}$ corresponds to the radius where power density is equal to its breakdown threshold. Introducing the ratio $\hat{P} = E_0^2 / E_{th}^2$ this condition can be written as:

$$\hat{P}\left(r_{th}, z\right) = \hat{P}_{\max}\frac{1}{1+\left(z/z_0\right)^2}\exp\left\{-2\frac{r_{th}^2}{\rho_0^2\left[1+\left(z/z_0\right)^2\right]}\right\} = 1. \tag{2.3}$$

The radial coordinate limiting the volume where the wave amplitude exceeds the threshold is defined by the condition $\left|E\right|^2 = E_{th}^2$. The normalized variables are defined as follows $R = 2r^2/\rho_0^2$ and $Z = 1 + z^2/z_0^2$, the the Eq. (2.3) can be written as:

$$\frac{\hat{P}}{Z}\exp\left\{-\frac{R_{th}}{Z}\right\} = 1. \tag{2.4}$$

Equation (2.4) allows the determination of the normalized radial coordinate limiting the volume of interest by:

$$R_{th} = Z \ln\left(\hat{P} / Z\right). \tag{2.5}$$

As follows from (2.5), the maximum length of this volume is $Z_{\max} = \hat{P}$ (the total length of the breakdown-prone volume is twice this length). From (2.5) it also follows that, when $\hat{P} = E_0^2 / E_{th}^2 < e$, the curve $R_{th}(Z)$ has only one extremum at $Z = 1 + z^2 / z_0^2$=1, i.e. in the focal plane. Correspondingly, the breakdown volume has a shape of a cigar or a prolate ellipsoid. However, when the excess of the wave amplitude over above the threshold is greater, $\hat{P} = E_0^2 / E_{th}^2 > e$ there is one more extremum at $Z_{extr} = 1 + z^2 / z_0^2 = \hat{P} / e$, i.e. the shape of this volume is a dumb-bell or peanut-like. These profiles are shown in 2.2 for several values of $\hat{P}$. (Note that Z=1 corresponds to z=0 and both new variables, R and Z, are proportional to r^2 and z^2, respectively.)

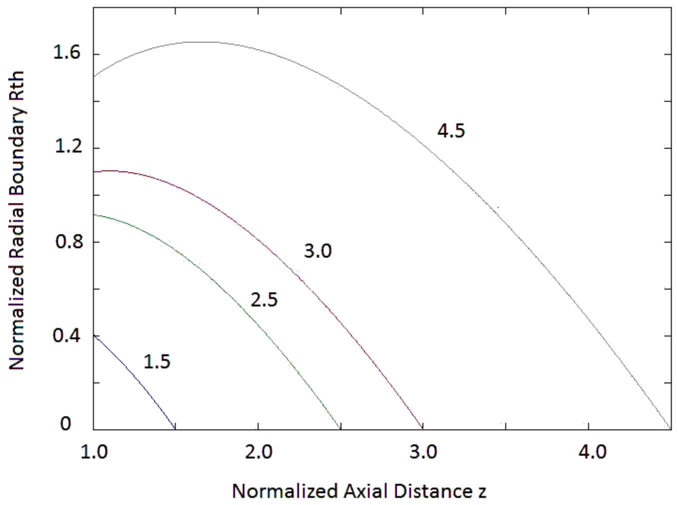

Figure 2.2 Profiles of the breakdown-prone for several values of the ratio of the wave power density to the breakdown threshold.

After expressing the values in the original coordinates, the normalized axial distance correspond to $z_{\max} = z_0\sqrt{\hat{P}-1}$. Correspondingly, (2.5) yields the following formula for the radial coordinate of the boundary of the breakdown-prone volume:

$$r_{th}\left(z\right) = \rho_0\sqrt{1+\left(\frac{z}{z_0}\right)^2}\ \ln\left\{\sqrt{\frac{\hat{P}_{\max}}{1+z^2/z_0^2}}\right\}. \tag{2.6}$$

The cross-sectional area of this volume depends on the axial coordinate and is equal to:

$$S\left(z\right) = \pi r_{th}^2\left(z\right) = \pi\rho_0^2\left(1+\frac{z^2}{z_0^2}\right)\ln\left(\sqrt{\frac{\hat{P}}{1+z^2/z_0^2}}\right) = \pi\rho_0^2 Z\ln\left(\sqrt{\hat{P}/Z}\right). \tag{2.7}$$

From Ref. 2.12 it follows that the corresponding volume is equal to [2.3]

$$V = \frac{\pi^2}{3}\frac{\rho_0^4}{\lambda}\left\{\frac{2}{3}\left(5+\hat{P}\right)\sqrt{\hat{P}-1} - 4\arctan\left(\sqrt{\hat{P}-1}\right)\right\}. \tag{2.8}$$

If this volume is approximated by a prolate spheroid the following estimate [2.2] results:

$$V_{ps} = \frac{2\pi^2}{3}\frac{\rho_0^4}{\lambda}\sqrt{\hat{P}-1}\ln\hat{P}, \tag{2.9}$$

and approximating this volume as a cylinder:

$$V_{cyl} = \frac{\pi^2}{2}\frac{\rho_0^4}{\lambda}\sqrt{\hat{P}-1}\left(\ln\hat{P}\right)^2. \tag{2.10}$$

All these three functions normalized to $\left(\pi^2/3\right)\left(\rho_0^4/\lambda\right)$ are shown in Fig. 2.3 (the first two were compared in Ref. 2.3). It can be seen that when the power density is close to the breakdown threshold, the prolate spheroid approximation shown by the green line is closer to the more accurate result shown by the blue line, while at larger excess of the power density over the threshold, the cylindrical approximation shown by the red line is better.

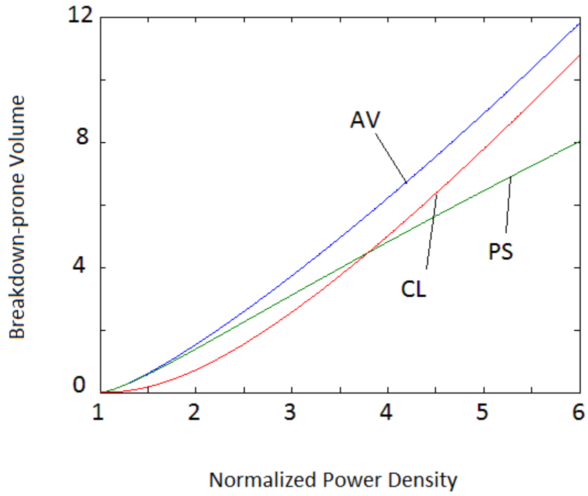

Figure 2.3 The functions characterizing the breakdown-prone volume versus the ratio of the wave power density to its breakdown threshold. The blue, red and green lines show results of the accurate calculations (AV) and the cylindrical (CL) and prolate spheroid (PS) approximations, respectively.

2.3 Breakdown in crossing wave beams with small diffraction spreading

When the diffraction spreading is added the analysis becomes more complicated. Under the assumption that the length of the region of beam intersection is shorter than the Rayleigh length $z_0 = \pi\rho_0^2 / \lambda$, viz. $z^2 << z_0^2$ and, therefore, in (2.2)-(2.3) $Z = 1 + \frac{z^2}{z_0^2} \approx 1$. In other words it is assumed that in the region of beam intersection the diffractive spreading is negligibly small. This assumption allows us to represent the electric field of each wave as $\vec{E} = \vec{E}_0 e^{-ikz} \exp\left(-r^2 / \rho_0^2\right)$. In order to define the field in the region of beam intersection two polarizations of the waves should be distinguished.

2.3.1 Wave electric field perpendicular to the plane of beam crossing (s -polarization).

In this case both wave beams propagate in the y-z plane and the electric fields of both waves are given as $\vec{E}_{01} = \vec{E}_{02} = E_0 \vec{x}_0$. The coordinates in the reference frame of each wave beam are related to coordinates y, z in the lab frame as $y_1 = y\cos\alpha - z\sin\alpha$, $y_2 = y\cos\alpha + z\sin\alpha$, $z_1 = z\cos\alpha + y\sin\alpha$, $z_2 = z\cos\alpha - y\sin\alpha$. Here 2α is the angle between these crossing wave beams. Correspondingly, the intensity of the resulting electric field $\vec{E}_\Sigma = \vec{E}_1 + \vec{E}_2$ is equal to:

$$\left|\vec{E}_\Sigma\right|^2 = 2E_0^2 \exp\left(-2r^2/\rho_0^2\right)\left[\cosh\left(2\frac{yz}{\rho_0^2}\sin 2\alpha\right) + \cos\left(2ky\sin\alpha\right)\right]. \quad (2.11)$$

In (2.11), $r^2 = x^2 + y^2\cos^2\alpha + z^2\sin^2\alpha$ is introduced. In the breakdown-prone volume the intensity (2.11) exceeds the threshold intensity E_{th}^2 defined elsewhere [2.3-2.5]. In the center of the focal plane, where $x = y = z = 0$, the field intensity is maximum: $\left|\vec{E}_\Sigma\right|^2 = E_{\max}^2 = 4E_0^2$. The intensity of the original single wave beam is equal to $E_{or}^2 = 2E_0^2$. So, the splitting of one original wave beam generated by a gyrotron into two beams of equal power allows the doubling of the wave peak intensity due to the interference of the wave beams.

The maximum size of the breakdown-prone volume in x-direction, which stretches from $-x_{\max}$ to $+x_{\max}$, for the wave of a given polarization is located on the x-axis in the focal plane $z = 0$, where also $y = 0$. As follows from (2.11), this size is equal to:

$$x_{\max} = \rho_0 \sqrt{\ln\left(\hat{P}\right)/2}\,. \tag{2.12}$$

In (2.12) the ratio of the peak wave intensity to the breakdown threshold intensity $\hat{P} = 4E_0^2 / E_{th}^2 = 2E_{or}^2 / E_{th}^2$ is introduced. Correspondingly, the breakdown-prone volume is determined by the condition which follows from (2.11):

$$\exp\left(2r^2 / \rho_0^2\right)\left[\cosh\left(2\frac{yz}{\rho_0^2}\sin 2\alpha\right) + \cos\left(2ky\sin\alpha\right)\right]^{-1} \le \hat{P}/2\,. \tag{2.13}$$

The interference of crossing wave beams may cause the appearance of several peaks in the field intensity. For illustration, the y-dependence of the intensity (2.11) in the focal plane ($z=0$) is shown for $x=0$ in Fig. 2.4, and the field intensity is normalized to $4E_0^2$. To accurately interpret results shown in Fig. 2.4 it should be remembered that the power ratio $\hat{P}$ should vary from 1 to 2: at smaller ratios the breakdown is impossible, while in the case of larger ratios, in the framework of the present approximation (neglect of diffraction effects), the breakdown may occur outside of the region of wave beam crossing. Then, in accordance with (2.13) (where the left hand-side is the inverse of the intensity shown in Fig. 2.4), it can be found from Fig. 2.4 that, when the angle exceeds 30°, the breakdown may occur not only in the central peak, but also in two side peaks. In the case of a 60° angle shown in Fig. 2.4d, it may occur even in 5 peaks.

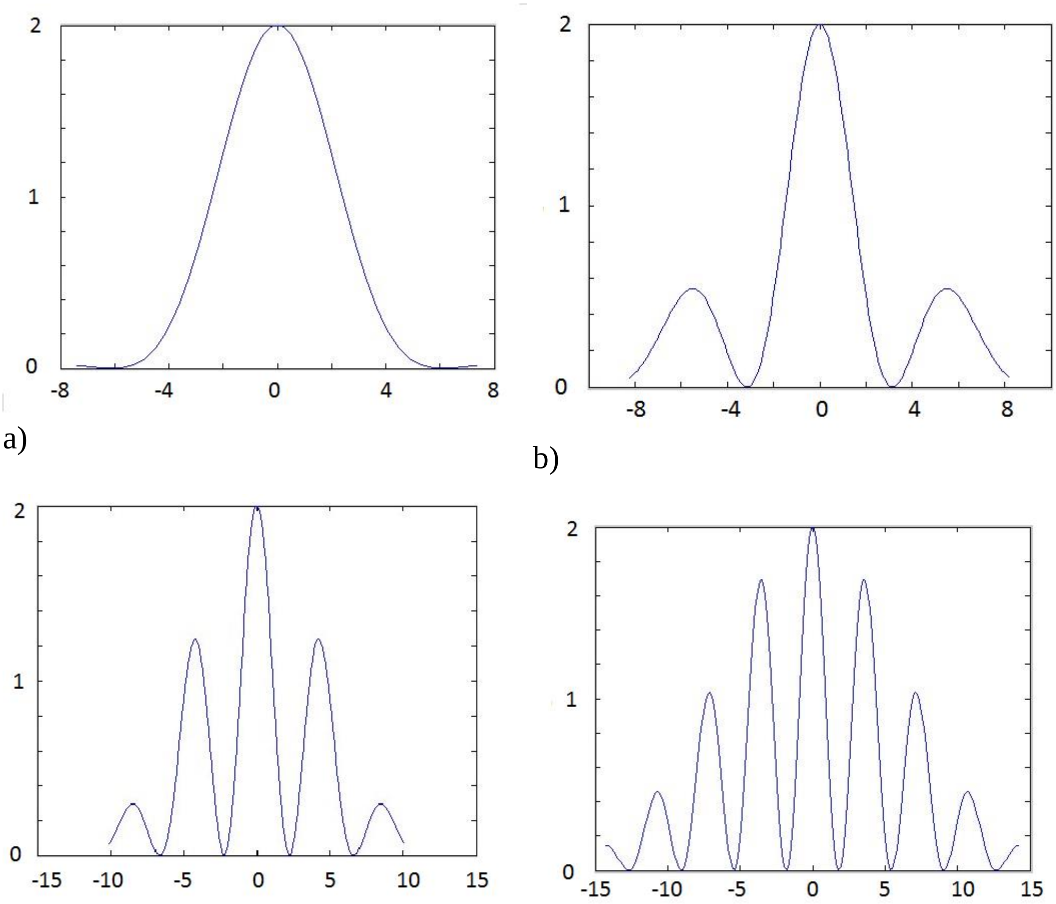

a) b) c) d)

Figure 2.4 Transverse profiles of the wave intensity in crossing wave beams in the focal plane for crossing angles: (a) 15°, (b) 30°, (c) 45° and (d) 60°.

An example of the corresponding 2D profile of this wave intensity in y-z plane is shown in Fig. 2.5 for the case of the 45° crossing angle.

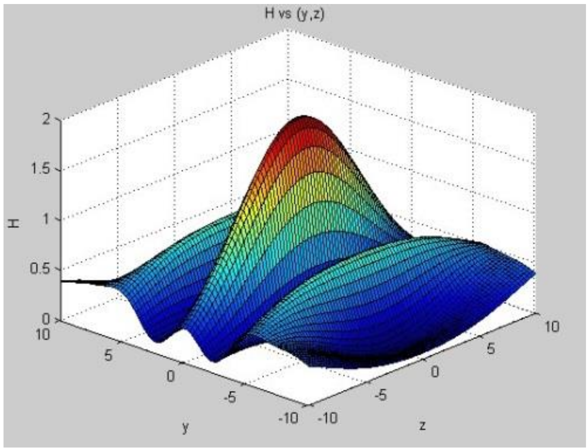

Figure 2.5 A spatial distribution of the wave intensity in the y-z plane in the case of 45^o crossing angle.

The length of the breakdown-prone volume in the z-direction ($-z_{\max} \le z \le z_{\max}$) can be found from (2.13) assuming $x = y = 0$; that yields

$$z_{\max} = \frac{\rho_0}{|\sin\alpha|}\sqrt{\ln\left(\hat{P}\right)/2}\,. \tag{2.14}$$

The formulas given above allow us to calculate the breakdown-prone volume

$$V = 8\int_0^{z_{\max}}\int_0^{y_{\max}(z)}\int_0^{x_{\max}(y,z)} dx\,dy\,dz = 8\int_0^{z_{\max}}\int_0^{y_{\max}(z)} x_{\max}\left(y,z\right)dy\,dz\,. \tag{2.15}$$

Here $x_{\max}(y,z)$ can be found from (2.13) with the use of the definition of r^2:

$$\begin{aligned} x_{\max}^2(y,z) = \frac{\rho_0^2}{2}\ln\left\{\frac{\hat{P}}{2}\left[ch\left(\frac{2yz}{\rho_0^2}\sin 2\alpha\right) + \cos\left(2ky\sin\alpha\right)\right]\right\} - \\ y^2\cos^2\alpha - z^2\sin^2\alpha \end{aligned} \tag{2.16}$$

Then, normalizing all dimensions to the width of the wave beams can be rewritten from (2.15) with the use of (2.16) as:

$$V = 8\rho_0^3\int_0^{z'_{\max}}\int_0^{y'_{\max}(z)}\left(\begin{aligned} \frac{1}{2}\ln\left[\frac{\hat{P}}{2}\left[ch\left(2y'z'\sin 2\alpha\right) + \cos\left(2\hat{k}y'\sin\alpha\right)\right]\right] - \\ y'^2\cos^2\alpha - z'^2\sin^2\alpha \end{aligned}\right)^{1/2} dy'\,dz'\ . \tag{2.17}$$

In (2.17), primes denote normalization to ρ_0, also $\hat{k} = k\rho_0$; the upper limit for the axial coordinate is given by (2.14), and the upper limit for the y-coordinate are determined. These limits can be found by using (2.13) and the fact that maximum values of the y-coordinate are located in the plane $x = 0$. Thus, $y'_{\max}\left(z'\right)$ obeys the equation:

$$y'^2_{\max}\cos^2\alpha + z'^2\sin^2\alpha - \frac{1}{2}\ln\left[ch\left(2y'_{\max}z'\sin 2\alpha\right)+\cos\left(2\hat{k}y'_{\max}\sin\alpha\right)\right] = \ln\left(\sqrt{\hat{P}/2}\right). \tag{2.18}$$

The breakdown-prone volume normalized to $8\rho_0^3$ [cf. Eq. (2.17)] is shown as a function of the normalized power $\hat{P}$ in Figure 6 for several values of the crossing angle. Note that when crossing angles vary from 30^o to 45^o the volume (for a given power-to-threshold ratio) changes only slightly.

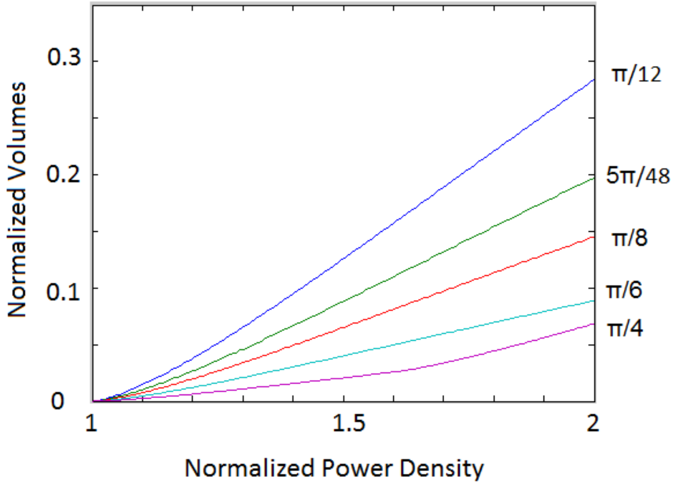

Figure 2.6 Normalized volumes of the breakdown region as functions of $\hat{P}$ for several crossing angles: α=π/12 (dark blue), α=5π/48 (green), α=π/8 (red), α=π/6 (light blue), and α=π/4 (purple).

Figure 2.7 illustrates the effect of contributions from additional side peaks to the volume. When the wave power is large enough for creating the breakdown conditions in the side peaks, the breakdown-prone volume starts to grow faster.

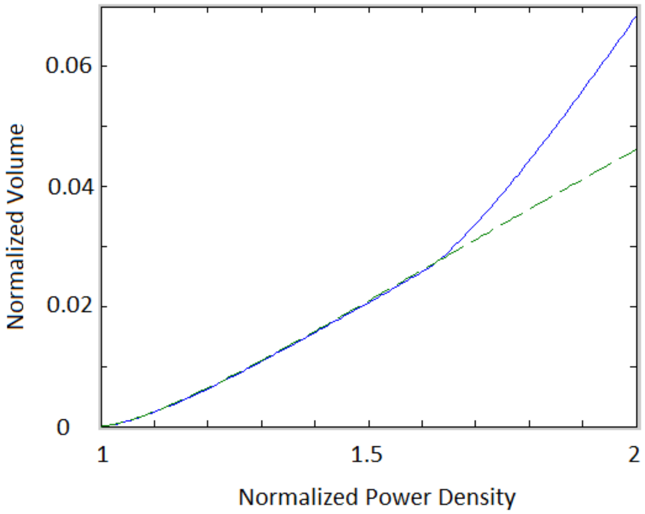

Figure 2. 7 The normalized volume as a function of the normalized power for the crossing angle π/4: the dashed lines show the volume contained in the main peak, the solid lines show the volume calculated accounting for the side peaks.

2.3.2 Wave electric field is parallel to the plane of beam crossing (p -polarization).

Repeating the same steps in derivation as those described above results in the expression for the intensity similar to (2.11):

$$\left|\vec{E}_\Sigma\right|^2 = 2E_0^2 \exp\left(-2r^2/\rho_0^2\right)\left[ch\left(2\frac{yz}{\rho_0^2}\sin 2\alpha\right) + \cos 2\alpha \cdot \cos\left(2ky\sin\alpha\right)\right]. \tag{2.19}$$

As follows from the second term in the square brackets of (2.19), the field intensity in this case is lower than in the case of the first polarization. This second term completely vanishes in the case of perpendicular propagation of crossing beams (when $2\alpha = \pi/2$).

So, Equations (2.12), (2.18) and (2.14) should be replaced, respectively, by

$$x_{\max} = \rho_0\sqrt{\ln\left[\hat{P}\left(1+\cos 2\alpha\right)\right]/2} \tag{2.20}$$

$$y_{\max}'^2 \cos^2\alpha + z'^2 \sin^2\alpha - \frac{1}{2}\ln\left[ch\left(2y'z'\sin 2\alpha\right) + \cos 2\alpha \cdot \cos\left(2\hat{k}y_{\max}'\sin\alpha\right)\right] = \ln\left(\sqrt{\hat{P}}\right)$$

(2.21)

and

$$z_{\max} = \frac{\rho_0}{\left|\sin\alpha\right|}\sqrt{\ln\left[\hat{P}\left(1+\cos 2\alpha\right)\right]/2}\,. \tag{2.22}$$

The normalized breakdown-prone volume for the p-polarization is shown in Fig. 2.8.

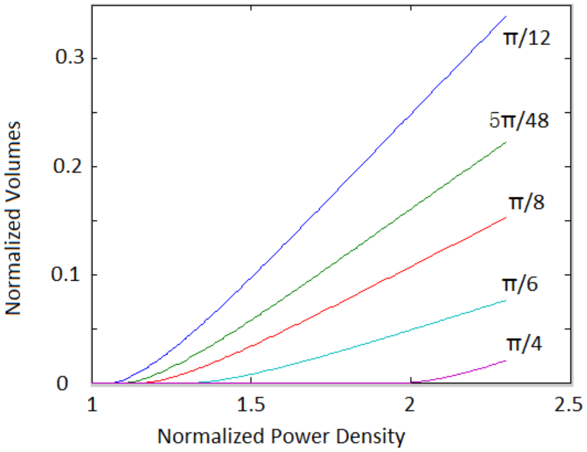

Figure 2.8 Normalized volumes of the breakdown region in the case of p-polarization for different crossing angles: α=π/12 (dark blue), α=5π/48 (green), α=3π/24 (red), α=π/6 (light blue), and α=π/4(purple).

As follows from the comparison of results presented in Fig. 2.8 with those shown in Fig. 2.6 for s-polarization, in the case of s-polarization the breakdown-prone volume is larger.

2.4 Breakdown in crossing wave beams with significant diffraction spreading

Earlier in this chapter, the analysis was performed for the case of crossing wave beams where the axial length of the breakdown-prone volume is much shorter that the Rayleigh length characterizing the diffraction spreading of wave beams: $z_{\max}^2 << z_0^2$.

As follows from the definition of these two distances, their ratio in the case of s - and p - polarizations is equal, respectively, is given by

$$\left(\frac{z_{\max}}{z_0}\right)_s = \frac{\lambda}{\pi\rho_0}\frac{1}{|\sin\alpha|}\sqrt{\ln\left(\sqrt{\hat{P}}\right)}, \tag{2.23a}$$

$$\left(\frac{z_{\max}}{z_0}\right)_p = \frac{\lambda}{\pi\rho_0}\frac{1}{|\sin\alpha|}\sqrt{\ln\left(\sqrt{\hat{P}\left(1+\cos 2\alpha\right)/2}\right)}. \tag{2.23b}$$

As follows from these formulas, the applicability of the assumption used earlier in this chapter is defined by the excess of the power density over its breakdown threshold and the ratio of the width of wave beams to the wavelength. For example, in the case of s-polarization and $\hat{P} = 1.5$, the diffraction spreading can be neglected when the crossing angle obeys the condition $\sin\alpha \geq 0.708\left(\lambda / \rho_0\right)$. The numerical coefficient in this estimate was obtained assuming that the ratio $z_{\max} / z_0$ should be smaller than 1/3.

Keeping the original representation of the intensity of wave beams (2.1)-(2.2) and repeating the same steps in derivation as those described above leads to the formulas defining the breakdown-prone volume which are similar, but more complicated than (2.17). (In view of their complexity, we do not present these formulas here.) Resulting dependences of the normalized volumes of the breakdown-prone region are compared in Fig. 2.9 with the corresponding data shown in Fig. 2.6, which were obtained ignoring the diffraction spread of wave beams, for the case of the s-polarization. As could be expected, the wave beam diffraction spreading reduces the breakdown-prone volume.

From Fig. 2.9 it follows that at small crossing angles, the difference in volumes calculated with and without diffraction spreading effect is rather large; however, at larger angles, that difference becomes relatively small. Therefore, at those larger angles, the breakdown-prone volume can be easily calculated under the assumption of a constant beam width.

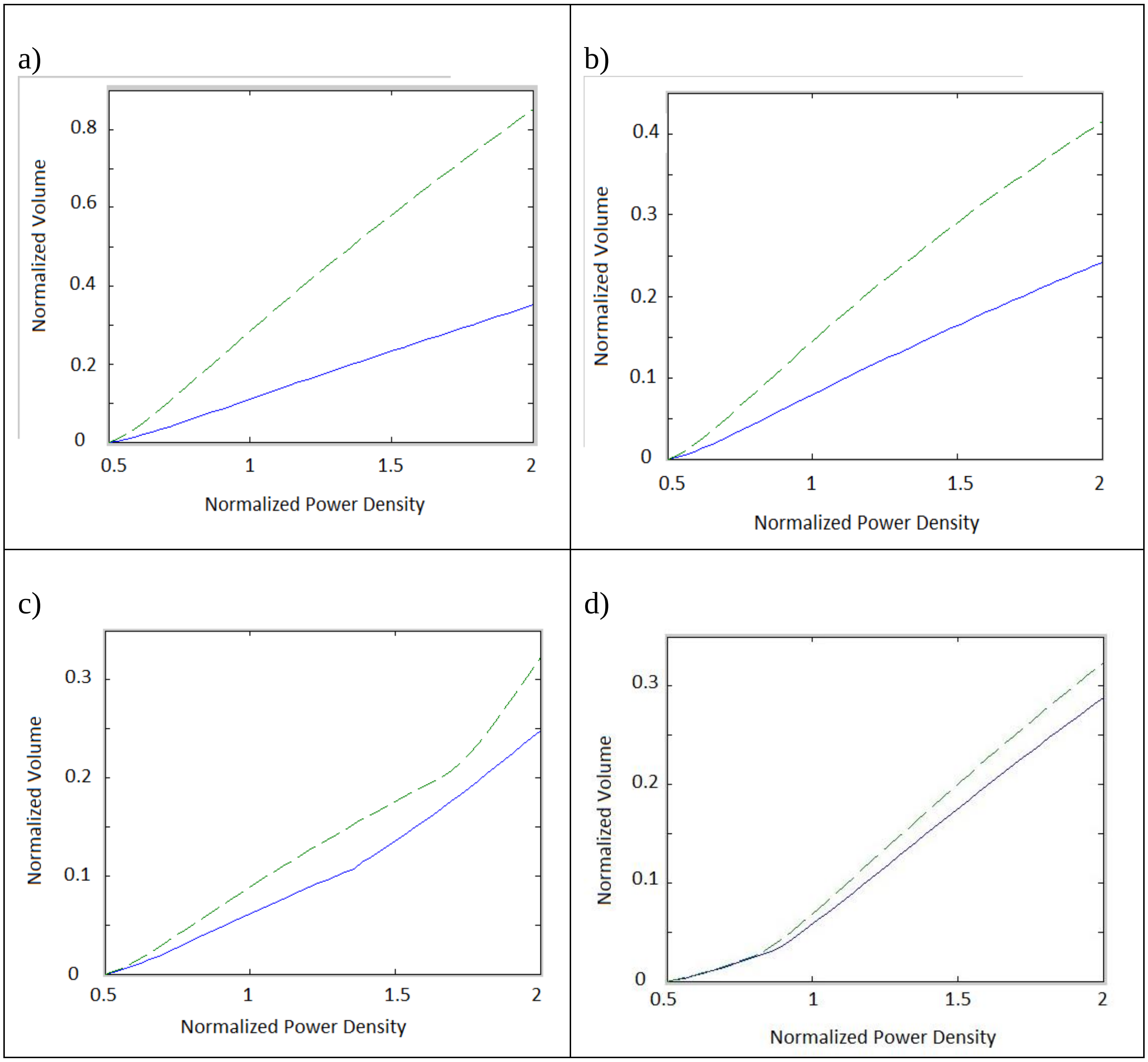

Figure 2.9 Comparison of two types of volumes in the case of s -polarization: solid blue—volume with varied beam width; dashed green—volume with constant beam width a) α=π/12, b) α=π/6, c) α=π/4, d) α=π/3.

It is also important, as will be shown in the next Section, to estimate the cross-sectional area of the focal breakdown-prone volume in the focal plane. Again, normalizing all dimensions to the width of the wave beams, this area can be represented as $S_{\perp} = 4\rho_0^2 S'_{\perp}$. This primed area is shown as a function of the power ratio for several values of the crossing angle in Fig. 2.10 where (a) and (b) show the cases of s - and p - polarizations, respectively. Fig 2.10 (a) and (b) show results of calculations for the case when the beam width is equal to the wavelength, i.e. the normalized wave number is equal to $\hat{k} = k\rho_0 = 2\pi$.

In Figure 2.10(c), results of calculations for a doubled wave number $\hat{k} = 4\pi$ and s - polarization are shown. As follows from the comparison of Fig. 2.10(a) with Fig. 2.10(c), the cross-sectional areas in both cases are quite similar, but in the latter case the area is smaller because the wave power is distributed over a larger space.

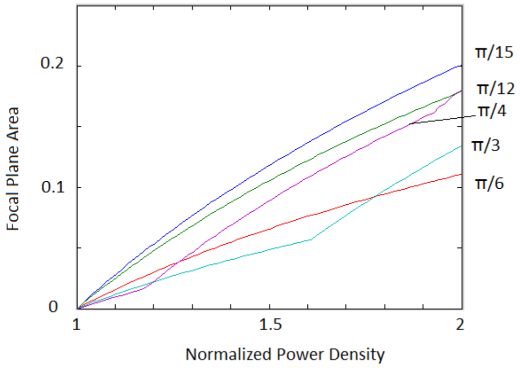

(a) s-*polarization*

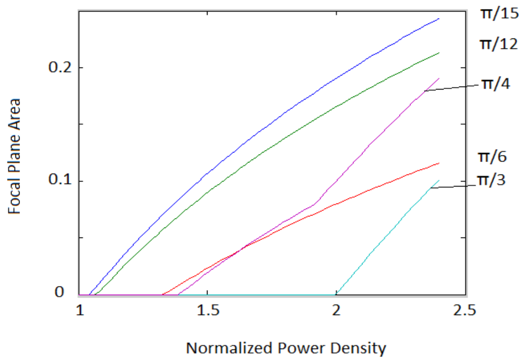

(b) p-*polarization*

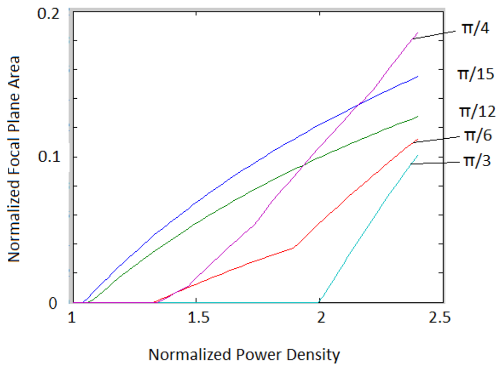

(c)

Figure 2. 10 Cross-sectional area of the breakdown-prone volume in the focal plane.

So, the wave power should exceed the threshold power, equal to $P_{th} = p_{th} S_{\perp}$ where the breakdown threshold power density at the atmospheric pressure is equal to [2.9]:

$$p_{th}\left(MW/cm^2\right) = 1.36\left\{1 + 2.135\left[f\left(THz\right)\right]^2\right\} \tag{2.24}$$

and the cross-sectional area is defined above.

At the same time, the breakdown-prone volume should be small enough in order to have a low breakdown rate in the absence of sources of ionization. This means that in the absence of additional sources of ionization the probability of having any free electrons in the volume defined by Eq. (2.17) should be low.

2.4.1 Role of the width of wave beams

In the analysis performed until now the breakdown-prone volume defined by Eq. (2.17) is normalized to $8\rho_0^3$ and its cross-sectional area in the focal plane normalized to $4\rho_0^2$. These normalization factors strongly depend on the width of the wave beam in the focal plane, ρ_0 . In the absence of wave scattering in the atmosphere, the width of a Gaussian wave beam formed by a simple antenna is equal to

$$\rho_0 = \frac{1}{\sqrt{\pi}} \frac{L}{R} \lambda . \tag{2.25}$$

In (2.25), L and R are the focal length and the antenna radius, respectively. So, when the focal length is much longer than the antenna radius, the width of a wave beam in a focal plane is much larger than the wavelength.

The restrictions on the wave power discussed above, being combined with Eq. (2.25), impose certain limitations on the range-to-antenna radius ratio L/R. First, from the requirement that the wave power should exceed the breakdown threshold and Eq. (2.25) it follows that this ratio is limited by the condition

$$\left(\frac{L}{R}\right)^2 \le \frac{\pi}{4} \frac{P}{p_{th} \lambda^2 S'_\perp} . \tag{2.26}$$

It should be noted that in the case of crossing wave beams the normalized cross-sectional area depends on the power–to-threshold ratio. In the case of a single Gaussian wave beam and the frequency 0.67 THz, Eq. (2.26) is equivalent to:

$$P(MW) > P_{th}(MW) = 0.27\left(L/10R\right)^2 , \tag{2.27}$$

i.e. the available THz power limits the range of the system.

At the same time, however, the breakdown-prone volume should be small enough in order to have a low breakdown rate in the absence of sources of ionization. This condition can be given for the volume defined by Eq. (2.17), i.e. $V = 8\rho_0^3 V'$, as:

$$\left(\frac{L}{R}\right)^3 V'\left\{\hat{P},\alpha\right\} < 0.7\frac{V_{\max}}{\lambda^3}\,. \tag{2.28}$$

For the case of s-polarization, the normalized volume $V'\left\{\hat{P},\alpha\right\}$ is shown in Fig. 2.7. Assuming that the frequency is equal to 0.67 THz and the maximum volume is equal to 1 cm^3, one can get from Eq. (2.28) the following restriction of the range:

$$\left(\frac{L}{R}\right) < \left(\frac{L}{R}\right)_{\max} = \frac{15.6}{\left[V'\left(\hat{P},\alpha\right)\right]^{1/3}}\,. \tag{2.29}$$

Corresponding dependencies are shown in Fig. 2.11 for both s- and p-polarizations. So, for example, in the case of $L/R = 20$ the breakdown-prone volume is small enough in all range of $\hat{P}$'s under study ($1 < \hat{P} < 2$) for any crossing angles shown in Fig. 2.11. At the same time, the power required for initiating the breakdown strongly depends on the L/R ratio. In particular, as follows from Eq. (2.27), for $L/R = 20$ it should exceed the threshold close to 1 MW. The designed 670GHz gyrotron, as shown by the results of the experiments, have power just exceeding 0.2 MW, so this device can be used only for experiments with $L/R \leq 10$. In this case, as follows from Fig. 2.11 for both polarizations, the breakdown-prone volume is small enough to detect the difference in the breakdown rate in the presence of an additional ionizing source from that in its absence.

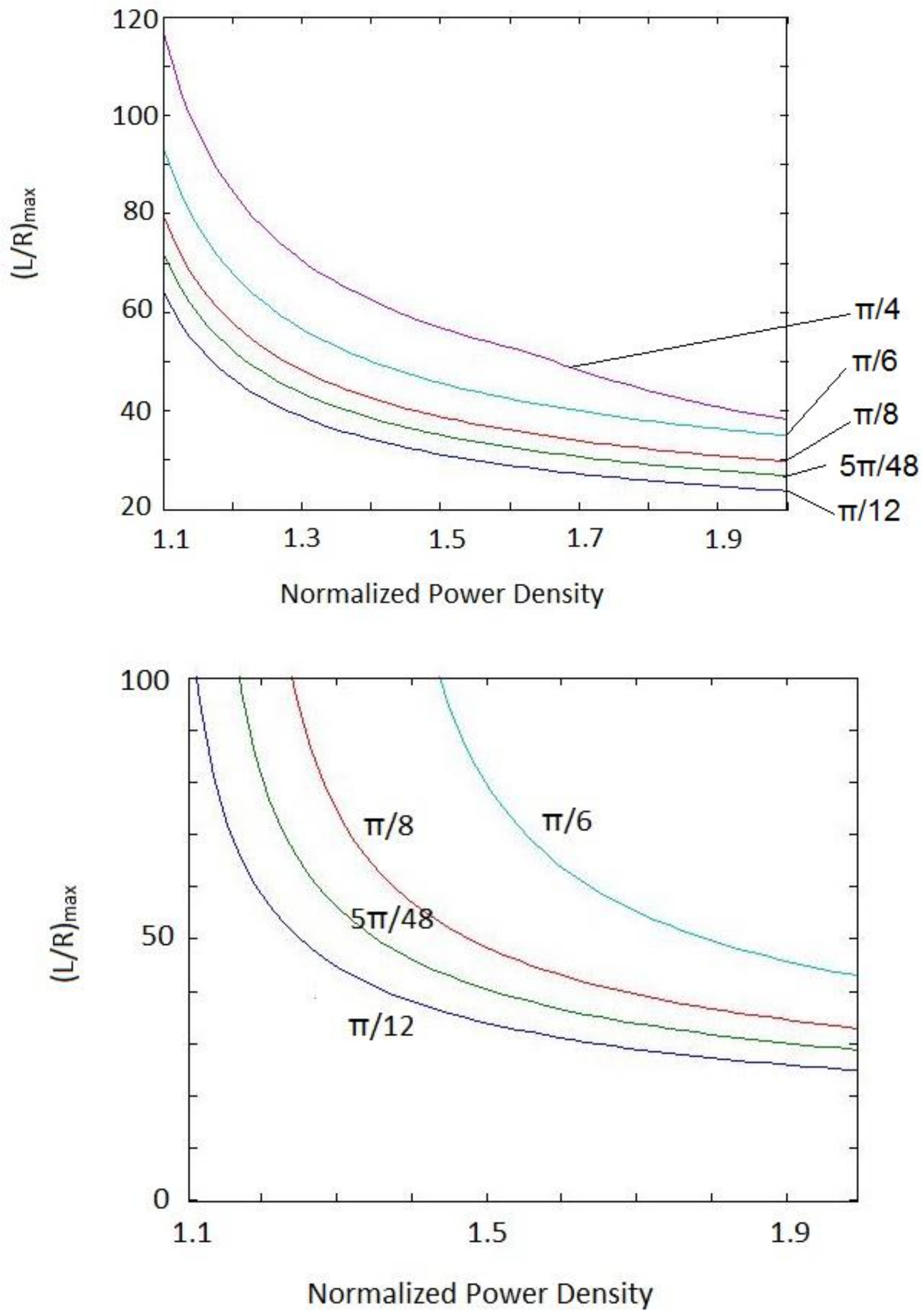

Figure 2. 11 The maximum of the L/R ratio vs normalized power density for different crossing angles; top – s-polarization, bottom – p-polarization.

2.4.2 Effect of the atmospheric turbulence

The analysis carried out above was done accounting for the diffraction effect, but ignoring the role of the atmospheric turbulence on the focusing of such wave beams. The latter effect has been studied in many textbooks (see, e.g., Ref. [2.6] and Ref. [2.7]) and papers (see, e.g., Ref. [2.8] and Ref. [2.9]). Below, we analyze this effect following the approach described in Ref. [2.10]. Before carrying out this analysis, we will make several preliminary remarks.

As is known [2.8], the spoiling of wave beam focusing by atmospheric turbulence can be characterized by using either the Rytov approximation [2.6, 2.7] or the more complicated Markov method. Thus the first step is the evaluation the applicability of the Rytov approximation to the case under investigation. Fante [2.8] has pointed out (with proper references) that the Rytov method is applicable when the parameter

$$\sigma_1^2 = 1.23 k^{7/6} C_n^2 L^{11/6} \tag{2.30}$$

is smaller than 0.3. In (2.30) $k = 2\pi/\lambda$ is the axial wave number and C_n^2 is the strength of turbulent refractive-index irregularities or the refractive-index structure parameter, which characterizes the Kolmogorov power-law spectrum. For microwave frequencies (up to 30 GHz) this constant is in the range (see p. 57 in volume I of Ref. 2.7) from $1.2 \cdot 10^{-14}$ up to $6.6 \cdot 10^{-14}$ ($m^{-2/3}$); here, the lower and upper numbers are given for stable and convective conditions, respectively. (According to Ref. 2.9, this strength for short millimeter waves varies from $6 \cdot 10^{-17}$ for weak turbulence up to $3 \cdot 10^{-13}$ $m^{-2/3}$ for strong turbulence.) At optical frequencies it varies from 10^{-12} to 10^{-14} $m^{-2/3}$ depending on the time of day [2.7]. It is assumed that this parameter is equal to

10^{-13} $m^{-2/3}$, the focusing length is on the order of 100 m and frequency is 670 GHz; then Eq. (2.30) yields $\sigma_1^2 \approx 0.4 \cdot 10^{-4}$. Thus, the Rytov approximation is valid.

The next step is to estimate the importance of the beam wander during the THz pulse duration; this duration in the developed 670 GHz gyrotron varies from 10 to 30 microseconds. A characteristic time scale for wandering of a focal spot can be estimated [2.16] as $t_w \approx D/|v|$. Here D is the wave beam diameter which varies from the diameter of the antenna dish D_A (on the order of 1 m) down to the scale of 1 mm in the vicinity of a focal spot (the radiation wavelength for 670 GHz is 0.47 mm). Also, v is the transverse flow velocity of the particulates in air. In the case of strong wind this velocity can be on the order of 1 m/sec. The characteristic time of wandering of a beam spot in the focal region is on the order of a millisecond and, hence it can be ignored in such short pulses. Correspondingly, in accordance with Ref. 2.8, the case under analysis can be treated as the short-term beam.

After these preliminary considerations the following description of the method that was used for the analysis of the effect of the atmospheric turbulence. According to Refs. [2.10, 2.12], the intensity of the wave in a turbulent atmosphere can be described as:

$$I\left(\vec{r}_\perp, z\right) = \iint\limits_{\infty} \left|\vec{E}_{(0)}\left(\vec{r}'_\perp, z\right)\right|^2 G\left(\left|\vec{r}_\perp - \vec{r}'_\perp\right|, z_{ant}\right) d\vec{r}'_\perp . \tag{2.31}$$

In (2.31), $\left|\vec{E}_{(0)}\left(\vec{r}'_\perp, z\right)\right|^2$ is the wave intensity in the absence of turbulence; for a single wave beam and crossing wave beams with s- and $p-$polarizations, this intensity is determined by (2.1), (2.11) and (2.19), respectively. The function $G\left(\left|\vec{r}_\perp - \vec{r}_\perp{}'\right|, z_{ant}\right)$, under certain assumptions about small perturbations in the refractive index due to the turbulence and smallness of the wavelength with respect to the inner scale of the turbulence, can be approximated by:

$$G\left(\left|r_\perp - r'_\perp\right|, z\right) = \frac{1}{\pi r_b^2}\exp\left(-\left|r_\perp - r'_\perp\right|^2 / r_b^2\right), \tag{2.32}$$

where the parameter r_b characterizes the effect of the turbulence on the width of a wave beam and is defined by the following relation:

$$r_b^2 = 0.434 \cdot C_n^2 \cdot z_{ant}^3 \int_0^\infty \frac{\exp(-\kappa^2 / \nu_m^2)}{(\kappa^2 + \nu_0^2)^{11/6}} \kappa^3 \, d\kappa \,. \tag{2.33}$$

In (2.33), $\nu_0 = 2\pi / L_0$, $\nu_m = 5.92 / l_0$ are the wave numbers determined by the outer L_0 and inner l_0 scales of the turbulence, respectively and the variable $z_{ant} = L - z$ characterizes the distance a wave beam passes from the antenna towards the focal plane located at the distance L from antenna. Since we are interested in characterizing the breakdown-prone volume localized in a small region near the focal plane, below we will assume in (2.33) $z_{ant} \simeq L$.

The representation of the right-hand side of (2.33) as $r_b^2 = 0.434 \cdot C_n^2 \cdot L^3 K$ where K denotes the integral given in (2.33). In Fig. 2.12, the lines of equal values of this integral are shown in the plane of parameters "ν_m versus ν_0". In principle, this integral can be expressed in terms of the incomplete gamma functions, since

$$\int \frac{\exp\left(-x/\nu\right)}{\left(a+x\right)^{11/6}} x dx = \frac{1}{\nu^{5/6}} \left\{ a\Gamma\left(-\frac{5}{6}, \frac{a+x}{\nu}\right) - \nu\Gamma\left(\frac{1}{6}, \frac{a+x}{\nu}\right) \right\}. \tag{2.34}$$

However, this solution is unwieldy to perform useful calculations, albeit one can express the upper gamma function in (2.34) via the lower gamma function and use a plot for that function shown in Fig. 6.3 of Ref. [2.13].

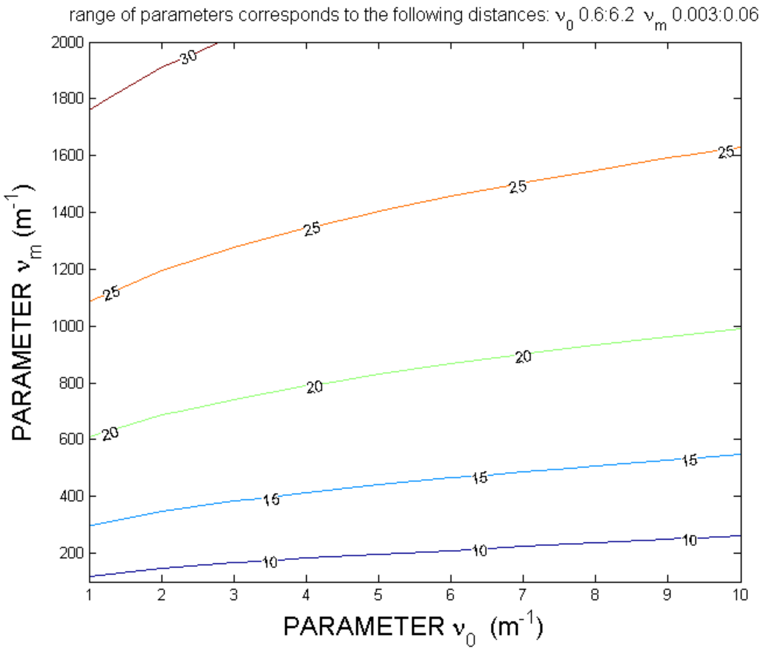

Figure 2. 12 Lines of equal values of the integral K expressed in $m^{-1/3}$.

Substituting Equations (2.11) and (2.32) into (2.31) allows one to calculate this integral analytically yielding the following distribution of the s-polarized wave beam intensity in the turbulent air:

$$I(x,y,z)=2E_0^2\sqrt{a_1a_2}\exp\left[-2\rho_0^{-2}\left(a_1x^2+a_2\cos^2\alpha\cdot y^2+\sin^2\alpha\cdot z^2\right)\right]\times$$

$$\times\left[\exp\left(a_2\rho_0^{-4}r_b^2z^2\sin^2 2\alpha\right)\cdot ch\left(2a_2\rho_0^{-2}yz\sin 2\alpha\right)+\exp\left(-a_2k^2r_b^2\sin^2\alpha\right)\cdot\cos\left(2a_2ky\sin\alpha\right)\right] . \qquad (2.35)$$

In (2.35) the following parameters are defined: $a_1=\left(1+2r_b^2/\rho_0^2\right)^{-1}$, $a_2=\left(1+2\cos^2\alpha\cdot r_b^2/\rho_0^2\right)^{-1}$ (A similar expression can be readily derived for the crossing wave beams of $p-$polarization).

When the crossing angle in (2.35) is equal zero, Eq. (2.35) yields the spatial distribution of the intensity in a single wave beam:

$$I(x,y,z)=4E_0^2a_1\exp\left[-\frac{2a_1}{\rho_0^2}\left(x^2+y^2\right)\right] \tag{2.36}$$

In (2.36), however, the numerical coefficient 4, which followed from the effect of interference of two beams, should be replaced by 2. In the absence of turbulence, i.e. when $r_b \to 0$, $a_1 = a_2 = 1$, that reduces (2.35) to Eq. (2.11).

The profiles of the wave beam intensity in the focal plane (where $z = L$ and, hence, $\rho = \rho_0$) in vacuum and in the turbulent atmosphere are shown in Fig. 2.13 where on the horizontal axis is shown the transverse coordinate normalized to ρ_0. The case of a single beam is shown in Fig. 2.13 (a); the wave intensity is axially symmetric, so on the horizontal axis the normalized radial coordinate. In Fig. 2.13 (b) and (c) the distribution of the wave beam intensity in the focal plane along the $y-$coordinate (when $x = z = 0$) is shown for beams with the crossing angles 12 (b) and 24 (c) degrees. These two last plots are shown for the case when the radial width of wave beams in the focal plane is equal to two wavelengths (i.e. in (2.35) $k\rho_0 = 4\pi$).

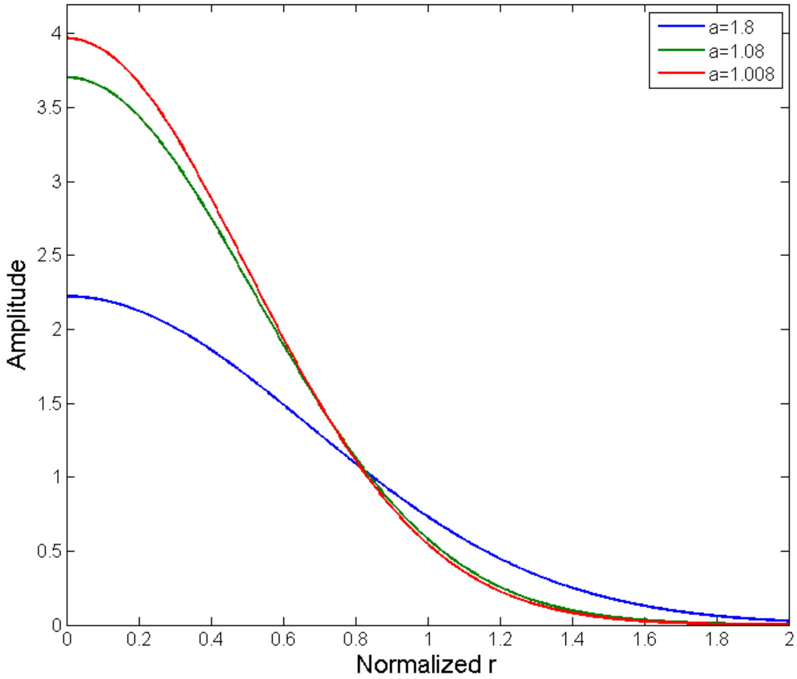

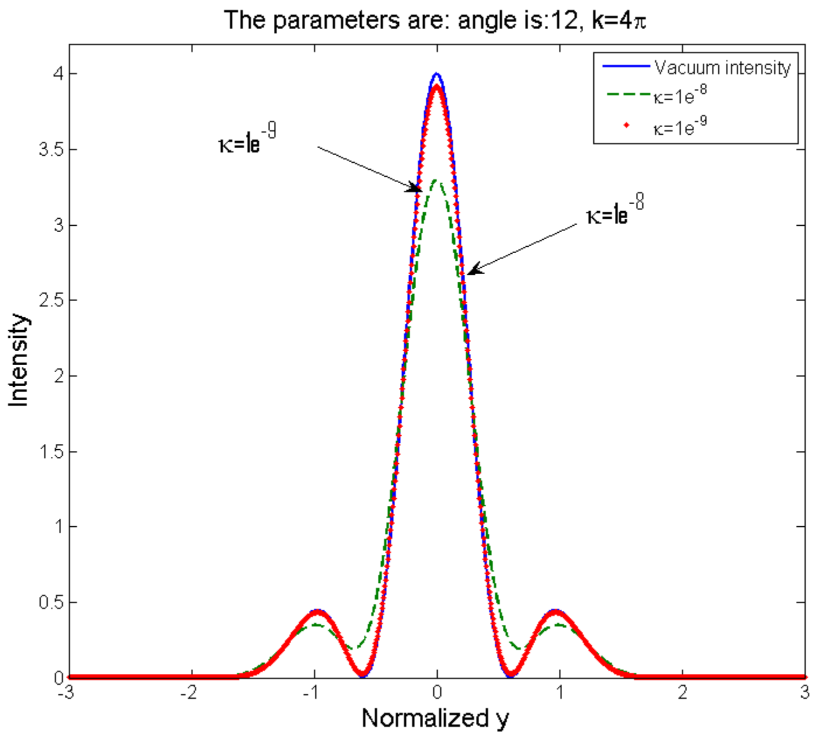
The parameters are: angle is:12, k=4π

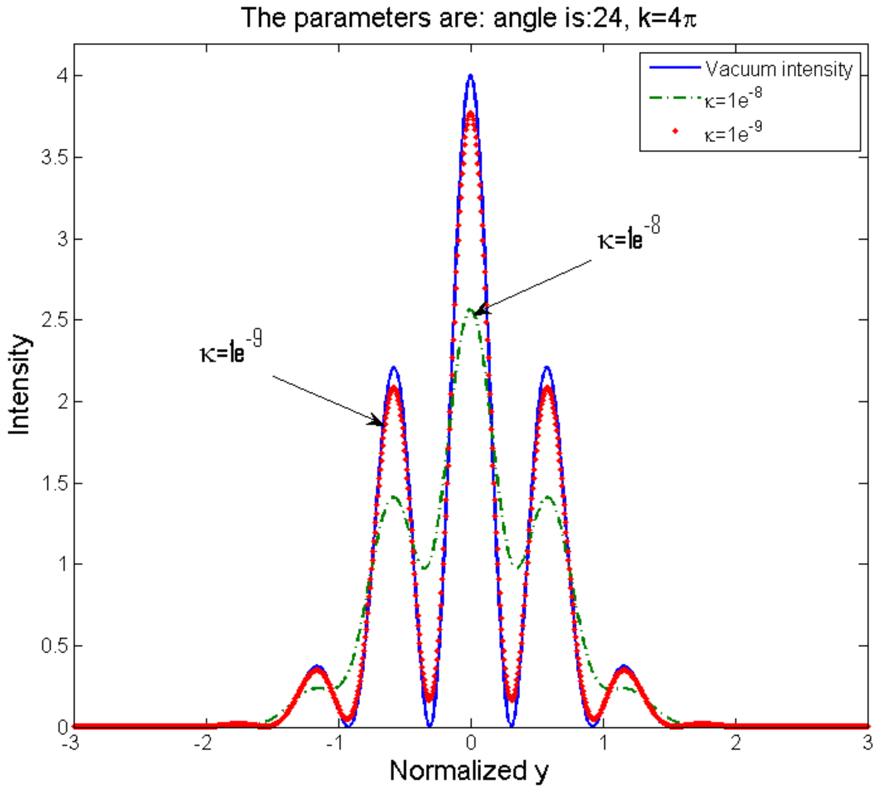

Figure 2. 13 Radial profiles of the wave beam intensity in the focal plane in the absence of atmospheric turbulence (solid blue curve) and in its presence for several values of the turbulence parameter $\hat{K}$ shown in the inset.

For practical purposes, it can be sufficient to evaluate the attenuation of the wave beam intensity in the center of the focal plane, where the intensity is maximum. As follows from equations given above, this attenuation can be characterized in the cae of wave beams of s-polarization by the attenuation factor

$$A = \frac{I(0,0,L)}{\left|\vec{E}_{\Sigma}\right|^2_{\max}} = \frac{1}{2}\sqrt{a_1 a_2}\left\{1+\exp\left\{-a_2\left(2\pi\frac{r_b}{\lambda}\right)^2 \sin^2\alpha\right\}\right\}. \qquad (2.37)$$

As follows from (2.37), in the case of weak turbulence ($r_b^2 << \rho_0^2$) $A \simeq 1$, while in the case of strong turbulence ($r_b^2 >> \rho_0^2$) the attenuation factor is small: $A \propto \rho_0^2 / r_b^2 << 1$. The dependence of A on the r_b / ρ_0 ratio is shown in Fig. 2.14 for several values of the crossing angle. Fig. 2.14 (a) and (b) correspond to different values of the normalized wave number $\hat{k} = k\rho_0 = 2\pi\rho_0 / \lambda$

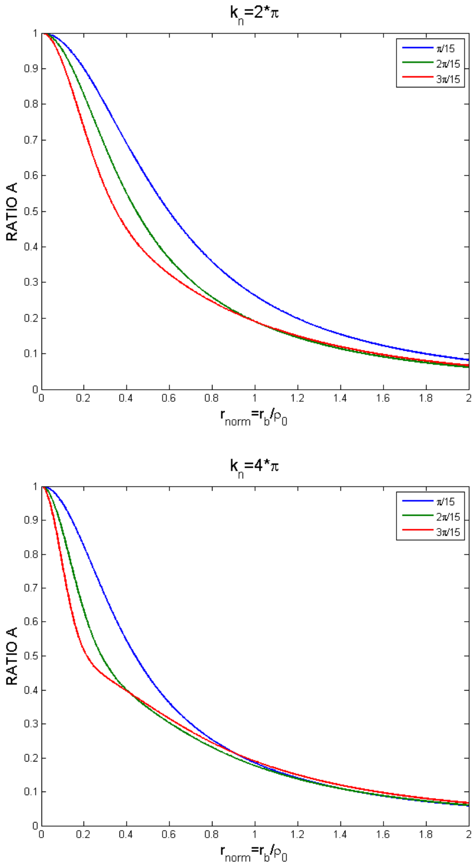

Figure 2. 14 Attenuation factor as the function of the r_b / ρ_0 ratio for the normalized wave number equal to 2π (top) and 2π (bottom).

As follows from Fig. 2.14, in the case of a narrow wave beam (figure) the effect of the atmospheric turbulence is relatively weak when the parameter r_b does not exceed $0.1\rho_0$. As the crossing angle and the beam width increase, this restriction on the effect of the atmospheric turbulence becomes even more stringent.

Under the condition of a weak turbulence effect ($r_b \leq 0.1\rho_0$) for evaluating the corresponding range of the system operation. In line with Eq. (2.33), the corresponding condition can be written as:

$$\left[L(m)\right]^3 < \frac{10^{-2}\left[\rho_0(m)\right]^2}{0.434C_n^2K}, \tag{2.38}$$

where K is given in Fig. 2.12. If we assume that a typical width of a well focused THz wave beams does not exceed 1 mm, the strength of turbulent refractive-index irregularities or the refractive-index structure parameter is on the order of $C_n^2 \approx 10^{-13} m^{-2/3}$ and the value of K is about 10-20, then we can readily find that the effect of the turbulence is weak at distances less than 20-30 meters. Certainly, increasing the turbulence parameter C_n^2 shortens this distance. The calculations done by Granatstein and Nusinovich showed that the range of the detection is close to 100 meters [2.1].

Chapter 3: Single mode excitation in High-Power Gyrotrons

3.1 Background

Megawatt-Class millimeter wave gyrotrons are necessary for electron cyclotron resonance heating and current drive in large-scale plasma installations. 1MW continuous wave power gyrotrons operating at 140GHz and 170GHz are developed for experiments at the stellarator Wendelstein-7X [3.1] and the ITER tokamak [3.2] respectively. To have an acceptable level of ohmic losses for continuous operation these devices should operate at very high order modes with dense spectra of eigenfrequencies. Thus the problem of mode excitation and their interactions become of extreme importance [3.3]; especially it is important at start-up, when voltage rises from zero to its nominal value, which usually in the range of (50-100kV). In the course of the rise relativistic electron cyclotron frequency decreases by about 20%, thus allowing the cyclotron-resonance condition to be fulfilled for a number of modes with frequencies higher than the operating mode prior the excitation of the desired oscillation.

Analysis of gyrotron start-up scenarios is summarized in [3.14]. This analysis shows that in high-power gyrotrons driven by electron beams with diode type magnetron injection guns (MIG) [3.4] at least one parasitic mode is excited prior to the excitation of the desired mode. Depending on the power level of those parasites significant damage can be caused to various diagnostic tools. Excitation of parasitic modes can be avoided in gyrotrons with triode type electron guns, but this makes the high-voltage circuitry more complicated, thus gyrotron users prefer to utilize diode-type guns. One of the methods of avoiding those excitations is fast voltage rise, as analyzed in [3.5], however, its feasibility with the current state of high voltage circuitry is questionable.

Another way to tackle this problem was proposed in [3.14]. The idea of this method is to ensure that the transition from space-charge limited emission to the temperature limited emission to occur at higher voltages. We performed a theoretical analysis of the method and came to several additional conclusions for the device performance. This method is especially advantageous for the gyrotrons intended for suppression of neoclassical tearing modes [3.6]. Typically, those gyrotrons operate in a power modulated regime. This means that operating voltage drops by 20-25%, reducing the gyrotron power to a small fraction of the full output. In this regime the tube collector is overloaded [3.7]. The described method allows one to address the issue of collector loading by simultaneously reducing the beam current, thus avoiding overheating. The equations describing the formalism were derived and simulated, and all the simulations were performed by using the MATLAB computing environment. The results of this work were presented at a number of conferences, (including APS DPP 2009 and ICOPS 2010) and published in IEEE Transactions on Plasma Science [3.1].

3.2 Problem formulation

3.2.1 Current density

Gyrotron electron guns typically operate in the regime of temperature limited emission [3.10]. This is true, however, only for the nominal values of the beam voltage V_{nom}. During the startup, i.e. when the voltage rises to its nominal value, in the range of intermediate voltages $V < V_{nom}$, the electron current density j contains contributions from both space-charge limited and temperature limited emission and can be described by the Longo formula [3.11]

$$\frac{1}{j} = \frac{1}{j_{SC}} + \frac{1}{j_{TL}}. \tag{3.1}$$

In Eq. (3.1) j_{SC} and j_{TL} are the space charge limited and temperature limited contributions, respectively. The space-charge limited current density j_{SC} in the parallel-plane diode is given by the Child-Langmuir law:

$$j_{SC} = \frac{4}{9}\varepsilon_0 (2\eta)^{1/2} \frac{V^{3/2}}{d^2} \tag{3.2}$$

where ε_0 is the dielectric constant of the free space, η is electron charge-to-mass ratio and d is cathode-to-anode spacing. This exact dependence is modified for the case of conical cathodes [3.8], however it retains the same 3/2 dependence of the current density on the voltage.

The Schottky effect enhances the electron emission. The temperature-limited current density j_{TL} taking account of the Schottky effect can be written as:

$$j_{TL} = j_{RD} \exp\left\{ \left(\frac{eE}{4\pi\varepsilon_0} \right)^{1/2} \right\}. \tag{3.3}$$

In Eq. (3.3) the quantity j_{RD} is given by:

$$j_{RD} = A_0 T^2 \exp\left\{ -\frac{e\phi}{kT} \right\} \tag{3.4}$$

is the Richardson-Dushman current density with parameter A_0 given by $A_0 = 1.2 \cdot 10^6 A/m^2 \deg^2$ and ϕ is the work function of the emitter material. For a typical gyrotron electron gun the electric field at the cathode surface does not exceed

5-7 kV/mm. If in the equation (3.3) the applied electric field E is written as $E = V/d$ it makes the exponential term close to unity (even for the electric field equal to 10kV/mm this term is still equal to 1.1274). Therefore the voltage dependence in Eq. (3.3) can be ignored and then $j_{TL} = j_{RD}$. It is possible to find the transition voltage from space charge limited to temperature limited emission, which was denoted V_{tr} in the introduction section by using Eq. (3.2) and Eq. (3.4). It was assumed that this transition takes place when $j_{SC} = j_{RD}$ and this voltage V_{tr} is estimated by means of equations (3.2) and (3.4).

3.2.2 Self-excitation conditions

The self-excitation condition for gyrotron modes defines the start current as [3.12]:

$$I_{0,st} = 1/\chi'' \tag{3.5}$$

where χ'' is the imaginary part of the linear susceptibility of the electron beam with respect to the field of a given mode and $I_{0,st}$ is the starting value of the normalized beam current parameter. In order to simplify the estimates the axial electric field distribution in the resonator is approximated by the Gaussian function $f(z) = \exp\left\{-\left(2z/L\right)^2\right\}$. Also, the device under consideration is assumed to operate at the fundamental cyclotron resonance. Under the abovementioned conditions according to [3.12], the normalized beam current parameter is equal to:

$$I_0 = 0.238 \cdot I_b(A) \cdot Q \cdot 10^{-3} G \frac{\lambda}{L} \frac{1}{4} \frac{1}{\gamma_0 \beta_{\perp_0}^4} \tag{3.6}$$

and the imaginary part of the linear susceptibility can be defined as:

$$\chi'' = -\frac{\pi}{4}\mu^2\left(1+\frac{\partial}{\partial\Delta}\right)\exp\left\{-\frac{\left(\Delta\mu\right)^2}{8}\right\}. \tag{3.7}$$

In Eq. (3.6) $I_b\left(A\right)$ gives the beam current in Amperes, Q is the cavity quality factor, the parameter G describes the coupling of a thin annular electron beam to the $TE_{m,p}$ - mode:

$$G = \frac{J_{m-1}^2\left(\nu_{m,p}R_0 / R_w\right)}{\left(\nu_{m,p}^2 - m^2\right)J_m^2\left(\nu_{m,p}\right)}, \tag{3.8}$$

L/λ is the ratio of the distance characterizing the axial localization of the cavity field to the wavelength, $\gamma_0 = 1+eV/mc^2$ is the initial electron energy normalized to the rest energy, and $\beta_{\perp,z} = v_{\perp,z}/c$ is the ratio of electron velocity components to the speed of light. In Eq. (3.7) $\Delta = \left(2/\beta_{\perp 0}^2\right)\left(1-\Omega_0/\omega\right)$ is the normalized cyclotron resonance detuning between the wave frequency ω and the cyclotron frequency at the entrance of the cavity Ω_0 and $\mu = \left(\pi\beta_{\perp 0}^2/\beta_{z0}\right)\left(L/\lambda\right)$ is the normalized interaction length. Eqation (3.8) gives the coupling coefficient for a circularly polarized mode co-rotating with electrons gyrating in the external magnetic field; the components in the formula have the following meanings $\nu_{m,p}$ is the eigennumber of a mode under consideration (i.e. $TE_{m,p}$) and R_0/R_w is the ratio of the electron guiding center radius to the cavity wall radius. In the case of a counter-rotating mode there should be the $m+1$ index in the subscript.

As follows from Equations (3.5) - (3.7), the start value of the beam current can be written as:

$$I_{b,st}\left(A\right)=21.4\frac{\exp\left\{\dfrac{\left(\Delta\mu\right)^{2}}{8}\right\}}{\mu^{2}\left(\dfrac{\Delta\mu^{2}}{4}-1\right)}\frac{4\gamma_{0}\beta_{\perp_0}^{4}}{Q\cdot10^{-3}G}\frac{\lambda}{L}\,. \qquad (3.9)$$

To determine the dependence of the start current on the beam voltage it should be taken into account, that the normalized cyclotron resonance detuning Δ in Eq. (3.9) depends on the relativistic cyclotron frequency at the entrance of the cavity, $\Omega_0 = eH_0 / mc\gamma_0$; then, the normalized detuning and normalized length, as well as the start current in Amperes as given by Eq. (3.9), depend on the orbital and axial components of initial electron velocity which, in their turn, also depend on voltage.

3.2.3 Dependence of electron velocity on parameters

Using the adiabatic theory of magnetron type electron guns [3.13] the orbital velocity is linearly proportional to the anode voltage, i.e. for a diode-type gun this velocity can be defined as:

$$\beta_{\perp0}=\beta_{\perp0,f}\frac{V}{V_f}, \qquad (3.10)$$

where the subscript ‘f’ stands for the final values of the beam voltage and corresponding orbital velocity. Then, the axial velocity can be defined with the use of the standard relation between the electron velocity components and the electron energy:

$$\beta_{z0}=\left(1-\gamma_0^{-2}-\beta_{\perp0}^{2}\right)^{1/2}. \qquad (3.11)$$

Using the Busch's theorem, the radial coordinate of electron guiding centers R_g and the external magnetic field vary along the device axis $B(z)$ are related as:

$$B(z) R_g^2(z) = const. \tag{3.12}$$

Also the electron orbital momentum $p_\perp$ obeys the magnetic invariant of motion:

$$p_\perp^2 / B = const\,. \tag{3.13}$$

Finally, the initial orbital velocity of electrons emitted with zero initial velocity is determined by the electric field perpendicular to the magnetic force line at the cathode and the external magnetic field [3.13]:

$$v_{\perp,c} = cE_{\perp,c} / H_c\,. \tag{3.14}$$

In Eq. (3.14) the subscript 'c' designates the cathode. The same velocity, as follows from Eq. (3.13), can be defined as:

$$\beta_{\perp,c} = \gamma_0 B_0 / \sqrt{\alpha_B}\,. \tag{3.15}$$

The subscript '0' designates the resonator and $\alpha_B = B_0 / B_c$ is the magnetic compression factor. Combining the equations (3.14)-(3.15) this factor can be determined by the following formula:

$$\alpha_B = \left[\gamma_0 B_0 / E_{\perp,c}\right]^{2/3}. \tag{3.16}$$

This magnetic compression determines, along with Eq. (3.12), the relation between the emitter radius and the beam position in the interaction space.

3.2.4 Collector loading

The power dissipated in the collector can be defined as:

$$P_{coll} = P_{b0} - P_{RF}\,. \tag{3.17}$$

In Eq. (3.17), $P_{b0} = I_b V_b$ is the beam power at the entrance to the interaction space (this power is the product of the beam current by the beam voltage) and P_{RF} is the power of the microwave radiation. The latter is determined by the beam power and the gyrotron RF generation efficiency η:

$$P_{RF} = \eta P_{b0}. \tag{3.18}$$

Then Eq. (3.17) can be rewritten as:

$$P_{coll} = P_{b0}\left(1-\eta\right). \tag{3.19}$$

In the framework of the general theory of gyrotrons [3.7, 3.9], the dependence of the efficiency on the beam voltage follows from the voltage dependence of normalized parameters (cyclotron resonance mismatch, normalized length and normalized beam current parameter) which define the gyrotron orbital efficiency $\eta_\perp$. Introducing the voltage normalized to its final value, $\hat{V} = V / V_f$, one can define the voltage dependence of normalized parameters as follows:

$$\mu\left(\hat{V}\right) = \hat{V}^2 \left(\frac{\beta_{zf}}{\beta_z}\right) \mu_f ,$$

$$\Delta\left(\hat{V}\right) = \frac{1}{\hat{V}^2}\left\{\Delta_f - \left(\frac{2}{\beta_{\perp f}^2} - \Delta_f\right)\frac{\left(\gamma_f - 1\right)}{\gamma_f}\left(1-\hat{V}\right)\right\}, \tag{3.20}$$

$$I_0\left(\hat{V}\right) = \frac{I_b}{I_{b,f}} \hat{V}^{-4} I_{0,f} .$$

In accordance with Equations (3.1)-(3.4), the ratio of beam currents in the last formula in (3.20) can be defined as

$$I_b / I_{b,f} = \hat{V}^{3/2}\left[\left(1+ j_{(0)}\right) / \left(1+ j_{(0)}\hat{V}^{3/2}\right)\right]. \tag{3.21}$$

The parameter $j_{(0)}$ is the ratio of the space charge limited density j_{SC} to the temperature limited current density j_{RD} at the nominal voltage.

For conventional gyrotrons, the relation between the interaction efficiency η and the orbital efficiency $\eta_{\perp}$ can be written as [3.12]:

$$\eta = \frac{\beta_{\perp 0}^{2}}{2\left(1-\gamma_{0}^{-1}\right)}\eta_{\perp} \,. \tag{3.22}$$

3.3 Results

The developed formalism was coded using the MATLAB environment. The dependence of the electron current on the applied voltage calculated by using Eq. (3.21) is shown in Fig. 3.1 for several values of the space-charge limited-to-temperature limited current density ratios. As one can see in this figure, when the current density ratio decreases from 10 to 1 this results in reducing the beam current at voltages about 0.4-0.5 of the nominal voltage by 1.6-1.9 times.

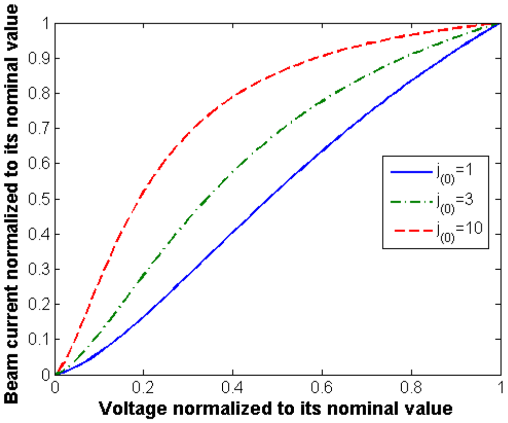

Figure 3.1 Current density as a function of voltage.

In the framework of the linear theory, self-excitation conditions of any mode do not depend on the presence of other modes in the resonator spectrum. So the start currents of all orthogonal modes can be calculated with the use of Eq. (3.5) and (3.7) separately.

The excitation of the $TE_{22,6}$-mode was studied. This mode is often used in MW-class gyrotrons. The parasitic higher-frequency modes that can be excited along with the operational mode are $TE_{23,6}$ and $TE_{24,6}$ modes. In order to calculate their start currents, it is necessary, first with the help of the equation (3.8) to determine the value of the coupling parameter G for these modes. The dependence of this parameter on the ratio of the electron guiding center radius R_0 to the wall radius of a cylindrical resonator R_w is shown for all three modes co-rotating with electron gyration which can be excited at the fundamental cyclotron resonance in Figure 3.2. The optimal value of beam injection for the operating mode (shown by a thin vertical black line in Fig. 3.2) is about 0.5 and the values of the coupling parameter for other modes should be also taken at this point.

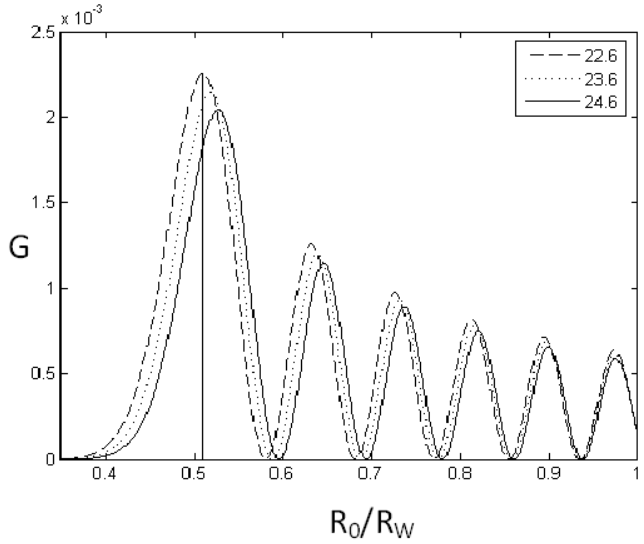

Figure 3.2 Parameter G as a function of the beam-to-wall ratio R_0 / R_w for modes $TE_{22,6}$, $TE_{23,6}$ and $TE_{24,6}$ modes. A thin vertical black line indicates the optimal beam position for excitation of the operating mode.

It was found from the equations (3.5) and (3.7) that there is a range of the detunings Δ for which the oscillations can be excited. This means that these modes can be excited either at different magnetic fields or, alternatively, if the magnetic field is fixed, at different voltages. Since eigenfrequencies of the $TE_{23,6}$ and $TE_{24,6}$ modes are higher than the eigenfrequencies of the $TE_{22,6}$-mode, the same value of the detuning Δ for those parasitic modes can be realized (when the magnetic field is fixed) at lower voltages because the voltage decrease increases the relativistic electron cyclotron frequency. Corresponding dependences of the start currents on the voltage for all three modes are shown by solid lines in Fig. 3.3. For the analysis we assumed that the gyrotron is driven by an electron beam with the nominal beam voltage at 80 kV, the nominal current is 40 A, and the orbital-to-axial velocity ratio at this voltage α is equal to 1.4. It is also assumed that the L/λ ratio is 4.0, the cavity Q-factor is 500 and the external magnetic field corresponds to the maximum interaction efficiency of the $TE_{22,6}$-mode at the nominal voltage.

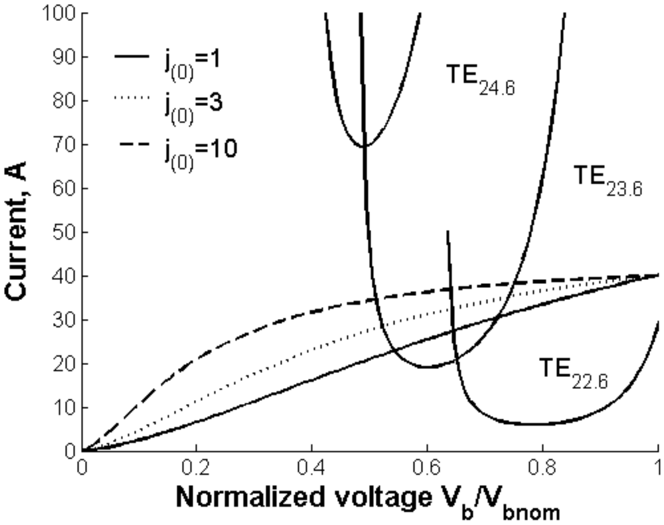

Figure 3.3 Self-excitation zones.

From the figure 3.3 it can be seen that the start current of the first parasitic $TE_{24,6}$-mode is located in the range of voltages between 0.4 and 0.6 of the final voltage, but even its minimum value is much larger than the final beam current (40 A). So this mode is not dangerous for gyrotron operation. However, the second parasitic mode $TE_{23,6}$, can easily be excited. The dependence of the beam current on the voltage which is shown in Fig. 3.3 corresponds to that shown in Fig. 3.1. These lines indicate that even when $j_{(0)} = 1$ the self-excitation condition for the $TE_{23,6}$-mode with the Gaussian axial structure of the cavity field can be fulfilled in a small region of intermediate voltages. In the results shown in Fig. 3.3 at the voltage corresponding to the minimum start current of the $TE_{23,6}$-mode ($V_b \approx 0.6V_{b,f}$) the beam current in the case of $j_{(0)} = 1$ is about 40% lower than in the case of $j_{(0)} = 10$. It should be noted that the this analysis does not provide the design solution for a particular tube, but rather aims at demonstrating the concept. For calculations that utilize of self-consistent codes, such as MAGY [3.15], the calculated start current is two times higher than calculated by simple theory.

This statement is illustrated by Fig. 4 reproduced from Ref. 22. As one can see, the minimum start current calculated for the Gaussian axial structure which are shown in Fig. 4a on the left are close to 10-12 A, while the minimum start current calculated with the use of the self-consistent code MAGY which are shown in Fig. 4b on the right are above 20 A.

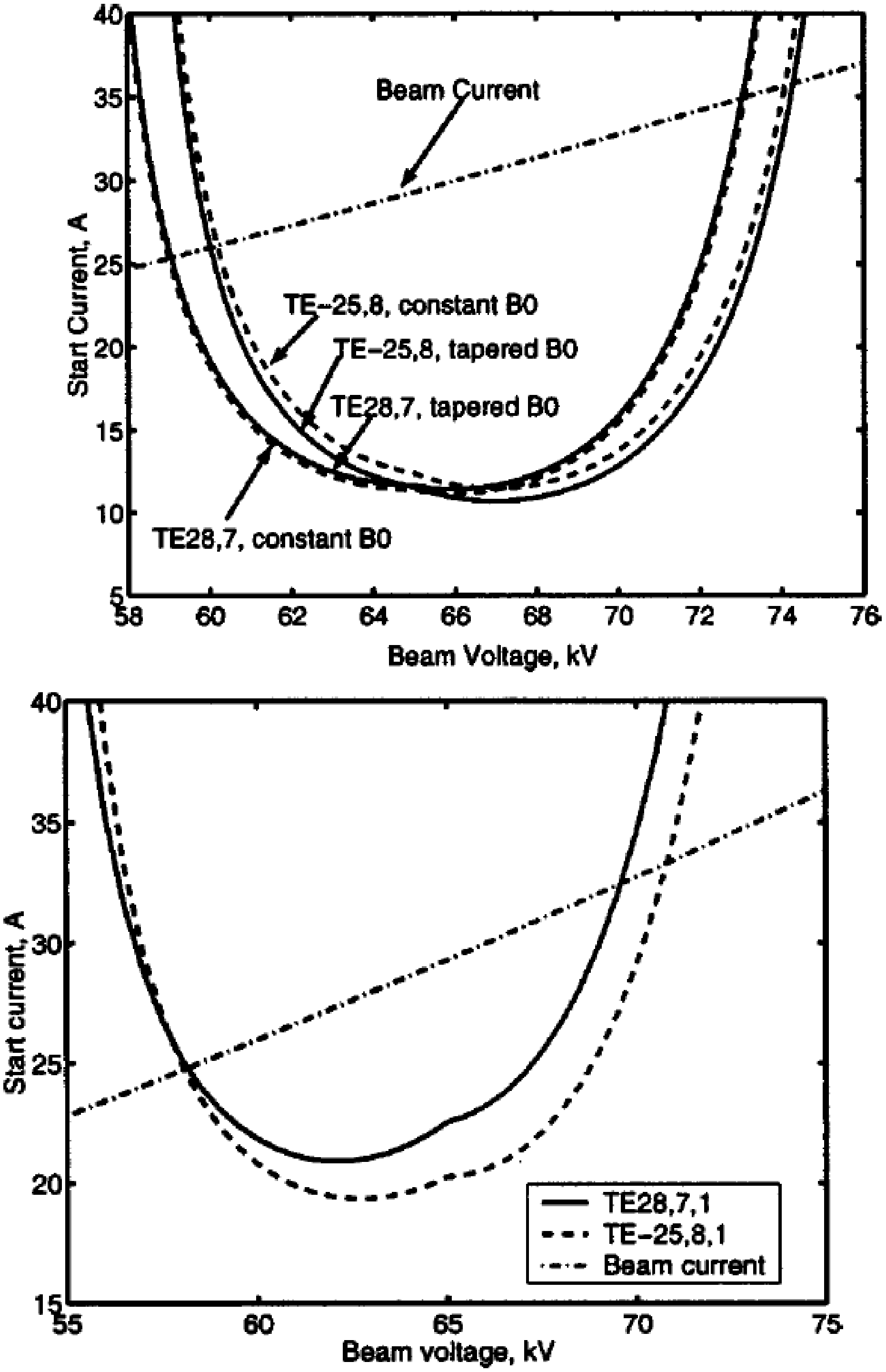

Figure 3.4 Start currents calculated in (top figure) the cold-cavity approximation and with the use of (bottom figure) the self-consistent code MAGY for a 110-GHz CPI gyrotron (reproduced from [3.11]).

The dependences of normalized parameters on the beam voltage, which are given by Equations (3.20)-(3.21), are shown in Fig. 3.4. The values of these parameters for the final voltage are chosen to be optimal for yielding high orbital efficiency (71%) [3.12]. The normalized beam current is shown for two values of the space charge limited – to temperature limited current density ratio $j_{(0)} = 10$ and $j_{(0)} = 3$. The difference between them is, however, rather small, because the main role in evolution of this parameter is played by the $\hat{V}^{5/2}$ dependence which follows from the formula in (3.20) and Eq. (3.21). When the voltage varies from $V_b = 0.7V_{b,f}$ to $V_{b,f}$ the normalized length μ doubles, as one can see in Fig. 4. The most important, however, is the evolution of the normalized cyclotron resonance mismatch which increases with voltage and at voltages smaller than the final value can be close to that corresponding to the minimum start current. The efficiency at these mismatches is much smaller than at $\Delta\left(V_{b,f}\right) = \Delta_{opt}$.

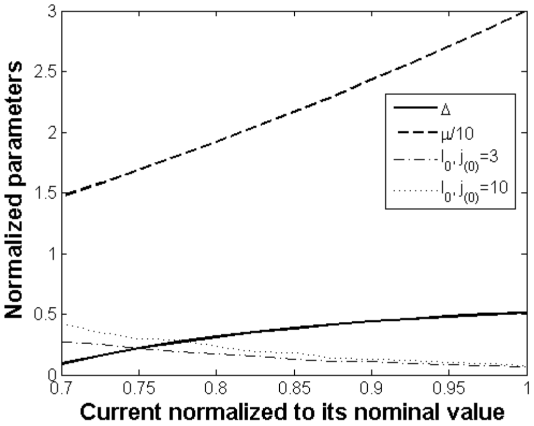

Figure 3. 5 Dependence of normalized parameters used in the gyrotron generalized theory on the voltage.

3.3.1 Collector loading

The next step was to analyze the effect of lowering the electron current density at intermediate voltages on the power dissipated in gyrotron collectors. It is assumed that the collector is at the same potential as the rest of the tube body (we assumed no potential depression). The electron optics is assumed to be in the framework of the adiabatic theory as described in the corresponding subsection of this chapter and it is possible to calculate the efficiency with the use of the nonlinear theory based on the cold-cavity approximation similar to the linear theory described in the subsection describing the self-excitation conditions. The evolution of corresponding normalized parameters of the generalized gyrotron theory with the voltage was shown in Fig. 3.5 above.

Calculations of power deposited at the collector were done for a gyrotron driven by a 80 kV, 40 A electron beam with the orbital-to-axial velocity ratio of 1.4 at the nominal voltage. Results of those calculations done for three values of the current density ratio are shown in Fig. 3.6. Bold circles there show the voltage at which the microwave oscillations start. At the final voltage, the beam power dissipated in the collector is about 1.8 MW. When the voltage goes down close to its value corresponding to the start of microwave oscillations in the case of high current density ratio ($j_{(0)} = 10$) the power dissipated in the collector exceeds 2 MW, while in the case of a lower ratio ($j_{(0)} = 3$) this power is close to the same value of 1.8 MW and in the case of $j_{(0)} = 1$ the collector power is even smaller than at the final voltage.

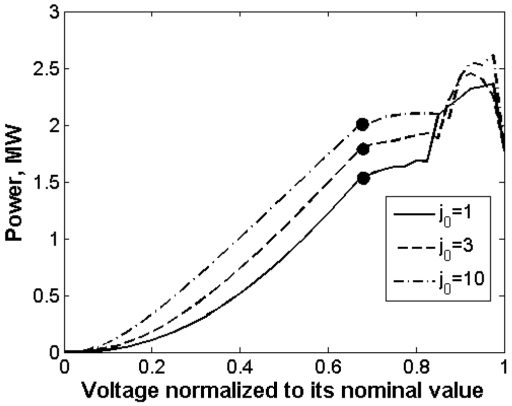

Figure 3.6 The power deposited at the collector at intermediate voltages for two cases with different space-charge-to-temperature limited emission ratio.

3.4 Conclusions

This chapter shown that there are some advantages in using magnetron injection guns with lower beam currents at intermediate voltages. The practical suggestions to realize the proposed scheme should be outlined. The lowering of the beam current at intermediate voltages can be realized by reducing the ratio of the space charge limited to temperature limited emission at the final voltage. To reduce this ratio, either the space charge limited emission should be reduced or the temperature limited emission should be increased (or both means should be used together).

In electron guns with space charge limited emission the beam current is commonly given as

$$I_b = PV^{3/2}. \tag{5.23}$$

where P is known as the perveance. So to reduce the space charge limited emission one should decrease the perveance of an electron gun. As a rule, this implies decreasing the electric field at the cathode that for diode-type electron guns means increasing the cathode-anode gap. In conventional MIGs this can be done either by increasing the anode radius or decreasing the cathode radius.

In the conventionally used Magnetron Injection Guns (MIGs), keeping the cathode radius fixed and increasing the anode radius may result in increasing the overall transverse size of a tube and, hence, require substantial modifications into the design of cryomagnets, namely increasing an outer dimater of the solenoid and the inner bore. Since this step will increase the cost of cryomagnets, it is unlikely that such a decision will be very attractive. Alternatively, one can keep the anode radius fixed and decrease the cathode radius. A simple analysis indicates, however, that such step is unrealistic for the following reasons. As follows from Eq. (3.12), the cathode radius and the electron guiding center radius in the interaction space are related as $R_{cath} = \sqrt{\alpha_B} R_o$. So, when the beam position in the interaction space is determined by the wavelength and the coupling to the operating mode [see Eq. (3.9)], decreasing the cathode radius means to lower the magnetic compression factor. Correspondingly, the cathode should be shifted towards the interaction space. Such positioning of the cathode in the region of stronger magnetic fields, as follows from the adiabatic invariant (3.13), means increasing the electron orbital velocity near the cathode. Since this velocity defined by (3.14) is linearly proportional to the electric field at the cathode and inversely proportional to the magnetic field near the cathode, we come to conclusion that for making the cathode radius smaller we must increase the electric field at the cathode, which is just opposite to our intention to reduce it.

In other words, combining (3.12) with (3.16) one can define the cathode radius by the following formula

$$R_{cath} = \left(\frac{\gamma_0 B_0}{E_{\perp,c}} \right)^{1/3} R_0 . \tag{3.24}$$

As follows from Eq. (3.24), when the guiding magnetic field, the beam voltage and the beam position in the interaction space are given, there is the minimal value of the cathode radius that is determined by the maximum of the electric field at the cathode limited by the DC breakdown, and the lowering of this electric field results in increasing the corresponding radius of the cathode.

Inverted MIGs offer in this regard much more flexibility because the radius of the inner electrode which plays the role of the anode there is not directly related to the beam position in the cavity. So one can fix the position of the emitter and reduce the radius of the inner electrode for lowering the electric field in the cathode-anode gap.

Here are few last comments regarding the operation of MIGs in various regimes. There are a number of reasons why, at present, gyrotron developers prefer to use electron guns operating in the temperature limited regime. First of all, it is easier to design such guns. Second, there is already a great experience accumulated with such MIGs. In this regard, it should be noted that there are also some successful designs and experiments with MIG-guns operating in the space-charge limited regimes [3.16]. In some design studies of MIGs it was found, however, that just in the region where both contributions are of the same order, i.e. $j_{SC} \approx j_{RD}$, the velocity spread is quite large. In our case, however, this fact is only beneficial. Indeed, if there is a significant electron velocity spread when the beam voltage passes through the region of excitation of a high-frequency parasitic mode, this spread will increase the start current and, hence, facilitate avoiding the excitation zone.

To figure out how important these arguments are, a realistic design of a MIG-gun operating with lower electric fields at the cathode should be performed and the dependence of the current density and the velocity spread on the beam voltage in such gun should be analyzed. In this regard, it should be mentioned that for a real device not only the electron gun should be accurately designed, but also the start current should be calculated more accurately with the use of a self-consistent approach (e.g., the code MAGY[3.15]) instead of the cold-cavity approximation.

Chapter 4: The role of RF melted microparticles in the operation of high-gradient accelerating structures

4.1 Introduction

Breakdown in accelerating structures has a long history of study; however, there is still no single theory that gives a full explanation of this complicated phenomenon. The experimental studies are complicated by the fact that the accelerating structures are not usually accessible until their failure. This significantly complicates the process, since no insight into the development of the processes that happens inside the structure can be given. There are numerous theories describing the possible stages of this process. The proposed theories and the corresponding models were recently reviewed in [4.1]. This review paper contains the references to the original papers by P. Wilson [4.2] and the others who proposed the initial models. One of the proposed mechanisms that can trigger the breakdown, as suggested by [4.3], is as follows: consider a small piece of metal that can move away from a protrusion located in the region of strong RF electric field. This small clump of metal is constantly bombarded by field emitted electrons to such degree that it becomes ionized: then, local plasma is formed and finally RF breakdown occurs. The detailed description of the process of field emission that leads to ionization of such microparticle was thoroughly analyzed in [4.4] and is well understood. The results of this work were published Physical Review Special Topics, Accelerators and Beams [4.5] and were reported at a number of scientific conference and workshops and published at these meetings proceedings. These include: 14th Advanced Accelerator Workshop and 2nd International Particle Accelerator Conference.

The focus of this chapter of the dissertation is to study another role that these micro-particles may play in the operations of high gradient structures. In what follows the model describing the heating of a micro-particle in high electromagnetic field is developed. The presented analysis shows that a microparticle extracted from a protrusion and traveling from the region of strong RF electric field to the region of strong RF magnetic field, can be heated and melted even without any bombardment by electrons. This melted particle or clump can later impinge on the surface of the structure and form a local surface nonuniformity, which may initiate further events, since the metal can be solidified in a way that enhances the field emission, leading to even further increase of the emitted electrons and produced heating. The model to describe the process of heating and melting of microportrusions on the surface of the accelerating structure will be described in the chapter 6 of this dissertation.

4.2 Dissipation of electromagnetic energy in small microparticles

Microwave heating is an important topic in engineering and science. It is well understood and has a number of applications, such as sintering of ceramics [4.6], heating of the catalysts in chemical reactions [4.7], heat treatment of mineral ores [4.8], regeneration of molecular sieves [4.9] and modern lithographic processes [4.10]. At the same time, microwave heating processes also impede the performance of some systems and may cause damage to living tissues. It is known that the contaminants on metallic and dielectric surfaces that can be heated by RF field can cause significant damage to different components of various RF systems [4.11, 4.12].

The various studies of the thermal effects in biological systems that were exposed to microwave radiation [4.13] show the importance of this subject for the biological sciences.

In most of these studies the description of the process proceeds through the macroscopic constitutive relations, namely $\vec{D} = \varepsilon\vec{E}$ and $\vec{B} = \mu\vec{H}$. The imaginary parts of permittivity ε and permeability μ provide the quantitative measure for the electromagnetic energy absorption.

The treatment of scattering and dissipation of electromagnetic waves by small microparticles that have dimensions much smaller than a wavelength was analyzed in the classical work by Landau and Lifshits [4.14] with a reference to the original treatise by Rayleigh [4.15] who studied the scattering, but not dissipation of light by small particles. As follows from Sec. 73 in [4.14], the RF energy dissipated in a small micro-particle during the pulse of duration τ is equal to

$$W = \frac{\omega\tau}{2} V\left(\alpha_e''\varepsilon_0\left|\vec{E}\right|^2 + \alpha_m''\frac{1}{\mu_0}\left|\vec{H}\right|^2\right). \tag{4.1}$$

Here ω and $\vec{E}\left(\vec{H}\right)$ are the frequency and electric field amplitude of the wave, τ is pulse duration of the RF field, V is the volume of micro-particle and α_e'' and α_m'' are imaginary parts of the electric and magnetic polarisabilities of the micro-particle. (In (4.1), the average intensity of the RF electric field is equal to the average intensity of the RF magnetic field.)

The idea behind the method that was used to treat the problem of microparticle heating in the RF field can be described as follows. The wave fields (electric – for α_e and magnetic – for α_m) are written for the spaces inside and outside the particle accounting for the particle geometry; the field in the external region contains two components – the external quasi-uniform field and the perturbation caused by the microparticle. Then, at the particle surface the relevant components of these fields should be matched separately according to the known boundary conditions.

The simplest configuration of a microparticle that can be used for initial estimates is a sphere. For a small sphere of radius a the volume in (4.1) is $V = \left(4\pi / 3\right) a^3$ and for metals the imaginary part of the electric polarisability of such a micro-particle, in accordance with (72.2) of [4.13], is given by:

$$\alpha_e'' = \frac{9}{4\pi} \frac{\varepsilon''}{4 + \left(\varepsilon''\right)^2} \tag{4.2}$$

where $\varepsilon'' = 4\pi\sigma / \omega$ (σ is the conductivity of the given metal). The imaginary part of the magnetic polarisability is given in the solution of problem 1 in Section 45 of [4.14] as:

$$\alpha_m'' = -\frac{9}{16\pi}\left(\frac{\delta}{a}\right)^2 \left[1 - \frac{a}{\delta} \frac{\sinh\left(2a/\delta\right) + \sin\left(2a/\delta\right)}{\cosh\left(2a/\delta\right) - \cos\left(2a/\delta\right)}\right]. \tag{4.3}$$

From this formula it can be concluded that the magnetic polarisability depends only on the ratio of the sphere radius to the skin depth $\delta = 1/\sqrt{\pi f \mu\sigma}$. The dependence of the magnetic polarisability on the this ratio is shown in Fig. 4.1 from which it follows that the maximum of the function, and hence the maximum of the RF field absorption happens when the ratio of the radius to skin depth of the microparticle is approximately 2.4, i.e. the sphere radius of about 2.4 skin depth. As an illustrative example, consider SLAC structures that were developed for the next generation of linear colliders. They are designed to operate at 11.424 GHz, which means that for the case of copper the skin depth in this case is about $0.6\mu m$ and the maximum of the absorption happens for the particles of several micrometers in diameter. The functional dependences of the imaginary parts of the magnetic polarizability as given by (4.3) are similar to the ones obtained by Y.Y. Lau and colleagues [4.16].

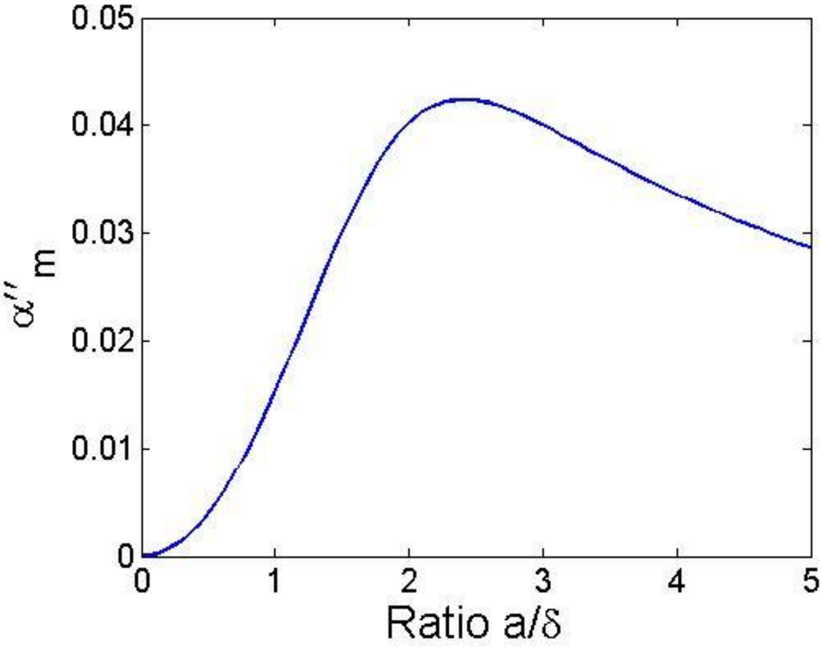

Figure 4.1 Imaginary part of the magnetic polarisability of a small sphere as a function of the ratio of the sphere radius to the skin depth.

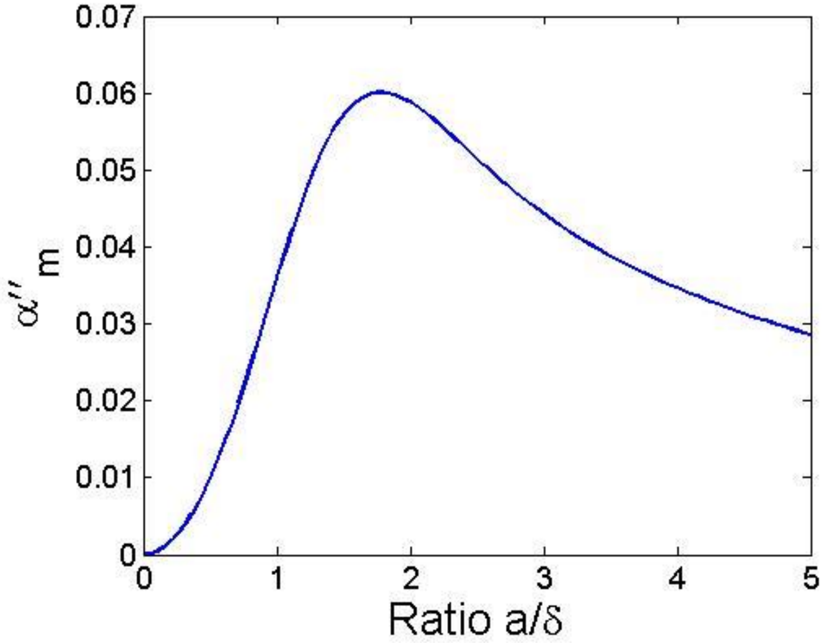

Figure 4.2 Imaginary part of the magnetic polarisability of a small cylinder oriented perpendicularly to the direction of the wave magnetic field.

As follows from comparison of (4.2) with (4.3) and Fig. 4.1, the magnetic polarisability plays the dominant role in determining the microwave energy dissipated in a metallic sphere of a radius on the order of a skin depth. The contribution from the electric field becomes important only when the radius of the micro-particle is much smaller than one nanometer independent on the operating wavelength. When such a small metallic sphere is located close to the surface of the accelerating structure, there can be significant enhancement of the electric field. This issue is discussed in great detail in [4.16]. However, in the present analysis α_e'' was not taken into account.

The evaluation of the RF energy dissipation for the different shapes of the particles can be performed in the same way, as it was done for the sphere. For instance, Landau and Lifshitz [4.14] in the second and third problems of Section 45 consider a small metallic cylinder of a radius a oriented perpendicular or parallel to the direction of the magnetic field of the wave. For the magnetic polarisability in the case of perpendicularly oriented cylinder they give the following formula:

$$\alpha_m = -\frac{1}{2\pi}\left[1 - \frac{2}{ka}\frac{J_1(ka)}{J_0(ka)}\right]. \tag{4.4}$$

In (4.4) $k = (1+i)/\delta$ is the complex wavenumber, hence the Bessel functions depend on a complex argument. In such a case, as known in the literature describing the processes in imperfect conductors [4.17], these functions should be expressed via Kelvin functions $\mathrm{ber}_{0,1}(x)$ and $\mathrm{bei}_{0,1}(x)$ [4.18]. The dependence of the imaginary part of the magnetic polarisability (4.4) on the ratio of the cylinder radius to the skin depth obtained with the use of these functions is shown in Fig. 4.2 which looks quite similar to Fig. 4.1. Even though the peak value of this polarisability is higher (0.06 versus 0.042 for a sphere), the corresponding ratio of the radius to the skin depth yielding the maximum polarisability is smaller (1.8 versus 2.4 for a sphere). When a cylinder is oriented parallel to the direction of the magnetic field its polarisability is two times smaller [4.14]. Note that in [4.14] only the limiting cases of small and large radii in comparison with the skin depth are considered, while in the present study these restrictions are removed. As follows from [4.14], the imaginary part of magnetic polarisability of a cylinder perpendicular to the wave magnetic field in the case of a radius much smaller than the skin depth is 2.5 times larger than that for a sphere, while in the opposite case of a large radius it is almost the same (corresponding coefficient is 1/2 for a cylinder versus 9/16 for a sphere). In the latter case (when a microparticle can be treated as a macroparticle) Equations (4.1)-(4.4) yield for the density of losses the same dependence (proportionality to $\omega\delta$) as the usual RF surface loss formula.

4.3 Critical fields and pulse duration

The dissipation of microwave energy defined by (4.1) leads to a temperature rise of this micro-particle. After the temperature reaches the melting point some energy is expended on melting the microparticle. Correspondingly, the energy balance describing the process of heating and melting a microparticle can be represented as:

$$W = W_H + W_M \, , \tag{4.5}$$

where the first and second terms in the right-hand side corresponds to the energy required for heating up to the melting temperature and for melting, respectively. In the same fashion, all the process can be subdivided into two stages.

4.3.1 First stage: the temperature rise to the melting point

During this stage ($0 \le t \le t_H$), the temperature increases up to the melting temperature of the material. In this stage, the energy balance equation, in line with (4.1) and the standard definition of the temperature rise, has the form:

$$\frac{\omega t}{2} \alpha''_m |H|^2 = c_T \rho_d \Delta T \; . \tag{4.6}$$

In (4.6), c_T is the specific heat capacity and ρ_d is the density of a given metal. When the temperature rises up to the melting point ($\Delta T = T_m - T_0$), Eq. (4.6) determines the corresponding instant of time $t = t_H$.

Equation (4.6) contains the imaginary part of the magnetic polarisability which depends on the a/δ ratio, which, in turn, can be temperature dependent. In fact, the temperature expansion of the radius a with the temperature rise can be neglected because for typical materials (such as copper, aluminum, tungsten or molybdenum) it is smaller than 2%. However, the changes in the skin depth can be significant. As follows from the Bloch-Gruneisen law which predicts the linear dependence of the material resistivity on temperature for temperatures exceeding 2/3 of the Debye temperature (which is valid for temperatures equal to and exceeding the room temperature), the skin depth is proportional to $\sqrt{T}$. Correspondingly, the argument for the functions defining the magnetic polarisability (4.3)-(4.4) can be redefined as:

$$\frac{a}{\delta} = \left(\frac{a}{\delta}\right)_0 \sqrt{\frac{T_0}{T}} \,. \tag{4.7}$$

When the nonlinear dependence of α''_m on temperature is taken into account it allows us to rewrite (4.6) in dimensionless variables to obtain an ordinary first-order differential equation:

$$\frac{dy}{dt'} = \Psi(z) \,. \tag{4.8}$$

In (4.8), $y = \Delta T / T_0$ is the temperature rise normalized to the initial temperature, $t' = (\omega t)|H|^2 / 2T_0 \rho_d c_T$ is the normalized time, the function $\Psi(z)$ describes the dependence of the imaginary part of the magnetic polarisability defined for specific geometries by (4.3) and (4.4) and its argument $z = a/\delta$ denotes the radius-to-the skin depth ratio (4.7), i.e. $z = z_0 / \sqrt{1+y}$.

The solution of (4.8) is shown in Fig. 4.3 for two values of the initial ratio $(a/\delta)_0 = 2.0$ and 4.0 by solid lines. Dash-dotted lines show asymptotic solutions obtained for the case when the temperature dependence of conductivity in the skin depth is ignored. While the asymptotic solutions shown by straight dash-dotted lines have obvious interpretation, the curves shown by solid lines exhibit more interesting behavior. Initially, when the temperature rise is small, the temperature rise for the case $(a/\delta)_0 = 2.0$ exceeds the temperature rise in the case $(a/\delta)_0 = 4.0$. However, as the temperature rise becomes larger, the dissipation in the case $(a/\delta)_0 = 2.0$, in line with data shown in Fig. 4.1, rapidly decreases, while the dissipation in the case $(a/\delta)_0 = 4.0$ increases because the ratio a/δ decreases with the temperature rise. They become equal when the temperature rise is about 0.3 of the initial temperature. Then, as is seen in Fig. 4.3 (and on the corresponding inset), the dissipation and corresponding temperature rise in the case $(a/\delta)_0 = 4.0$ becomes much larger than in the case $(a/\delta)_0 = 2.0$. Comparison of the temperature rise in a microsphere with an optimal initial ratios $(a/\delta)_0 = 2.3$ with the temperature rise in a micro-sphere having initial ratio $(a/\delta)_0 = 5.0$ shows that the temperatures become equal much later, when the temperature rise is about 1.6 of the initial temperature.

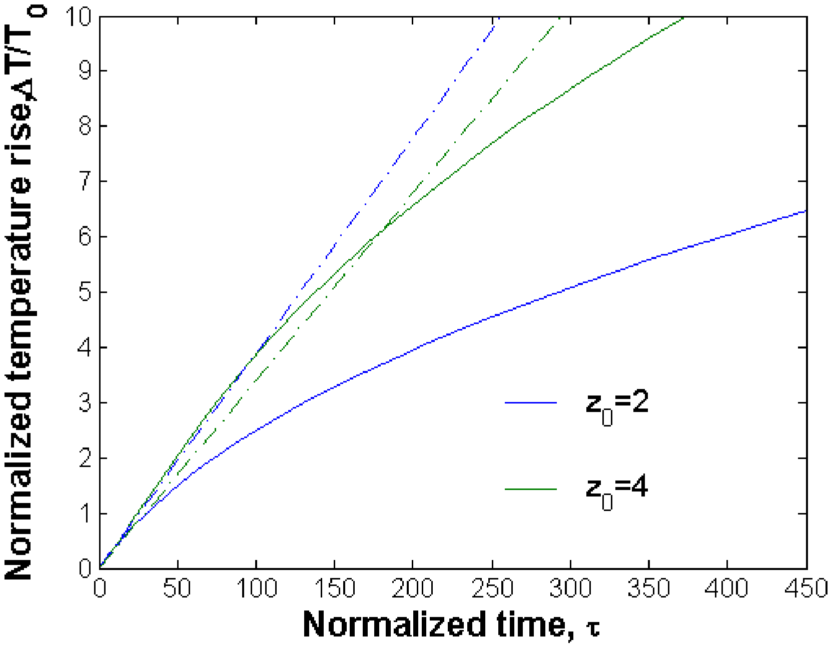

Figure 4. 3 Temperature rise (normalized to the initial temperature) as the function of normalized time for a micro-sphere with the temperature dependence of the skin depth taken into account (solid lines) and ignored (dash-dotted lines).

To correctly interpret the data shown in Fig. 4.3 the estimates of the ratio of the melting-to-initial temperature ratio for specific materials should be made. For example, for such materials as copper, aluminum, tungsten and molybdenum the (a/δ) ratio decreases at the melting point by 2.1, 1.76, 3.5 and 3.26 times with respect to initial values, respectively. This means, first, that this effect should be taken into account when the optimal ratio (a/δ) is estimated based on the data shown in Figures 4.1 and 4.2. These optimal values (2.4 for the sphere and 1.8 for the cylinder) should correspond to melting temperatures. Correspondingly, the optimal initial values of these ratios $\sqrt{T_m/T_0}$ are larger. (Here the word “optimal” means that particles of this size will be melted faster than others.) For example, in the case of a copper micro-sphere the optimal value of the initial ratio $(a/\delta)_0$ is about 2.1 times larger than 2.4, i.e. the optimal initial radius is close to five times initial skin depth.

Then, the curves like those shown in Fig. 4.3 should be used for estimating the instant of normalized time corresponding to the temperature rise from the initial to melting temperature, viz., for example, for copper $y_{\max} = \left(T_m - T_0\right)/T_0 \approx 3.5$. As follows from Fig. 4.3, in this case for a copper microparticle with $(a/\delta)_0 = 4.0$ the normalized time required for reaching the melting temperature is about 80. By using normalization of this time variable given after (4.8) this value can be converted into the time interval for given amplitude of the RF magnetic field and the other parameters. Having described the stage of the particle heating, the next subsection describes the process of particle melting.

4.3.2 Second stage: melting

During the second stage ($t_H \le t \le \tau$), the energy balance equation can be written as follows:

$$\frac{\omega\left(\tau - t_H\right)}{2}\alpha''_m \left|H\right|^2 = \rho_d \Lambda\,, \tag{4.9}$$

where Λ is the specific heat of melting. This equation determines the time interval required for melting a heated microparticle in the magnetic field of given amplitude.

The dependence of the critical magnetic field defined as the value of magnetic field that, first, causes the temperature to rise to the melting point and, then, melt a particle is shown for several metals in Fig. 4.4 for spherical microparticles with different initial values of the $(a/\delta)_0$ ratio. Asymptotic solutions obtained ignoring the temperature dependence of the skin depth are shown by dash-dotted lines. It was found that the discrepancy between asymptotic solutions and exact ones is larger when the initial ratio $(a/\delta)_0$ equals 2 (Fig.4.4a) because in this case the temperature rise causes drastic decrease in the imaginary value of the magnetic polarisability shown in Fig. 4.1. As follows from these results, in strong enough fields of long pulse duration such micro-particles can be melted. Consideration of a cylinder oriented perpendicularly to the wave magnetic field yields similar results. Results shown in Fig. 4.4 were obtained neglecting the radiation losses. To prove this assumption it should be noted that, for example, the energy required for melting a copper (specific heat of melting of copper is $0.385\,J \cdot g^{-1} \cdot K^{-1}$, density of copper is $8.02\,g \cdot cm^{-3}$) spherical microparticle with the radius of 1.3 micron (mass of the particle is) is about $1.8*10^{-8}$ Joules, while, as follows from the Stefan-Boltzmann law, the power of the black-body radiation from such a sphere at the melting temperature is close to $3.7 \cdot 10^{-6}$ W and, hence, in microsecond pulses the radiated energy is equal to $3.7 \cdot 10^{-12}$ Joules, i.e. about 4 orders of magnitude smaller, than the energy required to melt the particle.

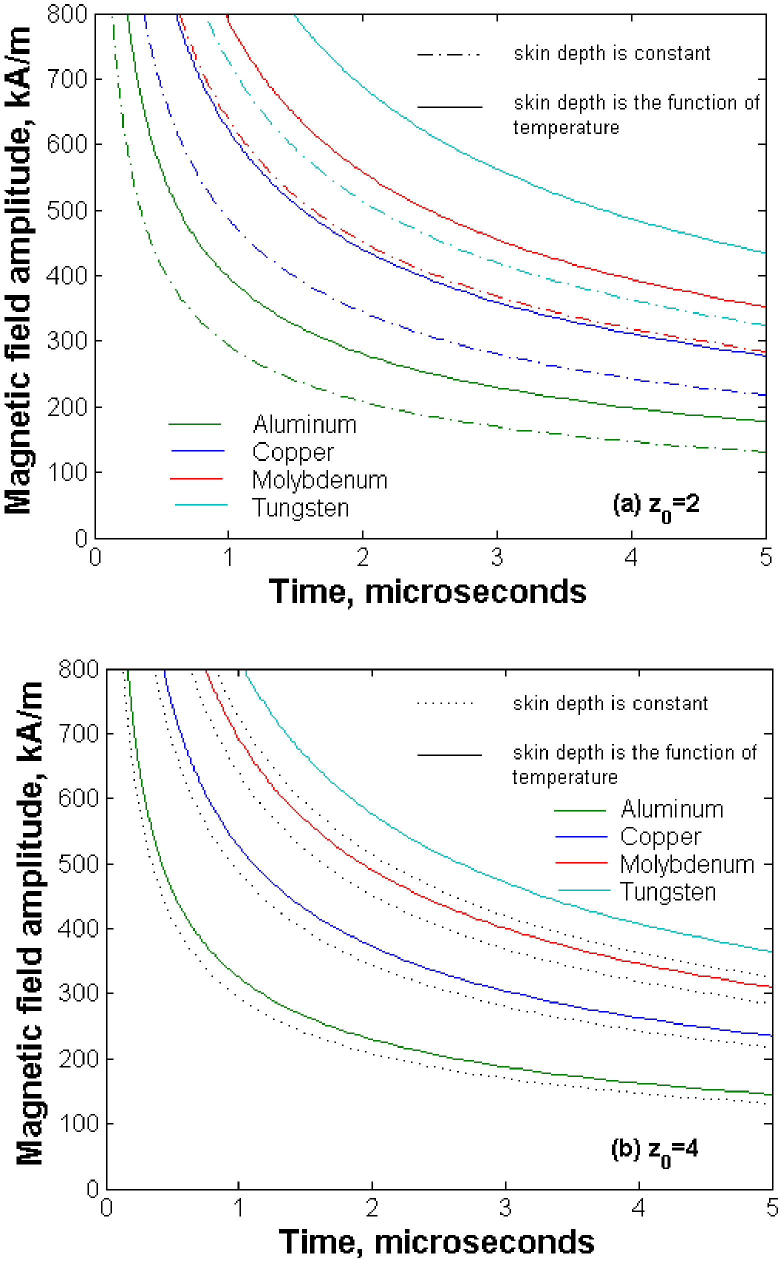

Figure 4.4 Critical field amplitude leading to melting of spherical microparticles with the initial (a/δ)-ratio as shown.

4.4 Practical consideration

The results of the analysis based on the proposed method show that it is quite possible that microparticles of a micron size can be melted in strong pulsed RF magnetic fields with long enough pulse duration. Magnetic fields and pulse durations required for melting of a particle are shown in Fig. 4.4. Their values are close to the numbers that were realized in SLAC experiments with X-band standing-wave structures [4.19]. For example, results reported in Ref. 4.18 indicate that in standing-wave X-band structures the accelerating gradient of 70 MV/m results in the surface magnetic field at the inner edge of the iris of about 700 kA/m. This field corresponds to magnetic fields shown in Fig. 4.4 for pulse durations on the order of hundreds of nanoseconds for materials like aluminum and in microsecond range for the materials that have higher melting point, i.e. copper and especially tungsten and molybdenum.

In this discussion with a short remark regarding the question of the origins of the micropartilces inside the accelerating structure. The standard process of fabrication of those structures involve various methods of polishing to achieve surface roughness on the order of several nanometers and extreme cleanliness of the entire structure during subsequent handling and assembly. However, in the recent studies it was shown that, in line with mechanical fracture [4.20] and atomistic models [4.21], microparticles can appear on the irises of the structures where strong RF field is localized, since strong electrostatic tension may cause the tip of an asperity on the iris to break off. The study of the erosion of the input coupler was done recently and is discussed in [4.22]. The image on Fig 4.5 is reproduced from this work for illustrative purposes, since this is the picture of the cavity after its failure, it is impossible to determine the size of the microparticles extracted during different stages of the process. To test the described formalism it will be necessary to inspect the cavity after a short series of breakdown events. These experiments to the best of my knowledge haven't been done yet, but they are planned at SLAC (personal communications with V. Dolgashev).

The presence of the micropartilces can have serious impact on the subsequent operation of the structure. Between RF pulses such a melted clump of metal can hit a structure surface and cause the appearance of spots of melted metal that were observed in numerous experiments. Examples of such surfaces are shown in Fig. 4.5. When such a clump impinges on the metallic surface and forms a spot with a radius of a few microns, as shown in Fig. 4.5. The height of the rims of such spot is less than a micron, but is enough for creating significant nonuniformity and hence magnification of the RF electric field resulting in field emission of a dark current from those areas. The radius of 5 skin depth in copper translates to about 3 micron size for wave frequency of 11.4 GHz.

These results show that microparticles of a micron-size can be melted in strong RF magnetic fields with long pulse duration. Then, such melted clumps can impinge the structure surface and initiate further breakdown events. This scenario can be treated as an alternative to building up a small protrusion from the surface initially melted by a strong RF magnetic field (this case was considered [4.2]). The next section of this thesis deals with the effects of repetitive pulsed operation on the process of heating and melting of these particles.

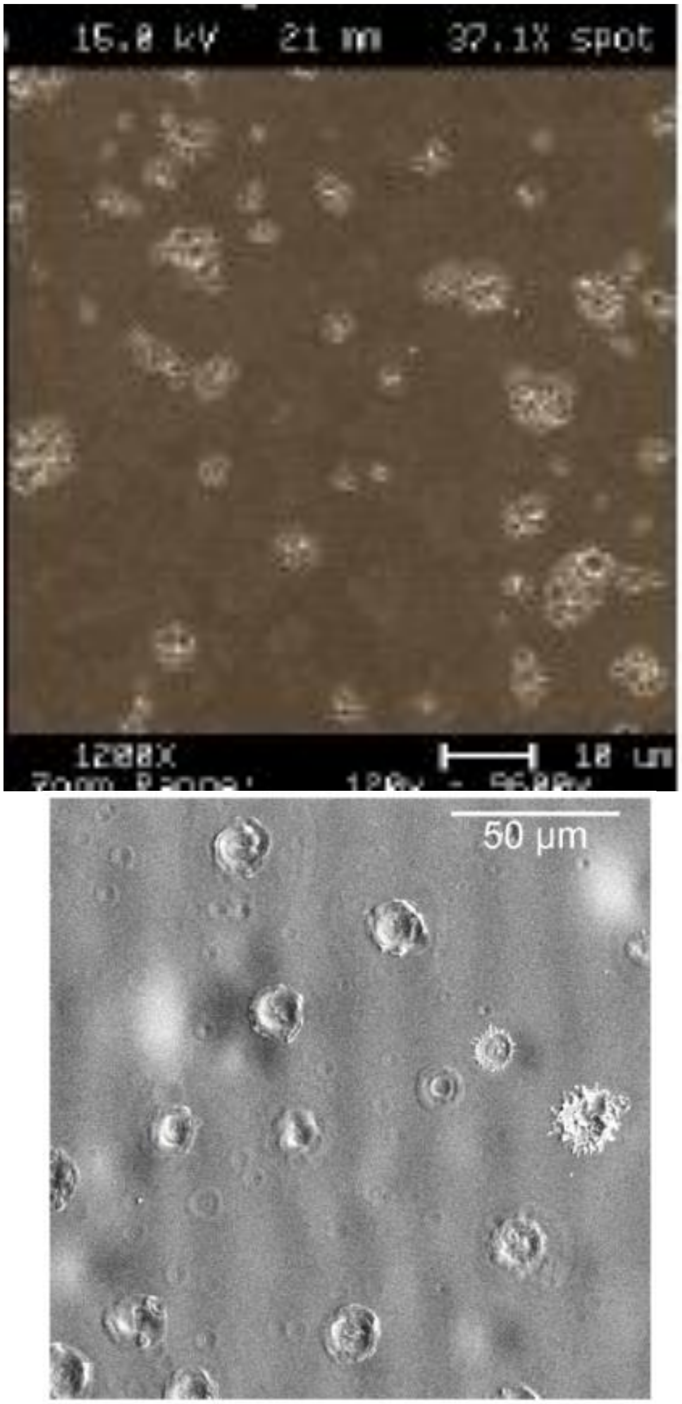

Figure 4.5 Splashes on the metallic surface of a structure: top - courtesy of L. Laurent, SLAC, bottom – reproduced from [4.21].

4.5 Possible effect of high-power microwave devices operated in pulsed regime

The next section continue the study of the processes that degrade the performance of a high power accelerating structures. As was shown in the previous chapter and in

[4.23] small metallic particles that can be found in various high-power microwave (HPM) devices can be substantially heated and melted by the RF electromagnetic field. This process of melting happens in the regions where RF magnetic field in the structure is strong. In particular, in the previous chapter using the general expressions for polarisabilities of small microparticles given in [4.24] it was found, that the RF magnetic field plays much more important role in microparticle heating than the RF electric field and, second, that the maximum absorption takes place when the size of microparticles is on the order of the skin depth. These studies lead to further broadening of our understanding of the details of the breakdown process. In the previous chapter, a limiting case was studied, i.e. the case when a metallic particle absorbs enough microwave energy in a single pulse to increase the temperature up to the melting point and the subsequent melting. Such a situation takes place when the microwave energy per pulse is large, i.e. the power of the RF electromagnetic field is high and the pulse duration is long. When an HPM device operates in a rep-rate regime another situation may take place. If the power and/or pulse duration is not sufficient to melt the metal in a single pulse a gradual heating resulting and subsequent melting of a microparticle can occur in the course of many pulses. It should be noted that, while in the case of particle melting in a single shot, the blackbody radiation is negligibly small, this radiation may result in substantial cooling between the pulses when the device operates in a rep-rate regime. In this case the conditions for melting of a microparticle can be met for a wider range of operating parameters of the RF field of the accelerating structure. The analysis performed in this chapter deals with this case, studying the effect of repetion rate on the process of melting of a microparticle inside the HPM structure. The results of this work were reported and published in IEEE Transactions on Plasma Science [4.23] and reported at APS DPP meeting in 2010.

4.6 Equations

The operation of any rep-rate device consists of a sequence of intervals having duration $T = 1/f_{rep}$. In each of such intervals there are two stages: (A) RF power on – the duration of this stage is the RF pulse duration τ_{RF}; and (B) RF pulse off. The duty cycle of operation is $D = f_{rep}\tau_{RF}$. The typical case for accelerators is to operate in the regime in which the duration of the stage B is much longer than the duration of the pulse, then $T_B \approx T = 1/f_{rep}$. The description of the stage A, the heating was given in the previous chapter. In this chapter the equation that describes the cooling of the microparticles and results of analysis are presented.

4.6.1 Stage A: Heating

As was shown in the previous chapter (Eq. 4.6), during stage A the temperature of a particulate rises according to:

$$\frac{dT}{dt} = \frac{\omega\alpha''_m}{2c_T\rho_d}\mu_0\left|H\right|^2 . \qquad (4.10)$$

In (4.10) c_T and ρ_d are the specific heat capacity and the density of a given material, respectively, and H is the amplitude of the RF field in A/m; α''_m is the imaginary part of the magnetic polarisability given in [4.23] for particles of a spherical and cylindrical geometries. This polarisability depends on the ratio of the particle radius a to the skin depth δ. Also taking into account the linear dependence on the temperature of the material resistivity (according to the Bloch-Gruneisen law), the a/δ ratio which is the argument in formulas defining the polarisability can be redefined as

$$a/\delta = (a/\delta)_0 \sqrt{T_0/T}\ . \tag{4.11}$$

Here T_0 and the subscript ‘0’ denote the initial temperature and the initial value of the radius-to-skin depth ratio, respectively. The analysis performed in this chapter is applicable to a particles of the spherical geometry, for which, as given in [4.23]:

$$\alpha''_m = -\frac{9}{16\pi}\left(\frac{\delta}{a}\right)^2\left[1-\frac{a}{\delta}\frac{\sinh(2a/\delta)+\sin(2a/\delta)}{\cosh(2a/\delta)-\cos(2a/\delta)}\right]. \tag{4.12}$$

4.6.2 Stage B: Cooling

During stage B, i.e. between the pulses the temperature of a particle decreases in accordance with the Stefan-Boltzmann law as:

$$\frac{dT}{dt} = -\frac{A\sigma T_0^4}{Vc_T\rho_d}\left(\frac{T}{T_0}\right)^4. \tag{4.13}$$

In (4.14), $\sigma = 5.67\cdot 10^{-8} W/m^2K^4$ is the Stefan-Boltzmann constant, A and V are the particle surface area and volume, respectively; for a sphere $A/V = 3/a$. Equation (4.14) is written for the case of black-body radiation. The applicability of this law to the cooling of particles in real high-power microwave devices is discussed later in this chapter. Under the assumption that the temperature dependence of parameters in Eq. (4.14) can be neglected, this equation can be integrated analytically.

Normalizing the temperature to its initial value and the time to the wave frequency allows us to rewrite Equations (4.10) and (4.13) as:

$$\left(\frac{dT}{dt}\right)_A = K_A \alpha''_m, \tag{4.14}$$

$$\left(\frac{dT}{dt}\right)_B = -K_B T^4. \tag{4.15}$$

In (4.14) $K_A = \mu_0 |H|^2 / 2c_T \rho_d T_0$ which for copper and initial room temperature yields $K_A = 6 \cdot 10^{-16} \left|H\left(A/m\right)\right|^2$. In (4.15), $K_B = (A/V)(\sigma T_0^3 / c_T \rho_d \omega)$ which for the same conditions and a wave frequency of 11.424 GHz yields $K_B = 1.8 \cdot 10^{-11} / a\left(\mu m\right)$.

When the RF magnetic field is high enough, the temperature can reach the melting point and then the particle can be melted in just the first shot. This is the case studied in the previous section of this chapter and in [4.5]. At lower magnetic field values, however, the temperature evolution during a sequence of shots should be considered. In the course of this evolution, the temperature may reach a steady state when the temperature rise during the time of one RF pulse is equal to the temperature fall during the interval between the shots. When both, the temperature rise and fall in a single shot, are small enough, we can approximate the temperature on the right-hand sides of Eqs. (4.14) and (4.15) by a constant value and find this stationary value T_{st} equating the temperature rise $\left(\Delta T\right)_A = K_A \alpha''_m \left(T_{st}\right) \omega \tau_{RF}$ to the temperature fall $\left(\Delta T\right)_B = K_B \left(T_{st}\right)^4 \omega / f_{rep}$. This determines the stationary value of the temperature about which the temperature oscillates in a rep-rate regime by the following simple equation ($D = f_{ref} \tau_{RF}$ is the duty cycle)

$$T_{st}^4 = \left(D K_A / K_B\right) \alpha''_m \left(T_{st}\right). \tag{4.16}$$

When this stationary temperature exceeds the melting temperature, the particle, apparently, will be melted in a long enough series of pulses. However, when the stationary temperature is lower than the melting temperature the particle will remain hot, but solid.

4.7 Results

Here are the estimates for the operational parameters required for reaching a stationary temperature equal to the melting temperature of a small copper sphere immersed in a strong RF magnetic field of 11.424 GHz frequency. The radius of the sphere was assumed to yield the maximum absorption at the melting temperature. For copper this temperature is 1350K, and assuming that the initial temperature is room temperature, 300K (so, the normalized temperature in Eqs. (4.14)-(4.16) is equal to 4.5). As was shown in the previous chapter, the absorption is at the maximum $\alpha''_{m,\max} \approx 0.042$ when the radius-to-skin depth ratio is close to 2.4. Since the skin depth in copper for the given frequency at the room temperature is about 0.6 micron, from Eq. (4.12) it is found that the optimum radius, taking into account temperature dependence is close to 3 micron. For this radius, the parameter K_B in the equations above is equal to $K_B = 6 \cdot 10^{-12}$. Then, from Eq. (4.16) it follows that the heating may result in melting when the product of the intensity of the RF magnetic field and the duty cycle obeys the following inequality:

$$D \left| H\left(\frac{MA}{m}\right) \right|^2 \geq 10^{-4} . \qquad (4.17)$$

In such alloys as CuZr used in recent joint (US-Japan-Europe) experiments with high-gradient accelerating structures [4.25] the situation is quite similar because the density and specific heat capacity are practically the same as for copper, while the melting temperature is a little lower (1250K instead of 1350K). This difference makes the right-hand side of (5.8) equal to $0.73 \cdot 10^{-4}$. For such typical regimes of operation in room-temperature accelerating structures with one microsecond pulse duration and a rep-rate of 100 pulses per second the duty cycle is 10^{-4}. Thus, the condition given by Eq. (4.17) in such regimes is fulfilled when the amplitude of RF magnetic field exceeds 1MA/m. Most of the experiments described in [4.25] were carried out with magnetic fields in the range of 0.5-0.6 MA/m. The duty cycle of HPM sources developed for radar applications can be, however, much larger. Correspondingly, the RF magnetic field amplitude satisfying (4.17) can be much lower than 1 MA/m.

The temporal evolution of the temperature of a particle is shown in Fig. 4.6. To obtain these results we multiplied the normalized time in Eqs. (4.14)-(4.15) by the parameter K_A: we introduced $\tau = K_A \omega t$. This allowed us to rewrite Eqs. (4.14)-(4.15) as:

$$\left(\frac{dT}{d\tau}\right)_A = \alpha''_m(T), \tag{4.14a}$$

$$\left(\frac{dT}{d\tau}\right)_B = -KT^4, \tag{4.15a}$$

where $K = K_B / K_A$. Every interval between RF pulses corresponds to the normalized time $\tau_B = K_A \omega / f_{rep}$. The normalized duration of one RF pulse is $\tau_A = K_A \omega \tau_{RF}$. Results presented in Fig. 4.6 show the temperature rise with a number of RF pulses of different duration for the case of a 100 Hz repetition frequency. As one can see, the stationary temperature exceeds the melting point (for the initial room temperature the melting temperature of 1350 K corresponds to the normalized temperature value of 4.5) when the RF pulse duration is longer than 1 microseconds. This melting level can be reached in about 10 pulses which occur in a small fraction of one second.

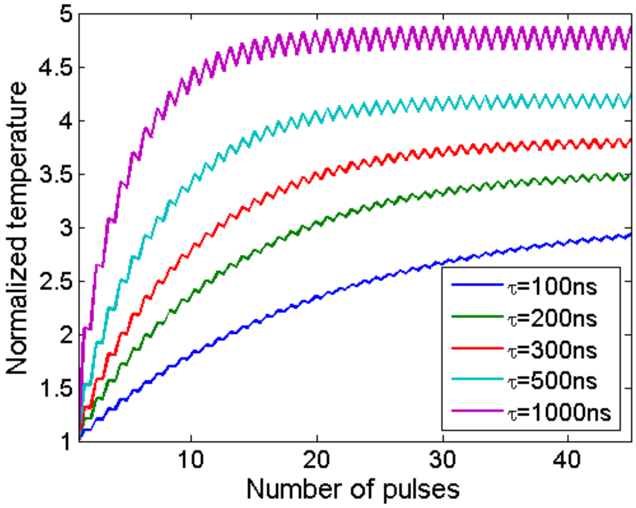

Figure 4.6 Normalized temperature rise as a function of number of pulses for several values of pulse durations.

<u>*4.8 Applicability of the Stefan-Boltzmann law*</u>

The analysis was performed for temperature losses between RF pulses by using the Stefan-Boltzmann law. This law describes thermal radiation losses of a black body which has perfect absorptivity and is in thermodynamic equilibrium with the environment. Neither of these two conditions is met for a particulate heated by an RF field in a well polished metallic structure in an accelerator or in a cavity/waveguide of an High Power Microwave (HPM) source. It is known that the intensity of thermal radiation in solids is affected by the nature of the particular solid as well as by the shape of an emitting body; the deviation of this intensity from that prescribed by the Stefan-Boltzmann law is especially strong near the phase transition to liquids, i.e.

near the melting point [4.26]. Since the particles under consideration may have an arbitrary shape, it makes sense to limit our consideration by prescribing in the Stefan-Boltzmann law a certain attenuation factor C characterizing the fact that our 'grey' particle emits less radiation than a black body.

We proceed by multiplying the right-hand sides in Eq. (4.13) and Eq. (4.15) by the factor C, which is equivalent to shortening the time interval between RF pulses, i.e. increasing the repetition rate with other parameters fixed. Results of corresponding calculations in which all other parameters were chosen the same as for the data shown in Fig. 4.6 (RF pulse duration is 500 ns) are shown in Figure 4.7. The dotted line in Fig. 4.7 shows the temperature rise in a single long RF pulse in the absence of thermal emission. As one can see, reduction of the cooling rate by a factor 0.6, which is equivalent to the increase of the repetition frequency by about 1.7 times, leads to the melting of a particle which in the case of the black body radiation would remain heated up to 1250K. As it follows from the equation (4.17) this reduction in cooling, which is equivalent to the increase of the repetition rate, indicates that particle can be melted at lower values of RF magnetic field.

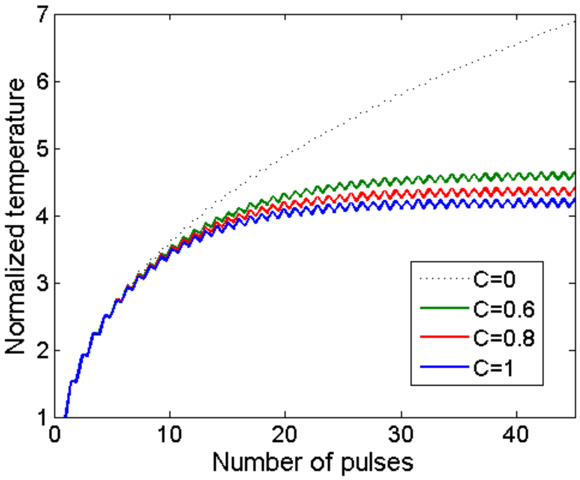

Figure 4. 7 Normalized temperature rise for several values of the factor C. Dashed line corresponds to absence of cooling mechanism, i.e. C=0. Pulse duration is 500ns.

4.9 Discussion

In the previous chapter some discussion was given on how those micropartilces appear in the RF structure. It makes sense to briefly discuss possible reasons for the appearance of such metallic micro-particles in microwave structures. In addition to the reasons given in the previous chapter, some particles may appear from the flanges and other elements of the different parts of accelerating structures. It should be noted that in the case of rep-rate operation such particles will not lie on the structure walls, but spend most of the time inside the structures without contacting the walls. The reasons for this could be either hydraulic pressure in cooling channels of MW-class HPM sources (see, e.g. [4.27]) or the electromagnetic pressure of RF power localized inside such structures resulting in the vibration of walls. Here is a simple example to illustrate the point. Assuming that due to some wall vibrations a particulate leaves the wall with an initial velocity 1cm/sec one can easily find, this particle will standoff from the wall at a distance not exceeding 0.5 mm and stay without contacts with the wall for about 0.2 sec. In the case of rep-rate operation with a 100 Hz repetition frequency this time interval corresponds to 20 RF pulses. Hence, in accordance with results shown in Figures 5.1 and 5.2, there will be enough time for this particulate to be heated and melted in a sufficiently strong RF magnetic field.

There are some planned experiments [4.28] in which metallic microparticles will be placed inside microwave circuits of rep-rate HPM sources without thermal contacts with the walls. Results of such experiments can validate the estimates and stimulate further theoretical efforts on this topic.

Chapter 5: Heating of the microprotrusions

The last chapter of this dissertation is dedicated to the subject of studying the temperature rise in microprotrusions. As was mentioned in the previous chapters, RF breakdown is the major factor that limits the operation of high-gradient accelerating structures. The overview of the existing scenarios that may lead to the breakdown is given [5.1]. The analysis of some processes that lead to the development of RF breakdown were given in the previous chapters of this dissertation. The overview [5.2] gives the summary of possible scenarios that lead to breakdown events. In all the described scenarios micro-protrusions play an important role, since in the vicinity of these protrusions the electric RF field is greatly enhanced, leading to the increase of the dark current caused by field emitted electrons. This chapter is dedicated to the development of a model that can describe the field distribution inside the protrusion and provide the description of protrusion heating. The results presented in this chapter were reported in a number of scientific conferences[5.3] [5.4]

5.1 Fields outside microprotrusion

5.1.1 Fields near microprotrusion

In the analysis of the role of microprotrusions in the operation of high-gradient accelerating structures the main attention is paid to the electron field emission from the protrusion apex. This field emission follows the Fowler-Nordheim (FN) relation [5.5], which will be given later in this chapter. The local electric field is given by $E_{local} = \beta \cdot E_0$, where E_0 is background field in the structure and β is some constant called the field amplification or field enhancement factor. With the inclusion of the related (local field dependent) area factor, the total current from a protrusion can be linked to the current density at the protrusion apex, which is governed by the FN relationship. This consideration implies that the total current mimics the dependency of the apex current density with respect to the background field. The value of the field enhancement factor is related to the shape of the microscopic protrusions present in the cavity. Due to the strong exponential dependence of the Fowler-Nordheim current density on the local field [5.5] the current flowing through the protrusion changes dramatically with the change of the field amplification factor β. However, in experiments the exact value of this amplification factor, as a rule, is not known; therefore typically its value is assumed to be reasonable for interpreting the results of the experiments. The issue of local field amplification was actively studied in early work on the field initiated vacuum arc (see, e.g. Ref. [5.6] and references therein) and in vacuum microelectronics where the field emitters and field emitter arrays are used in various areas of science and technology (the historical overview is given in Ref. [5.7]).

The spatial distribution of a high frequency electric field in a resonator or accelerating structure can be found by solving the wave equation with appropriate boundary conditions (Helmholtz equation). For protrusions that are much smaller than the wavelength of the applied high-frequency field, the field is electrostatic on the spatial scale of the protrusion and is governed by the Laplace's equation for the potential. This chapter is limited to the study of quasi-cylindrical microprotrusions with a diameter on the order of the skin depth at the operational frequency or less than that value. For X-band frequencies and the copper structures, this means that the objects under consideration are of the size of a micron or smaller.

The use of electrostatic modeling for studying some dynamic processes at RF and microwave frequencies can be justified by the following arguments. Although RF and microwave frequencies induce some effects on metals, as far as field emission is concerned, such electrostatic modeling is sufficient to find field enhancement because the time scale of field emission (sub-picosecond) is much shorter than any other relevant RF or microwave time scale. For example, electrostatic models are used to describe field emitter arrays intended to field emit in time with a 5 GHz RF field [5.7]. In theoretical models for such devices, electrostatic modeling of the field emitters is the commonly accepted approach to understand their operation, even though the conditions during the operation are not static.

5.1.2 PCM Model

There are numerous studies in the literature dedicated to the analysis of the field distribution in the vicinity of protrusions of various shapes, including conical, elliptical, prolate spheroidal, fractal and others [5.8-5.11]. The analysis presented in this chapter describes the field distribution by using the Point Charge Model (PCM) [5.12, 5.13] which was recently developed for studying field emitters. This model can also be applied to the analysis of microprotrusions in accelerating structures. The PCM allows one to determine the potential outside the protrusion, protrusion shape and obtain the analytical expression for the field amplification factor.

The idea behind the PCM model is based on the method of images typically used to solve boundary problems in electrostatic configurations which involve some symmetry (see, e.g., [5.10]). It is that conductors present in the problem can be replaced by some charge distributions that yield the same form of the potential in the region of interest. Specifically, an alternative electrostatic problem in which the conductor is absent is considered; then a distribution of charges localized in the region of space formerly occupied by the conductor is added, and is adjusted in a way that the distribution produces zero potential on the surface that coincides with the surface of the conductor. From the uniqueness of solutions of the Laplace's equation it is known that the potential above this surface must be the same as above the actual conductor in the original problem. This approach is beneficial because for simply shaped protrusions the virtual charges provide a more straightforward way to solve the problem. In particular, the potential above a protrusion with cylindrical symmetry can be realized by a distribution of point charges assembled along the z axis (see Fig. 5.1a). Here, the first charge is put at the origin and each subsequent charge is put on the top of the sphere created by the isolated equipotential line of the previous charge, those equipotentials can be related to the virtual charge magnitude and can be determined from the boundary condition on the protrusion apex. In fact, the equipotential surface of the assembled charge distribution (marked as a bold black line on Fig. 5.1 (c) and (d)) is smooth and ellipsoidal or conical in nature, the detailed description of how these charges are assembled is given in the Appendix A.

In order to obtain a scalable analytical expressions for the potential, four model parameters should be fixed, namely the magnitude of the external field F_0, the height (alternately, the radius of the protrusion) of the equipotential line of the first charge a_0, the number of charges n and the ratio of the distances between successive

a_n values, or $a_n / a_{n-1} = b$ for all n. Consequently, all energies are measured in units of $F_0 a_0$, all lengths in units of a_0, and so on (the so-called “natural units” of Ref. [5.13]).

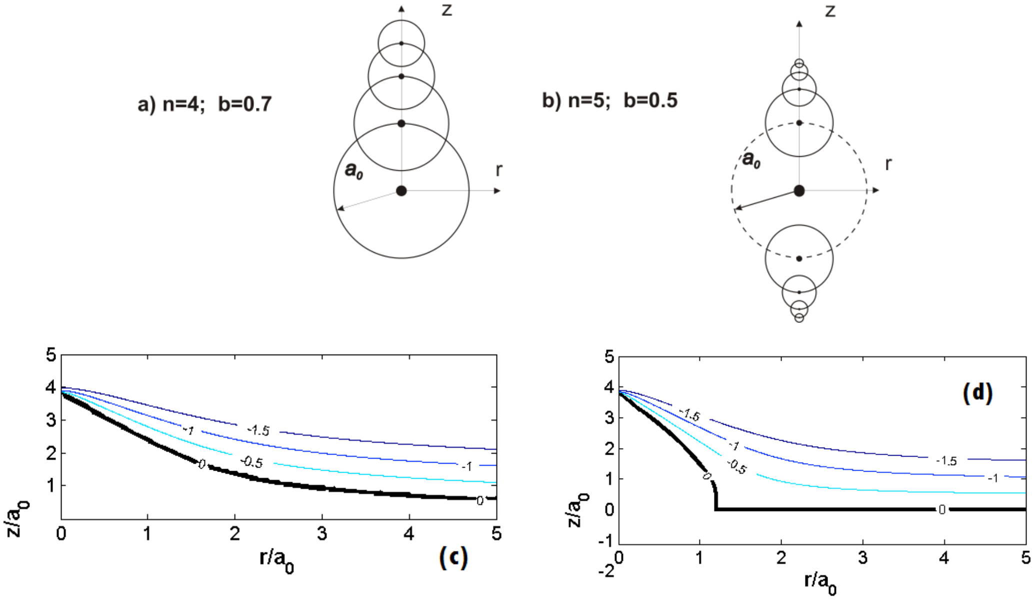

Figure 5.1 Charges assembly according to the PCM model: a) the monopole PCM, b) the dipole model, DPCM (the charge at the origin for the DPCM is omitted). Corresponding equipotential lines are shown in figures (c) and (d). The bold black line shows the zero potential which can be treated as the surface of the structure and a protrusion on it.

From the analysis of the PCM it follows that it is possible to determine the potential outside the protrusion and the field amplification factor analytically and the use of “natural units” allows for scaling arguments to be invoked. However, in the case of the PCM model with all virtual charges of the same sign (a so-called monopole model, Fig. 5.1a) the equipotential zero line from the charges set never intersects the plane *z=0.* This case does not correspond to the realistic situation. In numerical simulations this fact may lead to instabilities and greatly increase the computational time. To overcome this problem and to give a more realistic shape of the protrusion a so-called Dipole point charge model (DPCM) was developed [5.13].

In this model a set of charges is added to the initial assembly, as shown in Fig. 5.1b. Those charges are just the mirror reflection of the virtual charges assembled over the plane $z = 0$. The DPCM assembly results in an equipotential line that intersects the $z = 0$ plane.

In the case of the monopole model [5.12, 5.13] shown in Fig. 5.1a the potential has the following form:

$$V_n(r,z) = F_0 a_0 \left\{ -\frac{z}{a_0} + a_0 \sum_{j=0}^{n} \frac{\lambda_j}{\sqrt{r^2 + (z - z_j)^2}} \right\}. \tag{5.1}$$

where F_0 is background field, a_0 is the length scale associated with the primary point charge and dimensionless coefficients λ_j are proportional to the magnitudes of the point charges. They can be determined analytically assuming that the potential $V_n(r,z)$ satisfies $V_n(0, z_{n+1}) = 0$, where $z_{n+1} = \sum_{j=0}^{n} a_n = a_0 \left(1 - b^{n+1}\right) / \left(1 - b\right)$. Corresponding equipotential lines are shown in Fig. 5.1c. Here, a zero equipotential line does not intersect *z=0* plane, but rather asymptotically falls to zero for large values of r. Using this model a larger simulation cell can be used, but the potential will have some finite value at the numerical boundary which may lead to numerical instabilities.

In the case of the DPCM model the potential has the following form [5.12]:

$$V_n(r,z) = F_0 a_0 \left\{ -\frac{z}{a_0} + a_0 \sum_{j=1}^{n} \frac{\lambda_j}{\sqrt{r^2 + (z - z_j)^2}} - a_0 \sum_{j=1}^{n} \frac{\lambda_j}{\sqrt{r^2 + (z + z_j)^2}} \right\}, \tag{5.2}$$

where the second sum is the contribution from the charges (cf. (5.2) for the dipole model with (5.1) for the monopole model which neglects the second sum in (5.2) and has a λ_0 component). Corresponding equipotentials are shown in Fig. 5.1d. This assembly results into a zero equipotential line that has the intersection with $z=0$ plane.

The PCM model gives the shape of the protrusion, i.e. the surface of zero potential, which is denoted by $z_s(r)$. In order to describe whisker-like protrusions, a large number of charges n and the ratios $a_n/a_{n-1}=b$ close to one should be used, while the case of small n and b correspond to shallow protrusions. After the amplification factor β is calculated, the emitted current density on the surface is computed by calculating the normal electric field using (5.2) and inserting it in the Fowler-Nordheim [5.1] relation. The algorithm will be discussed in details later in this chapter; it also should be noted that the field magnification on the apex strongly depends on the radial coordinate, and, as a result of that, appreciable field emission from metals in the case of significant field amplification occurs at a small site (typically with area of the order of 10 nm^2). Typical values of the fields that produce field emission are of the order of 5GV/m; for example, for copper a 4GV/m field on the 10 nm^2 emission area produces a current of the order of 1nA.

5.1.3 Field enhancement

Appreciable field emission from metals occurs only when the field at the emission site is on the order of 5 GV/m. Typical fields on metal surfaces in high-gradient accelerators are on the order of 100 MV/m, i.e. about a factor of 50 lower. This means that in order to get significant field enhancement factors (in the range of 50-60) which may lead to significant dark current, it is necessary to have large enough number of charges in the model. The field amplification factor on the protrusion apex $\beta_n(r=0)$, as follows from (5.2), can be written as:

$$\beta_n(r=0) = -\frac{1}{F_0}\frac{\partial V_n(0,z)\big|_{z=z_{n+1}}}{\partial z} = 1 + a_0^2\sum_{j=1}^{n-1}\frac{\lambda_j}{(z_{n+1}-z_j)^2} + a_0^2\sum_{j=1}^{n-1}\frac{\lambda_j}{(z_{n+1}+z_j)^2}\ . \quad (5.3)$$

In the article describing the DPCM model [5.13] it was shown that for small ratio of subsequent virtual charges b the shape of the protrusion that yields significant field enhancement is physically unrealistic (in order to achieve required filed amplification factors the radius of the apex should be less than the atomic radius). Assemblies with a value of b that lies in range from 0.8 to 0.95 are used for the calculations. Figure 5.2 shows the dependence of field amplification factor on the number of charges for several values of b. For example, with 30 charges and *b=0.85* the field amplification factors as large as $\beta = 55$ can be obtained.

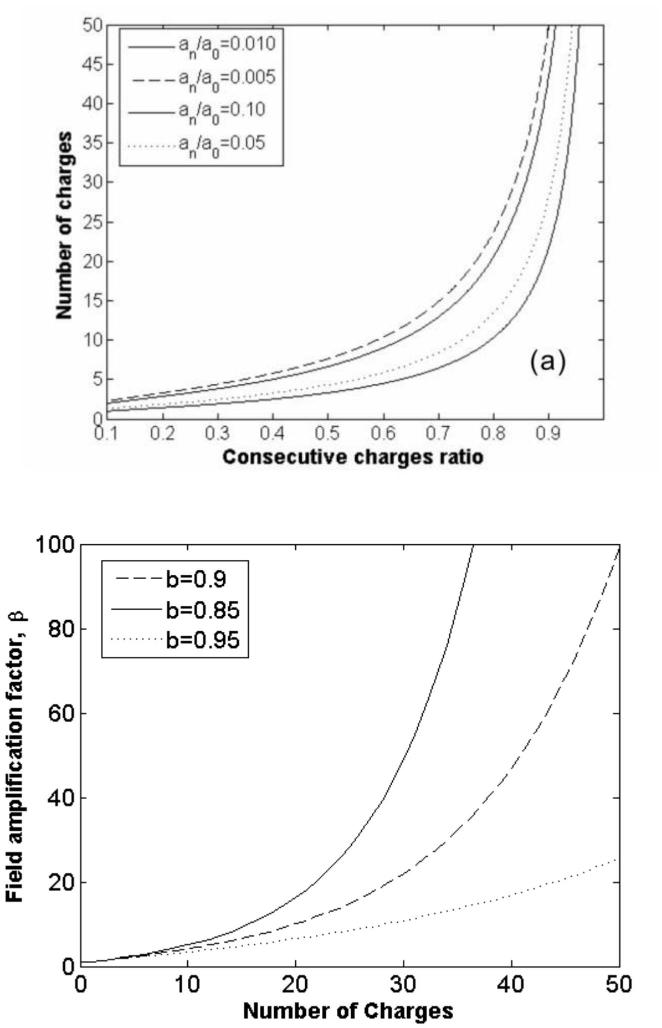

Figure 5.2 a) Number of charges required to achieve the given ratio between radii of the apex and the base of protrusion. b) Field amplification factor as a function of number of charges for different values of b.

5.2 Field inside protrusion

In order to find the potential and the current density inside the protrusion, an alternate problem to the one described in the previous section must be solved. Inside the protrusion that has the conductivity σ, which is high but finite, the current density and electric field are related by the point form of Ohm's law $\vec{J} = \sigma\vec{E}$. Conservation of charge requires $\nabla\vec{J} = \nabla(\sigma\vec{E}) = 0$. Further, it is assumed that the protrusion is much smaller than the wavelength (so $\vec{E} = -\nabla\phi$) and the electrical conductivity is uniform. As a consequence, the electric potential inside the protrusion satisfies the Laplace's equation:

$$\nabla^2 \phi = 0 \tag{5.4}$$

This equation satisfies following boundary conditions for the potential on the protrusion boundaries. First, the potential vanishes at the base of the protrusion:

$$\phi = 0 \text{ at } z = 0 \text{ .} \tag{5.5a}$$

Second, at the protrusion surface $z_s(r)$ the normal current density and, consequently, the normal electric field are prescribed:

$$\frac{\partial \varphi}{\partial x_n} = \varphi' \text{ at } z_s(r), \tag{5.5b}$$

where x_n is the normal to the surface and:

$$\varphi' = -J_n / \sigma \text{.} \tag{5.6}$$

In (5.6) J_n is the current density determined by the Fowler-Nordheim relation and the electric field just outside the protrusion.

After the fields outside the protrusion were determined, it was assumed that the protrusion is a perfect conductor and consequently set the electrical potential to zero on the surface of the protrusion. Taking into account the finite conductivity of the protrusion, the electrical potential will be nonzero on the protrusion surface according to the solution of (5.4). Under the assumption that the electrical conductivity σ is large enough, the small change in potential on the surface of the protrusion has negligible effect on determination of the potential outside the protrusion. Further, it was assumed that the current density below the protrusion is diffuse enough that the rise of potential at the base of the protrusion can be ignored. Thus, the boundary condition (5.5a) defines the potential at the base.

To solve the equation (5.4) numerically a finite difference relaxation scheme was used. Since the problem is symmetric with respect to the z axis, it was only solved in the positive part of r-z plane and the boundary conditions $\partial\varphi / \partial x_n = 0$ at $r = 0$ were applied. The application of boundary conditions at $r = 0$ and $z = 0$ is straightforward, but the condition at $z_s(r)$ is more difficult to evaluate. To match the solution to the boundary condition, the integrated electric flux $Q(r) = \int_0^r 2\pi r' \sqrt{1 + z_s'^2}\, \phi'(r') dr'$ was introduced and then this flux was matched to the numerical flux.

Once the scheme converges, the potential distribution is found for the region inside the protrusion. The solution of this problem also results in a small potential existing at the surface of the protrusion. In principle several iterations of the numerical solutions should be run until the potentials match on the surface, however, given the high conductivity and small surface potential these iterations are unnecessary and were omitted.

An example of 2D-nonuniform spatial distribution of the RF electric field inside a microprotrusion is shown in Fig. 5.3. This field is rather weak; its peak value near the apex slightly exceeds 3 kV/m. However, in metals with high conductivity this field causes significant current density. For example, in the case of copper with $\beta = 40$, $\Phi = 4.3 eV$ this peak electric field yields the current density of about

$0.18 A/\mu m^2$ that corresponds to the power density of about $0.53 mW/\mu m^3$. For the protrusion made of molybdenum these numbers are three times smaller.

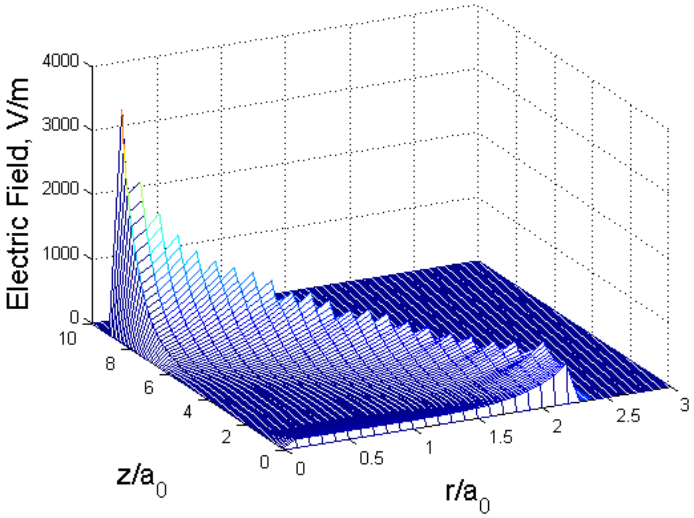

Figure 5. 3 Electric field inside protrusion: the external uniform RF electric field is 300 MV/m, number of charges in the DPCM model is 40 and the ratio b is equal to 0.9.

5.3 Protrusion heating

After the field and the current density inside the protrusion are determined, the volume power density can be calculated and the heat equation can be solved to determine the temperature rise inside the protrusion:

$$\frac{\partial \Delta T}{\partial t} = D\nabla^2 \Delta T + \frac{\left\langle \vec{J} \cdot \vec{E} \right\rangle}{c_\rho}. \tag{5.7}$$

In (5.7), ΔT is temperature rise, D is diffusivity of the material and c_ρ is the material specific heat. Angular brackets denote averaging over RF period. Eq. (5.7) implicitly assumes that $D = \lambda_T / c_p \rho$, (is dependent on the ratio of the thermal conductivity to the specific heat and the temperature) does not depend on the temperature. In the equation defining the diffusivity λ_T is the thermal conductivity, c_p is the specific heat and ρ is the density of the material. However thermal conductivity and specific heat are dependent on scattering rates of electrons amongst themselves and on scattering rate of the electrons with the lattice of metal atoms, so in general the diffusivity is temperature dependent. However, the complexity incurred by keeping the temperature dependence is in stark contrast to the relatively small difference it makes, as simulations of heat flow with and without a temperature dependent thermal conductivity show [5.12]. Therefore, the temperature-independent approximation for the diffusivity D is chosen for the simulations, but the temperature dependence of the electrical conductivity is taken in account in the source term [the last term in the right-hand side of Eq. (5.7)].

The heat propagation equation is the subject to the following boundary conditions: $\Delta T = 0$ at $z = 0$ and $\frac{\partial \Delta T}{\partial x_n} = 0$ at the surface of the protrusion $z_s(r)$, once again due to the symmetry of the problem the temperature rise is only determined in the first quadrant, and the boundary condition $\frac{\partial \Delta T}{\partial x_n} = 0$ at $r = 0$ is applied. For calculating the volume power density in the last term in RHS of (5.7) we use the simple relation between current density and electric field: $\vec{J} = \sigma(T)\vec{E}$. In this formula $\sigma(T)$ is the temperature dependent electrical conductivity which can be determined by the Bloch-Gruneisen law predicting a linear dependence of the material resistivity on temperature for temperatures exceeding 2/3 of the Debye temperature, i.e. for room temperatures and above (e.g., for copper and molybdenum, $T_D \approx 343K$ and *450K*, respectively).

The boundary condition for the electron current density at the protrusion surface implies that this current density it equal to the Fowler-Nordheim current density:

$$j_{FN} = \frac{a_{FN} F^2}{\Phi t^2} \exp\left\{ -\frac{b_{FN} \Phi^{3/2} v}{F} \right\}. \tag{5.8}$$

In (6.8), $F = eE_{RF} = eE_0 \sin \omega t$ is the periodic RF field at the emission site, Φ is the work function (in the range of 4-5 eV), a_{FN} and b_{FN} are constants equal to 1.37 A/eV and 6.83 (eV$^{1/2}$nm)$^{-1}$, respectively, and where, for metals under fields where tunneling is appreciable, convenient (in the sense of taking ratios of current densities) and reasonably accurate approximations are $v = 0.93869 - y^2$ and $t(y) = 1.126$, where the dimensionless variable is given by $y = 0.0379 F^{1/2} / \Phi$ for F in eV/micron and Φ in eV (see, e.g. [5.10]). In the case of RF fields of the X-band the wave period is about 0.1 nsec, while the temporal scale of protrusion heating is given by an RF pulse duration which typically is on the order of 100 nsec or more. Therefore, for analyzing the heating processes the heat source term should be averaged over an RF period. The difference between the DC and RF heating can be described by the function characterizing the ratio of the averaged to peak loss power (where the peak loss power corresponds to the field emission in DC fields at $E = E_0$):

$$\Psi = \frac{\left\langle j^2 \right\rangle}{\left[j_{FN}^{(0)} \right]^2} = \frac{1}{2\pi} \int_0^{\pi} \sin^4 \tau \cdot \exp\left\{ -13.6618 \cdot 10^9 v(y_0) \frac{\Phi^{3/2}}{F_0} \left[\frac{1}{\sin \tau} \frac{v(y)}{v(y_0)} - 1 \right] \right\} d\tau \;. \tag{5.9}$$

In (5.9) it was taken into account that in an RF cycle the field emission takes place only during one half of the RF period, $\tau = \omega t$. The variable y_0 in (5.9) corresponds to the peak value of the RF electric field. This function Ψ is shown as a function of the maximum surface gradient on the protrusion apex for several values of the work function in Fig. 5.4. As follows from Fig. 5.4, its value typically does not exceed 0.1. When the oscillating terms in the exponent play a negligible role, Eq. (5.9) yields this ratio of loss powers equal to 0.1875, but the exponential term reduces this ratio further (ref [5.14]).

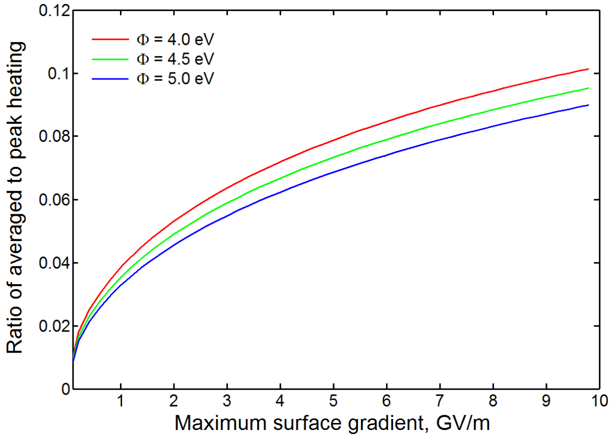

Figure 5. 4 Ratio of the average to peak loss power in protrusions.

Examples of a typical temperature distribution inside the protrusion are shown in Figure 5.5. These examples are shown for the number of virtual charges equal to *n*=38 and *b*=0.9, which corresponds to the amplification factor β=40, as was used in the evaluation of the Fowler-Nordheim current density above. The RF electric field far from protrusion is equal to 300 MV/m. Here the temperature rise is not very large. However, when the number of charges is increased to 42 leading to the increase of the amplification factor to 50, it is possible to achieve melting temperature for both copper and molybdenum in the case of pulses of microsecond duration.

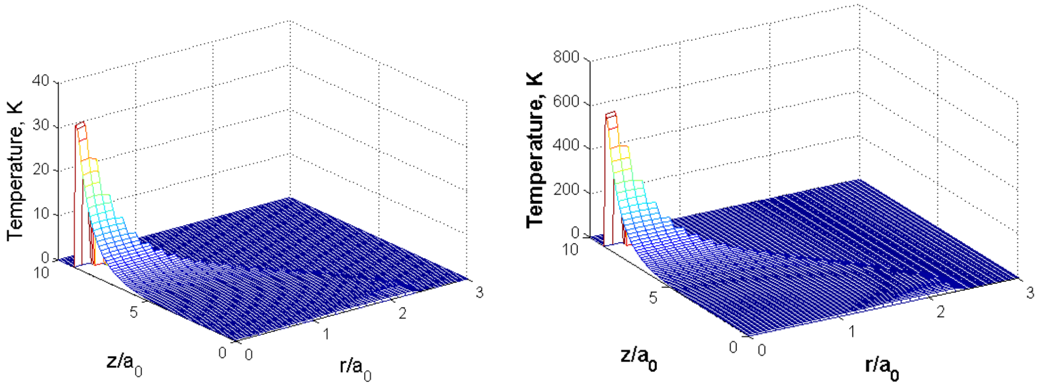

Figure 5.5 Temperature rise in copper (left) and molybdenum (right) microprotrusions in the base RF electric field 300 MV/m. Results are shown for the case *b*=0.9 and *n*=38 (field amplification is about 40) when the temperature reaches the steady state and its peak is well below the melting level. Pulse duration in this case is 300 nanoseconds.

In order to verify the calculations a simplified model of the field distribution inside the protrusion was used. It was assumed that a uniform electric current flows through the protrusion, its shape is given by the DPCM model, and that the radius of the apex a_{apex} corresponds to the last charge in the assembly. Then the current density is:

$$J(z) = J_{FN} \frac{a_{apex}^2}{a(z)^2}. \tag{5.10}$$

Under these assumptions the following heat propagation equation should be solved:

$$\frac{\partial}{\partial T}(\Delta T \cdot A(z)) = \frac{\partial}{\partial z}\left(D \cdot A(z) \frac{\partial \Delta T}{\partial z}\right) + \int dS \cdot \frac{\langle \bar{J} \cdot \bar{E} \rangle}{C_p \rho}, \tag{5.11}$$

where $A(z) = \pi a(z)^2$ is the area of the corresponding layer, ΔT is temperature rise, *D*, C_ρ and ρ are the material thermal diffusivity, specific heat and density, respectively.

There are known numerous attempts to find partial solutions of Eq. (5.7). A number of such cases were discussed in [5.14]. Some of them are based on the assumption that the temperature of the protrusion base remains constant during the pulse and, hence, the heat does not propagate from microprotrusion to the bulk of the structure. This assumption is, apparently, valid only when the height of a microprotrusion h is much larger than the heat propagation distance:

$$h >> \sqrt{D\tau} \,. \tag{5.12}$$

In (5.12) τ is the microwave pulse duration and the diffusion coefficient $D = \lambda_T / c_p \rho$ (again here λ_T is the thermal conductivity) is equal for copper and molybdenum to $0.12 \mu m^2 / ns$ and $0.0613 \mu m^2 / ns$, respectively. Thus, in the case of 100 nsec pulses the heat propagates a distance of a few microns and that can be comparable with the height of microprotrusions. So, the condition (5.12) can be fulfilled in the case of short enough pulses and long enough protrusions. Since we have assumed that the protrusion radius is on the order of the skin depth, condition (5.12) can be used only for describing fast processes in thin and long microprotrusions. Note that just this sort of microprotrusions with height-to-base ratio about 8-10 that was found to be responsible for the dark current in Ref. 5.15. Corresponding figures were also reproduced in Ref. 5.16. Later some mechanical fracture [5.17] and atomistic [5.18] models were developed for explaining this phenomenon (see also Ref. 5.19).

To observe significant heating in short pulses the electron current density should be high enough. Let us make an estimate for a thin cylindrical microprotrusion in which the electron current density is equal to the Fowler-Nordheim current density from the protrusion apex j_{FN}. The total energy of the Joule heating of such a protrusion during a pulse of duration τ is $W = (\langle j_{FN}^2 \rangle / \sigma) V\tau$ and this energy causes the temperature rise $\Delta T = W / c_T \rho_d V$. Here $V = \pi a^2 h$ is the protrusion volume, in angular brackets we have the electron current density squared averaged over the RF period which is determined above by Eq. (5.9) as $\langle j^2 \rangle = \left| j_{FN}^{(0)} \right|^2 \Psi$ (the function Ψ is determined by (5.9) and shown in Fig. 5.4), ρ_d and c_p are the density and specific heat capacity, respectively. So to reach the melting temperature the required peak current density is:

$$j_{FN}^{(0)} = \left(\sigma c_T \rho_d \Delta T_m / \Psi \tau \right)^{1/2}. \tag{5.13a}$$

Here ΔT_m is the temperature rise from the initial temperature to the melting temperature). The condition (5.12) and the definition of the diffusion coefficient allows one to rewrite (5.13a) as:

$$j_{FN}^{(0)} > \left(\sigma \Delta T_m \lambda_T / \Psi \right)^{1/2} / h. \tag{5.13b}$$

For a copper and molybdenum the materials that are typically used in accelerating structures, the work functions are 4.3 and 4.2 eV, respectively; so in accordance with Fig. 5.4 the value of the function Ψ is equal to 0.09. As follows from (5.13b), to reach the melting temperature in 100 nsec pulses in 10 micron high microprotrusion of copper or molybdenum the electron current density should be in the range of a few $A / \mu m^2$.

Results of the analysis of Eq. (5.7) and Eq. (5.11) are presented in figures 5.6-5.9. Figure 5.6 shows the temperature evolution in a copper protrusion with a height equal to $10 a_0$, $a_0 = 0.5 \mu m$, amplification factor $\beta = 56$ and two different locations of the boundary condition $\Delta T = 0$ at $z = 0$ and $z = -10a_0$. It can be seen from the result presented in the figure 5.6 that the location of this boundary condition plays a role practically at all instants of time starting from one nsec. Therefore, below only results of calculations performed with the boundary condition imposed at $z = -10a_0$ are presented.

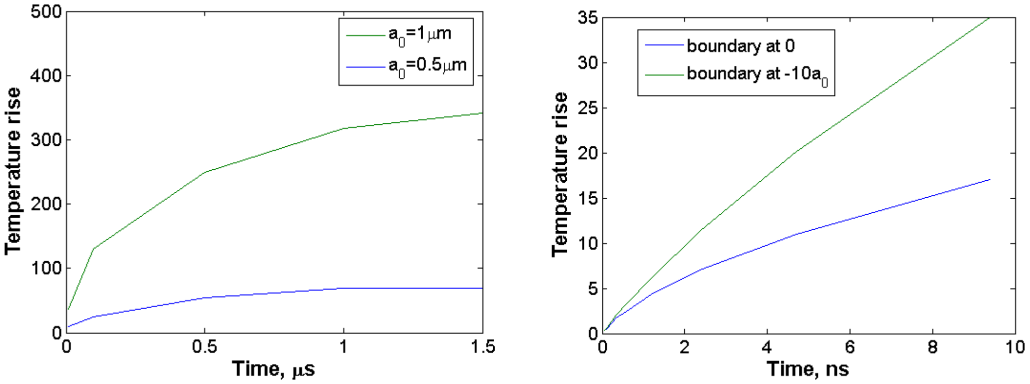

Figure 5.6 Temperature rise in protrusions for the cases when the boundary condition $\Delta T = 0$ is imposed at different locations: $z = 0$ and $z = -10a_0$; right figure shows the process in its initial phase.

The simulations for protrusions of the same geometry were also performed by using both an accurate method of calculating the field and current in the protrusion and by using a 1D approximation (5.10). Results of these simulations are shown in Fig. 5.7. It was found that the 1D approximation yields lower temperature rise. Therefore the same temperature rise can be obtained with the use of the 1D model by assuming that the field amplification factor is higher than in the case of an accurate model.

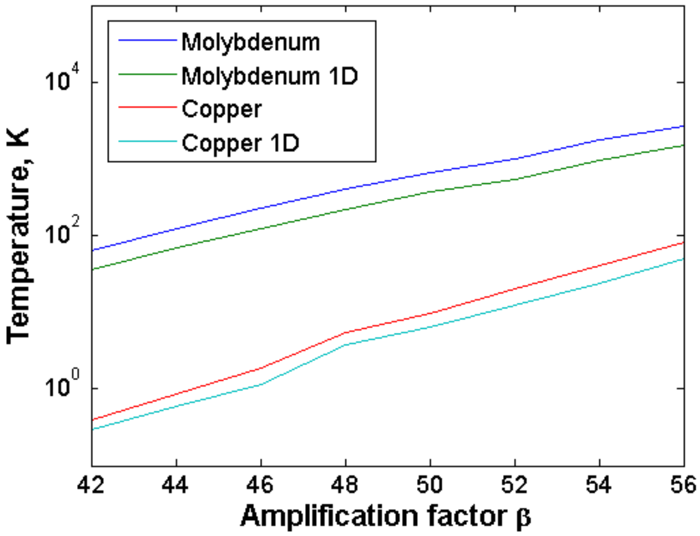

Figure 5.7 Temperature rise in 20 nsec pulses calculated with the use of accurate model and 1D approximation. The ratio b is equal to 0.9; the background field is 300 MV/m.

The scaling parameter a_0, which is the radius of the equipotential of the charge located at origin, determines the size of the protrusion. Results presented in Figures 5.8 and 5.9 indicate that to get significant temperature rise in realistically short pulses the field amplification factors should exceed 50 and the protrusions should have a whisker-like shape which correspond to values of the parameter b close to one. In Fig. 5.8 we show the temperature rise for different values of scaling parameter a_0 and for the pulses length of 100 ns and 200 ns.

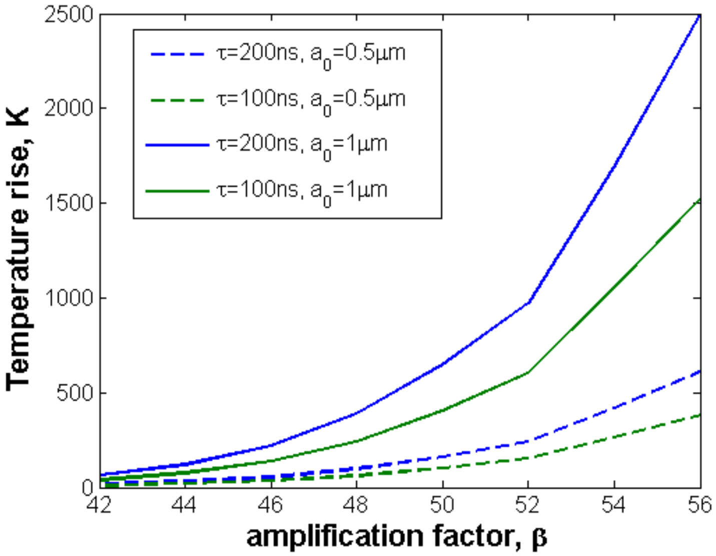

Figure 5.8 Temperature rise in copper for different values of the pulse duration (the ratio *b* is equal to 0.9).

The time required to reach melting is shown in Fig. 5.9 for two sorts of protrusions with slightly different values of the b-ratio which corresponds to different protrusion heights. Both sorts of protrusions have a whisker-like shape. As could be expect, in the case of protrusions with a larger height-to-base ratio (longer whiskers) the time required to reach melting temperature on the protrusion apex is shorter. The temperature rise required for melting copper and molybdenum is close to 1000 K and 2500 K, respectively. At the same time, shallow protrusions with small height-to-base rations cannot be heated up to melting because of the heat sink to the structure wall.

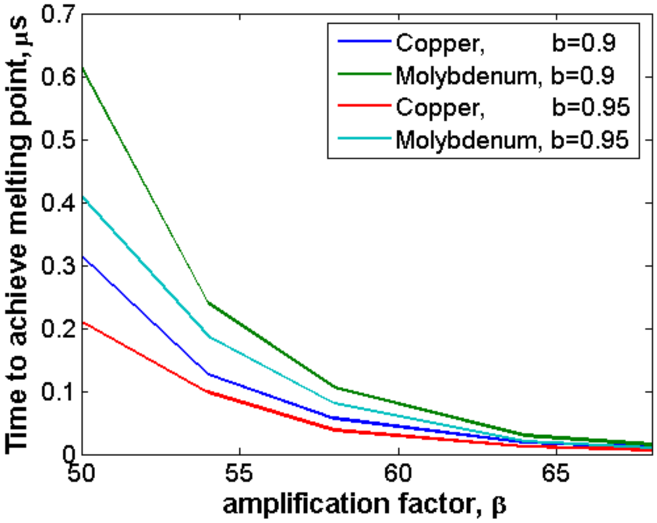

Figure 5. 9 Time required for achieving melting temperature of copper and molybdenum in protrusions of different geometry. It is assumed that $a_0 = 1\mu m$, there are shown two cases: b=0.9 and the protrusion height about 10 a_0 and b=0.95 and the protrusion height about 20 a_0.

5.4 Summary

The formulation of the problem of protrusion heating that was given in this chapter allowed an accurate determination of the electric field distribution inside a metallic protrusion of micron size and the temperature rise inside of it. This temperature rise is greatly dependent on the geometry of the protrusion, i.e. on the field amplification factor, β and on the protrusion height-to-base ratio. It was found that in order to achieve melting temperature in copper and molybdenum whisker-like protrusion apexes for pulses with several hundred nanosecond length the field amplification factor should be larger than 50. In this analysis several important effects were omitted from the consideration. Inclusion of those factors should be the subject of the further study. Accurate analysis of thermal processes in micro-protrusions should help to identify regimes of stable operation with low breakdown rate in high-gradient accelerating structures. The presented analysis showed that it is possible to melt the whisker-like protrusions when the field amplification factor is high enough and the pulse length is long enough. It is shown that when amplification factor is higher than 50, it is possible to achieve melting temperature of the protrusions in several hundred nanosecond pulses. This is consistent with what was shown in the literature [5.1]. The larger the height-to-base ratio for the protrusion, the easier it is to heat its apex up to the melting point. It was also found that the heat flow plays an important role in the process; in particular, it was found that to get meaningful results the boundary condition $\Delta T = 0$ should be placed deep enough in the metal. First of all, all the effects of magnetic field were completely ignored including the induction heating. Secondly, the Nottingham effect and the radiation losses from the surface of the protrusion were not taken into consideration [5.18], inclusion of these factors may lead to the creation of hotter regions inside the protrusion [5.6], which in turn may lead to the thermo-mechanical instability and destruction of the tips. This work was continued by another member of our research group, where all the mentioned effects were included into the consideration [5.20].

Chapter 6: Conclusions and future work

The development and experimental investigation of the sub-terahertz gyrotron operating at 0.67THz developed for the purpose of concealed radiation detection has proven to be a challenging task. At the same time, this activity provided a reach field for future studies in the areas of tube development and various physical processes that affect the gyrotron performance. The extensive analysis of the gyrotron resonator circuit and its various components allowed this tube to demonstrate a generation of electromagnetic radiation at record power levels exceeding 200kW and with efficiencies in excess of 20% at certain regimes. These results have clearly demonstrated that this source have huge potential for the chosen task of detection of concealed radiation. The experiments with this gyrotron have shown that it is possible to create a breakdown event on an array of initiators and in the chamber with controlled atmosphere. To further improve the generation of the electromagnetic radiation several issues in the gyrotron design should be addressed in the subsequent experiments. These issues included a need in a more robust output window and more reliable electron gun.

The analysis of the data obtained in the experiments gave rise to a number of theoretical studies that analyzed a number of processes affecting the performance of the detection scheme the sub-terahertz gyrotron and addressing some general issues in high power microwave device operation, that were the prime suspects in deteriorating the device performance. A careful analysis of the breakdown volume and the effect that the atmosphere has on the propagating radiation was performed, making possible further enhancement of the range of the system. At the same time the performance of the gyrotron was severely hindered by the breakdown events taken place inside the tube. This breakdown events deteriorate the quality of the output RF radiation. To deepen the understand of the process of RF breakdown inside a high-gradient structure a number of scenarios, including the role of the microprotrusion on the surface of the metal and metallic particles that can be melted in high frequency RF fields, were analyzed. This analysis expanded the current understanding of the breakdown process.

Overall this work is a first step in development of a truly portable device for remote detection of concealed radiation that lays the foundation of the future experiments.

Appendices

Appendix A

It is well known that electric field in the vicinity of a sharp metallic object is amplified. For many applications it is important to determine the amplification factor of this field and the radius of curvature. Point Charge Model (PCM)[5.12, 5.13], that was developed for the analysis of field emitters provides an elegant solution to these tasks. This model is based on the fact that it is possible to represent protrusion surface using a linear chain of point charges assembled in such a way that so that their equipotential surface mimics that of an actual object. By themselves the radius of the equipotential line of the nth point charge, denoted as $|a_n|$, can be related to the magnitude of the charge itself.

Assembling these charges in a line approximates the emitter, as in Fig. 1 in the case of 3 point charges (n=3), such that the nth point charge is located on the apex of the (n-1)-th sphere. The expression for the field and apex radius can be obtained analytically if $a_{n+1}/a_n= r$ for all n, and such an example is shown in Fig. 2 for r=0,75 for various n. The growth as well as the destruction of metallic whiskers or bumps can therefore be characterized by evolution of n and r. If the apex of an emitter sharpens due to surface migration, for instance, under application of high fields, then the r factor should decrease. On the other hand, if the apex is damaged and blunted, then the n factor r should decrease.

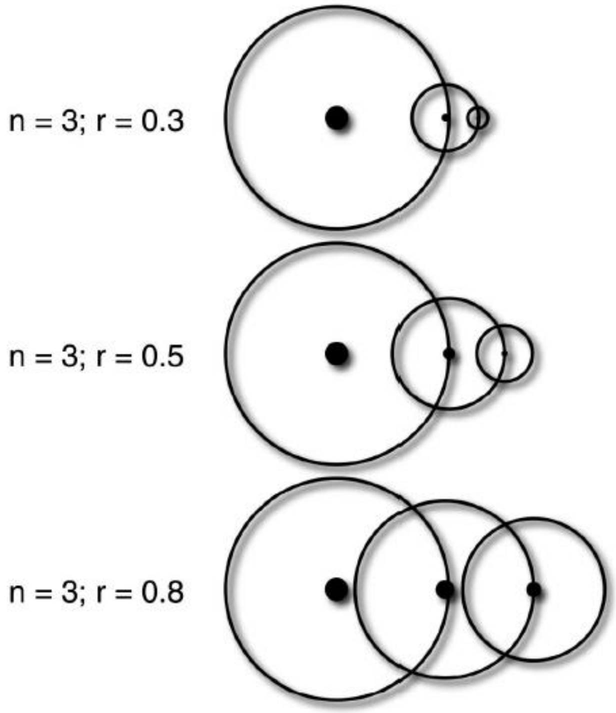

Figure 1 The illustration of Point Charge Model. The circles are the equipotential lines of their center charge only: the total equipotential surface is created by all the point charges and is therefore slightly larger, reproduced from [5.13].

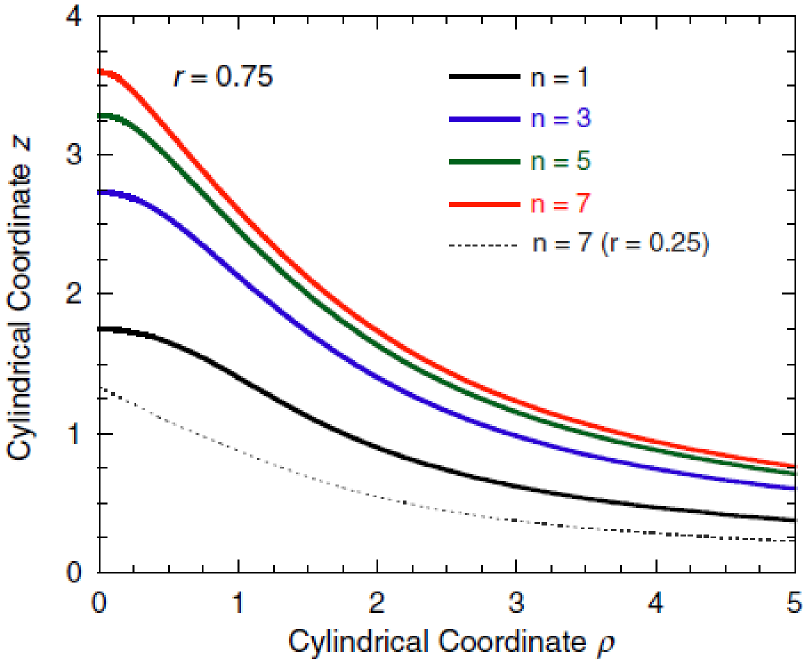

Figure 2 The shape of the emitter in the point-charge model for different values of n for r=0.75. Also shown in the figure is the case for n=7 and r=0.25 surface, reproduced from [5.13].

Bibliography

[1.1] J. F. Frittelli, *Port and Maritime Security: Background and Issues* (New York, Novinka Books, 2005).
[1.2] M. Yu. Glyavin, A. G. Luchinin, G. S. Nusinovich, J. Rodgers, D. G. Kashyn, C. A. Romero-Talamas, and R. Pu, J. Appl. Phys. Lett. **101**, 153503 (2012).
[1.3] V.L. Granatstein, G.S. Nusinovich, J. Appl. Phys. **108**, 063304 (2010).
[1.4] R. Paschotta, "Laser induced breakdown" in Encyclopedia of Laser Physics and Technology, http://www.rpphotonics.com/laser_induced_break-down.html
[1.5] P. Woskoboinikow, W. J. Mulligan, H. C. Praddaude, and D. R. Cohn, J. Appl. Phys. Lett.**32**, 527 (1978).
[1.6] G. Nusinovich, V. Granatstein, T. Antonsen, Jr., R. Pu, O. Sinitsyn, J. Rodgers, A. Mohamed, J. Silverman, M. Al-Sheikhly, and Y. Dimant, IEEE International Vacuum Electronics Conference, Monterey, CA, May 18–20, 2010, IVEC 2010 Book of Abstracts IEEE cat. no. CFP10VAM-ART, pp. 197–198.
[1.7] G. S. Nusinovich, P. Sprangle, C. A. Romero-Talamas, and V. L. Granatstein J. Appl. Phys. **109**, 083303 (2011).
[1.8] A. D. McDonald, *Microwave Breakdown in Gases* (Wiley, New York, 1966), p. 162.
[1.9] A. Yariv, *Quantum Electronics* (Wiley, New York, 1975).
[1.10] V. Granatstein and W. Lawson, IEEE Trans. Plasma Sci. 24, 648 (1996).
[1.11] M. V. Ivashcenko, A. I. Karapuzikov, A. N. Malov, and I.V. Sherstov, Instrum. Exp. Tech. **43**, 119 (2000).
[1.12] G.S. Nusinovich, M. K. A. Thumm, M. I. Petelin. J.Infrared Milli Teraherz Waves **35** 325 (2014).
[1.13] K. Takahashi, K. Kajiwara, Y. Oda, A. Kasugai, N. Kobayashi, K. Sakamoto, J. Doane, R. Olstad, and M. Henderson Rev. Sci. Instrum. **82**, 063506 (2011).
[1.14] M. Blank, P. Borchard, S. Cauffman, K. Felch 15th International Conference on Terahertz Electronics. IRMMW-THz. Joint 32nd International Conference on " 364-366 (2007).
[1.15] M. Glyavin, Yu. Bykov, G. Denisov J. Jpn. Soc. Infrared Sci. and Tech., **12,** 60-64 (2002).
[1.16] M. Yu. Glyavin, A. G. Luchinin, and G. Yu. Golubiatnikov Phys. Rev. Lett. **100**, 015101 (2008).
[1.17] A. V. Gaponov, A. L. Goldenberg, D. P. Grigoryev, I. M. Orlova, T. B. Pankratova, M. I. Petelin, JETP Letters, **2**, 267 (1965).
[1.18] A. V. Gaponov, M. I. Petelin, V. K. Yulpatov, Radiophys. Quantum Electronics, **10**, 794 (1967).
[1.19] V. A. Flyagin, A. V. Gaponov, M. I. Petelin, V. K. Yulpatov, IEEE Trans. on Microwave Theory and Technique, **25**, 514 (1977).
[1.20] G. S. Nusinovich, *Introduction to the Physics of Gyrotrons* (Johns Hopkins University Press, Baltimore, 2004).
[1.21] A. A. Andronov, V. A. Flyagin, A. V. Gaponov, A. L. Goldenberg, M. I. Petelin, V. G. Usov, and V. K. Yulpatov, J. Infrared Phys. 18, 385 (1978).

[1.22] Manfred Thumm Plasma Phys. Control. Fusion 45 A143 (2003).
[1.23] A.L. Goldenberg, M.I. Petelin, Izv. VUzov. Radiofizika 16, 141–149 (1973).
[1.24] Gregory S. Nusinovich, Ruifeng Pu, Thomas M. Antonsen Jr., Oleksandr V. Sinitsyn, John Rodgers, Ali Mohamed, Joseph Silverman, Mohamad Al-Sheikhly, Yakov S. Dimant, Gennady M. Milikh, Michael Yu. Glyavin, Alexei G. Luchinin, Eugene A. Kopelovich, Victor L. Granatstein J. of Infrared.and Millimeter. Terahertz Waves 32, pp 380-402 (2011).
[1.25] K. Nguyen, E. Wright, V. Jabotinski, D. Pershing, P. Horoyski, A. Roitman, R. Dobbs, M. Hyttinen, D. Berry, D. Chernin, A. Burke, J. Petillo, J. Calame, B. Levush, J. Pasour, ICOPS-2010, Norfolk, June 2010, paper 2C-4 (2010).
[1.26] M. Botton, T.M. Antonsen Jr, B. Levush, K.T. Nguyen, A.N. Vlasov IEEE Transactions on Plasma Science, vol. 26, issue 3, pp. 882-892 (1998).
[1.27] K. Sakamoto, A. Kasugai, Y. Ikeda, K. Hayashi, K. Takahashi, S. Moriyama, M. Seki, T. Kariya, Y. Misunaka, T. Fuji, T. Imai, Nucl. Fusion, 43, 729 (2003)
[1.28]Kesar, Petillo, J.J.; Nusinovich, G.S.; Herrmannsfeldt, W.B; Granatstein, V.L. IEEE Trans on Plasma Sci. 39 (2011).
[1.29] W. Lawson, P.E. Latham, V. Specht, M.K.E. Lee, Q. Qian, J.P. Calame, B. Hogan, V.L. Granatstein, M. Reiser, C.D. Striffler Conf.Proc. C930517 2670-2672 (1993).
[1.30] T. M. Taylor, Proceedings of EPAC, Paris, France (2002).
[1.31] V. A., Flyagin, A. G. Luchinin, and G. S. Nusinovich Int. J. of lnfr. and Mill. Waves, Vol. **4**, No. 4 (1983).
[1.32] M.Yu. Glyavin, A.G. Luchinin, and G.Yu. Golubiatnikov Phys. Rev. Lett. **100**, 015101 (2008).
[1.33] A. Kasugai, K. Sakamoto, K. Takahashi, K. Kajiwara, and N. Kobayashi Nucl. Fusion 48, 054009 (2008).
[1.34] V. I. Belousov, M. M. Ofitserov, V. Yu. Plakhotnik, and Yu. V. Rodin, Instrum. Exp. Tech. **39** , 402 (1996).
[1.35] A. G. Shkvarunets, Prib. Tekh. Exp. 4, 72 (1996).
[1.36] R. Pu, Gregory S. Nusinovich, Oleksandr V. Sinitsyn, and Thomas M. Antonsen Jr. Phys. Plasmas **18**, 023107 (2011).
[1.37] M. Thumm Int. J. of Infrared and Millimeter Waves, Vol. **19** 3 (1998)

[2.1] V.L. Granatstein, G.S. Nusinovich, J. Appl. Phys. **108**, 063304 (2010).
[2.2] G. S. Nusinovich, P. Sprangle, C. A. Romero-Talamas, and V. L. Granatstein, J. Appl. Phys., **109**, 083303 (2011).
[2.3] G. S. Nusinovich, F. Qiao, D.G. Kashyn, R. Pu, L.S. Dolin J. of Appl Phys, **113**, 233303 (2013).
[2.4] A. G. Litvak, Ch. 4 in *Applications of High-Power Microwaves*, Eds. A. V. Gaponov-Grekhov and V. L. Granatstein, (Artech House, Boston-London, 1994).
[2.5] V. E. Semenov, Sov. J. Plasma Phys., **10** 328 (1984).
[2.6] A. Yariv, *Quantum Electronics*, (John Wiley and Sons, Inc., New York, 1975), Sect. 6.5.
[2.7] I. S. Gradshtein and I.M. Ryzhik, “Tables of Integrals, Series, and Products”, Academic Press, New York, 1980.

[2.8] V. I. Tatarskii, *The effects of the Turbulent Atmosphere on Wave Propagation* (Jerusalem: Israel Program for Scientific Translations, 1971).
[2.9] A. D. Wheelon, *Electromagnetic Scintillation: I. Geometrical Optics, and II. Weak Scattering* (Cambridge University Press, Cambridge, UK, 2001).
[2.10] R. L. Fante, , Proc. IEEE, **63**, 1669-1692 (1975).
[2.11] W. B. Miller, J. C. Ricklin and L. C. Andrews, J. Opt. Soc. Am., A, **10**, 661 (1993).
[2.12] L. S. Dolin, , Radiophys. and Quant. Electron., **11**, 486-491 (1968).
[2.13] S. M. Rytov, Izv. AN SSSR, Ser. Fiz., (Bull. of the AS USSR, Physical series), No.**2**, 223-259 (1937) [In Russian].
[2.14] L. S. Dolin, Soviet Radiophysics, **7**, 380 (1964).
[2.15] M. Abramowitz and I. A. Stegun, *Handbook of mathematical functions*, (Nat. Bureau of Standards, 1964).

[3.1] D. Kashyn, G.S. Nusinovich, T. M. Antonsen Jr. IEEE Transactions on Plasma Science Vol., **39**, Issue 8. (2011)
[3.2] M. Yeddulla, G. S. Nusinovich, and T. M. Antonsen, Jr., Phys. Plasmas, vol. **10**, no. 11, p. 4513, 2003.
[3.3] M. Thumm, S. Alberti, A. Arnold, P. Brand, H. Braune, G. Dammertz, V. Erckmann, G. Gantenbein, E. Giguet, R. Heidinger, J.-P. Hogge, S. Illy, W. Kasparek, H. P. Laqua, F. Legrand, W. Leonhardt, G. Lievin, G. Michel, G. Neffe, B. Piosczyk, M. Schmid, K. Scworer, and M. Q. Tran, IEEE Trans. Plasma. Sci., vol. **35**, no 2, pp 143-153 (2007).
[3.4] K. Sakamoto, A. Kasugai, K. Takahashi, R. Minami, N. Kobayashi, and K. Kajiwara, Nat Phys. vol **3**, pp. 411-414 (2007).
[3.5] G.S. Nusinovich, IEEE Trans Plasma Sci., Vol. **27**, pp. 313-326, (1999).
[3.6] W. Lawson, J. Calame, V. L. Granatstein, G. S. Park, C. D. Striffler, and J. Neilson, Int. J. Electron. **61**, 969 _1986_.
[3.7] D.R. Whaley, M. Q. Tran, S. Alberti, T. M. Tran, T. M. Antonsen, Jr., and C. Tran Phys. Rev. Lett., vol **75**, no. 7, pp. 1304-1307, Aug 1995.
[3.8] R. J. La Haye, S Gunter, D. A. Humphreys, J. Lohr, T.C. Luce, M. Maraschek, A. Muck, K. Nagasaki, S. D. Pinches, ad E. J. Strait, Phys. Plasmas, vol. **9**, no. 5, pp. 2051-2060, May 2002.
[3.9] ECRH Groups at IPP Greifswald, FZK Karlsruhe, IPF Stutgart, W Kasparek, M. Petelin, V. Erckmann, D. Schegolkov, A. Bruschi, S. Cirant, A. Litvak, M. Thumm, B. Plaum, M. Grunert, and M. Mathaner, Fusion Sci. Technol.,
[3.10] S. Tsimring, *Electron Beams and Microwave Vacuum Electronics*. (Hoboken New Jersey:Wiley, 2007).
[3.11] G.S. Nusinovich, O.V. Sinitsyn, L. Velikovich, M. Yeddulla, T. M. Antonsen, Jr., A.N. Vlasov, S.R. Caufmann, and K. Felch IEEE Trans. Plasma Sci., vol. **32**, pp 841-852 (2004).
[3.12] S. Tsimring, *Electron Beams and Microwave Vacuum Electronics*. (Hoboken New Jersey:Wiley, 2007), p.468
[3.13] A.S. Gilmour, Jr., *Microwave Tubes*. (Norwood, MA: Aretech House, 1986), p. 129.

[3.14] G.S. Nusinovich, *Introduction to the physics of the gyrotrons*. (Baltimore, MD: The John Hopkins Univ. Press, 2004), p. 63.
[3.15] A. Goldenberg and M.I. Petelin, Radiophys. Quantum Electron., vol. **16**, p. 106, 1973.
[3.16] B.G. Danly and R.J. Temkin, Phys. Fluids, vol. **29**, p.561 (1986).
[3.17] M. Botton, T.M. Antonsen, Jr. B. Levush, K. T. Nguyen, and A.N. Vlasov, IEEE Trans. Plasma Sci., vol. **26**, no.3 pp. 882-892, Jun. 1998.
[3.18] V. N. Manuilov, B. V. Raisky, E. A. Solujanova, and Sh. E. Tsimring, Radiotekhn. Electron., **40**, pp. 648-655 (1995).

[4.1] R. B. Palmer, R. C. Fernow, J. C. Gallardo, D. Stratakis and D. Li, Phys. Rev. ST – Accelerators and Beams, **12**, 031002 (2009).
[4.2] P. Wilson, Proc. 12th AAC Workshop, Eds. M. Conde and C. Eyberger, AIP Conf. Proc., 877, p. 27, Melville, New York, 2006.
[4.3] Z. Insepov, J. H. Norem, and A. Hassanein, Phys. Rev. ST – Accelerators and Beams, **7**, 122001 (2004).
[4.4] H. Padamsee and J. Knobloch, AIP Conf. Proc. 474, Ed. R. M. Phillips, Woodbury, New York, p. 212, (1999).
[4.5]
[4.6] J. Cheng, R. Roy, and D. Agrawal, J. Mater. Sci. Lett **20,** 1561 (2001).
[4.7] W. L. Perry, A. K. Datye, A. K. Prinja, L. F. Brown and J. D. Katz, AIChE J. **48**, 820 (2002).
[4.9] S.W. Kingman and N.A. Rowson, Minerals Eng. **11**, 1081 (1998).
[4.9] M.D. Turner, R.L. Laurence, W.C. Conner, and K.S. Yngvesson AIChE J. **46**, 758 (2000).
[4.10] J.H. Booske, R.F. Cooper, and S.A. Freeman, Mater. Res. Innovations **1**, 77 (1997).
[4.11] V.A. Dolgeshev and S.G. Tantawi, AIP Conf. Proc. **691**, 151 (2003).
[4.12] H. Bosman, PhD. Thesis, University of Micihgan, 2004.
[4.13] J. M. Osepchuk, and R.C. Petersen, IEEE Microw. Mag. **2**, 57 (2001).
[4.14] L.D. Landau and E.M. Lifshitz, Electrodynamcis of Continious Media (Pergamon Press, Oxford, 1960).
[4.15] Scientific Papers by Lord Rayleigh (Dover, New York, 1964), Vol. **1**, p. 104.
[4.16] W. Tang, H. Bosman, Y.Y. Lau and R. M. Gilgenbach, J. Appl. Phys. **97**, 114915 (2005).
[4.17] S. Ramo and J.R. Whinnery, *Fields and Waves in Modern Radio* (John Wiley & Sons, New York, 1960), p. 243.
[4.18] M. Abramowitz and I.A. Stegun, *Handbook of Mathematical Functions*, (National Bureau of Standards, 1964), sec. 9.9 and Table 9.12.
[4.19] V.A. Dolgashev, Report No. SLAC-PUB-10114 (2002).
[4.20] Z. Insepovm J.H. Norem, and A. Hassanein, Phys. Rev. ST Accel. Beams 7, 122001 (2004).
[4.21] F. Djurabekova and K. Nordlund, CLIC Breakdown Workshop, 2008.
[4.22] W. Wuensch, in Proceedings of the 8th European Particle Accelerator Conference, Paris, 2002 (EPS-IGA and CERN, Geneva, 2002), p. 134.

[4.23] G.S. Nusinovich, D. Kashyn, and T.M Antonsen, Jr., Phys. Rev. ST-Accel. Beams, vol. **12**, no. 10, p 101001 (2009)

[4.24] L.D. Landau and E.M. Lifshitz, *Electrodynamcis of Continious Media* (Pergamon Press, Oxford, 1960).

[4.25] S. G. Tantawi, V. Dolgashev, Y. Higashi, and B. Spataro, AIP Conf. Proc., 1299, Eds. S. Gold and G. S. Nusinovich, pp. 29-37 (Melville, New York, 2010).

[4.26] P.-M. Robitaille, IEEE Trans. Plasma Sci., 31, 1263-1267 (2003).

[4.27] B. Piosczyk, A. Arnold, G. Dammertz, O. Dumbrajs, M. Kuntze, and M. K. Thumm, IEEE Trans. Plasma Sci., **30**, 819-827 (June 2002).

[4.28] D. Schiffler (private communication, February 2011).

[5.1] J. W. Wang and G. A. Loew, SLAC-PUB-7684, (Oct.1997).

[5.2] R.B. Palmer, R.C Fernow, J.C. Gallardo, D. Stratakis, D. Li, Phys. Rev ST Accel. & Beams, **12**, 031002 (2009).

[5.3]. D. Kashyn, G. S. Nusinovich, T. M. Antonsen, Jr., and K. L. Jensen, Proc. AAC-2010, AIP Conf. Proc. 1299, Melville, New York, 2010, p. 387.

[5.4] G. Fursey, *Field Emission in Vacuum Microelectronics* (Kluwer Academic/Plenum Publishers, New York, 2005), Ch. 3.

[5.5] R. H Fowler and L. Nordheim, Proc R. Soc, A **119**, 173 (1928).

[5.6] E. E. Martin, J. K. Trolan, and W. P. Dyke, J. Appl. Phys., **31**, 782 (1960).

[5.7] D. R. Whaley, R. Duggal, C. M. Armstrong, C. L. Bellew, C. E. Holland, and C. A. Spindt, IEEE Trans. Electron Devices, **56**, 896 (2009).

[5.8] L. D. Landau and E. M. Lifshitz, *Electrodynamics of Continuous Media* (Pergamon Press, Oxford, 1960), pp. 16-17.

[5.9] H. G. Kosmahl, IEEE Trans. Electron Devices, **38**, 1534 (1991).

[5.10] G. Fursey, *Field Emission in Vacuum Microelectronics* (Kluwer Academic/Plenum Publishers, New York, 2005), Ch. 3.

W. R. Smythe, “Static and dynamic electricity”, International Series in Pure and Applied Physics, 3rd Ed., 1968.

[5.11] O. B. Isaeva, M. V. Eliseev, A. G. Rozhnev, N. M. Ryskin, Solid-State Electronics, **45**, 871 (2001).

[5.12] K. L. Jensen, Y.Y. Lau, D.W. Feldman P.G. O’Shea, Phys. Rev. ST Accel. & Beams **11**, 081001 (2008).

[5.13] K. L. Jensen, J. Vac. Sci. Technol. B **29**, 02B101 (2011).

[5.14] D. W. Williams and W. T. Williams, J. Phys. D: Appl. Phys., **5**, 280 (1972).

[5.15] R. P. Little and W. T. Whittney, J. Appl. Physics, **34**, 2430 (1963).

[5.16] A. S. Gilmour, Jr., *Microwave Tubes*, (Artech House, Norwood, MA 1986), Fig. 15.32.

[5.17] A. Hassanein et al., Phys. Rev. ST Accel. & Beams, **9**, 062001 (2006).

[5.18] F. Djurabekova and K. Nordlund, CLIC Breakdown Workshop, May 2008 (http://indico.cern.ch/materialDisplay)

[5.19] S. Calatroni, CLIC Workshop 2007 – RF Structures and Sources (http://indico.cern.ch/conferenceDisplay.py?confId=17870).

[5.20] A. C. Keser, T. M. Antonsen, G. S. Nusinovich, D. G. Kashyn, and K. L. Jensen Phys. Rev. ST Accel. Beams **16**, 092001 – Published 24 September 2013